

RESPONSE EXPERIMENT OF PACIFIC OCEAN TO ANOMALOUS WIND STRESS
WITH OCEAN GENERAL CIRCULATION MODEL

BY

OCEANOGRAPHICAL RESEARCH DIVISION

気象研究所技術報告

第24号

海洋大循環モデルを用いた風の応力異常に対する太平洋の応答実験

海洋研究部

気象研究所

METEOROLOGICAL RESEARCH INSTITUTE, JAPAN

MARCH 1989

Meteorological Research Institute

Established in 1946

Director : Dr. Yasushi Okamura

Forecast Research Division	Head : Mr. Isao Kubota
Climate Research Division	Head : Mr. Kazuhi Kiriyaama
Typhoon Research Division	Head : Mr. Kiyoshi Kurashige
Physical Meteorology Research Division	Head : Mr. Mitsuru Asahi
Applied Meteorology Research Division	Head : Mr. Tsunehiro Majima
Meteorological Satellite and Observation System Research Division	Head : Mr. Syoichi Koinuma
Seismology and Volcanology Research Division	Head : Dr. Mamoru Katsumata
Oceanographical Research Division	Head : Mr. Akira Sano
Geochemical Research Division	Head : Dr. Yukio Sugimura

1-1 Nagamine, Tsukuba-shi, Ibaraki-ken 305, Japan

Technical Reports of the Meteorological Research Institute

Editor-in-chief : Mamoru Katsumata

Editors : Fumiaki Fujibe Hideji Kida Yoshimasa Takaya
 Shigeru Chubachi Junji Sato Osamu Uchino
 Itsuo Furuya Masahiro Endoh Hisayuki Inoue

Managing Editors : Makoto Matsushita, Kazuyuki Nakayama

Technical Reports of the Meteorological Research Institute

has been issued at irregular intervals by the Meteorological Research Institute since 1978 as a medium for the publication of survey articles, technical reports, data reports and review articles on meteorology, oceanography, seismology and related geosciences, contributed by the members of the MRI.

序

アフリカの乾燥・砂漠化が例であるように、近年、気候問題が世界的に重要視されている。その気候の形成や変動には海洋が大きくかかわり、と言うよりも、相互に影響を及ぼし合う関係にあることも認識されている。

1979年の世界気候会議で承認された「世界気候計画（WCP）」は、以後、具体的作業に入り、「世界気候研究計画（WCRP）」の中で、大気・海洋問題が重要な課題になっている。TOGA（熱帯海洋・全球大気研究計画）や WOCE（世界海洋循環実験計画）が例である。

現在、海洋を含めた気候異変には、自然科学分野のみならず、政治・経済関係、さらには一般の人々も強い関心を示している。ちょっとした気象異変や、社会の変わった動きにすら、「エル・ニーニョの所為ではないか」という。これは豊富な情報が一因であろう。また、約20年前のエル・ニーニョ発生時に、連鎖反応的に起きた世界的な農業と経済の混乱が、わが国では豆腐の異常値上げとして食生活に顕現したことを記憶しているからかもしれない。ユーザーが要求する知識内容は様々であろうが、大気と海洋の壮大で複雑な相互作用を解明し、将来の現象を予測することが、我々の役目であろう。

しかし、元来、海洋は人間が生存している場ではない。このため、観測データも知識も不十分である。今後、衛星をはじめ、新しい観測技術によって、データも知識も蓄積されようが、それでもかなりの年月が必要であろう。しかし、それまで、いや、それから、何らかの方法で、目的に近づく努力が必要である。それが、モデル手法による海洋変動の把握と予測である。外国では、1960年代後半から、モデルを用いた海洋と気候の研究が盛んになり、その様子は本報告の膨大な Reference からもうかがえる。わが国でも、大学等で成果をあげつつある。

さて、気象研究所海洋研究部では、動的な海洋をイメージに置いて、昭和58年度から「海洋大循環数値モデルの開発」を開始し、途中で計算能力の向上もあって、予期以上の成果をあげて、一応、昭和62年度で終了させた。今後は、このモデルを基礎にして、大気・海洋相互作用や様々な海洋現象を研究していく所存である。

本報告は、開発途中のモデルを試行したものである。良いにつけ悪いにつけ、様々な鍵を顕在化させているので、今後の研究にとって良い道標となろう。海面に及ぼす風の変動・異常が、いかに海洋（主として水温構造）に影響を及ぼすかがテーマであり、その産物は予測される海洋状態である。

内容は、まず、モデルの紹介にかなり力をそそぎ、入力要素として水温・塩分・海水の密度・海流などの海洋要素と風・気温・降水・蒸発などの大気要素を用いている。これを動かして動的な定常状態を作り上げる。これに、太平洋の海洋大循環を大きく支配している赤道付近の東風と

北半球の貿易風を様々に変化させて与え、モデルを駆動させて、対応する海洋状態を産出している。

本報告の目的は、前記の TOGA や WOCE の指向に合致しているが、結果は必ずしも満足すべきものではない。海洋の渦スケールは大気の高・低気圧スケールに比較して 1 桁以下であるので、同レベルの産物を得るには、さらに計算機的能力向上が必要である。また、必要とする海洋データも質・量ともに不十分である。今後は、相互に補完しながら、研究を推進していきたい。

平成元年 3 月

気象研究所海洋研究部長

佐 野 昭

Response Experiment of Pacific Ocean
to Anomalous Wind Stress
with Ocean General Circulation Model*

by

Oceanographical Research Division
Meteorological Research Institute

海洋大循環モデルを用いた風の応力異常に
対する太平洋の応答実験**

気象研究所海洋研究部

* Presented by Yoshihiro Kimura : Marine Department, Japan Meteorological Agency, and
Masahiro Endoh : Oceanographical Research Division, Meteorological Research Institute

** 木村吉宏 : 気象庁海洋気象部
遠藤昌宏 : 海洋研究部

Contents

Abstract	1
和文概要	2
1. Introduction	3
2. Description of the Model	4
2.1 Governing equations	4
2.2 Model domain and boundary conditions	5
2.3 Prognostic equations	7
2.4 Grid system and finite difference equations	9
2.4.1 Grid system	9
2.4.2 Time differencing	12
2.4.3 Momentum equations	12
2.4.4 Temperature and salinity equations	17
2.4.5 Boundary conditions	18
2.4.6 Vorticity equation	20
2.4.7 Programming	21
2.4.8 Notes	22
2.5 External forcing	23
2.6 Vertical resolution of the model ocean and initial conditions	24
2.7 Computation and parameters	25
3. Normal State	28
3.1 Time integration	28
3.2 Horizontal distributions	29
3.3 Vertical sections	36
3.4 Meridional circulation and meridional heat transport	41
3.5 Comments	42
4. Response Studies	48
4.1 Introduction	48
4.2 Response to anomalous forcing in the equatorial ocean	53
4.2.1 Anomalous eastward wind (cases 100 and 101)	53

4.2.2 Effect of the difference in the longitude of the forcing anomaly (cases 110, 120 and 130)	69
4.3 Response to anomalous forcing in the extra-equatorial ocean	78
4.3.1 Anomalous trade wind increase (cases 200 and 201)	78
4.3.2 Variation 1 (case 210)	87
4.3.3 A warm anomaly (case 250)	89
4.4 Summary and remarks	89
References	95

Abstract

A general circulation model of the ocean is developed for the study of dynamical response to the wind stress change. The model is idealized in the horizontal dimension having a rectangular shape with flat bottom topography. The purpose of the present report is to describe the model developed and to present the results in detail.

The numerical model extends over 100° in the east-west direction from 30°S to 54°N in the meridional direction with 8 levels in the vertical direction and 2° (N-S) \times 2.5° (E-W) horizontal grid spacing. Zonally uniform wind stress and heat and salt fluxes imposed on the sea surface drive the steady normal general circulation in 140 years of integration.

Anomalies of wind stresses corresponding to (1) relaxation of the easterly winds in the equatorial region and (2) intensification of the trade winds in the tropical/subtropical region are imposed for 90 and 180 days, respectively. Temperature anomalies defined as the difference between the results for anomalous and normal wind stresses are traced for a few years.

Separation of the response into the baroclinic mode and the surface mode is apparently recognized. The surface mode anomaly is mainly advected by the background quasi-zonal steady circulation. Temporal variation of SST is very sensitive to the horizontal structure of the normal temperature field, due to the advection of temperature by anomalous horizontal currents associated with the Ekman pumping or subsurface temperature anomaly.

概 要

風の応力の変動に対する力学的応答を調べるために海洋大循環モデルを開発した。モデルは矩形で海底は平である。この報告はモデルと計算結果の詳しい記述である。

モデル海域は、東西幅が 100° 、南北が 30°S から 54°N までの緯経線で囲まれた球面で、鉛直 8 層、水平 2° (南北) \times 2.5° (東西) の格子を持つ。東西方向に一樣な風の応力、熱・塩分のフラックスを海面で与え、定常解が得られるまで 140 年間積分する。

風の応力の異常は、(1)赤道海域での東風の弱まりと、(2)熱帯・亜熱帯海域での貿易風の強化を、それぞれ 90 日と 180 日与える。このようにして得られる海水温の変動を数年にわたって追跡、解析する。

その結果、海洋の応答が、傾圧モードと海面モードとに別れることが分かった。海面モードは、おもに定常的な循環場により流される。海面水温 (SST) の時間変動は、エクマン・ポンピングや亜表層の水温変動と関連した水平流による温度移流のため、定常場の水平温度構造にたいへん敏感である。

1. Introduction

Since the 1960's, world general circulation models of the ocean have been developed for the purpose of simulation of the climatological general circulation and SST pattern. On the other hand, basin scale models that were started from barotropic models in the 1960's are mainly intended for the study of simple dynamics with nonlinear effects. Recent increase of scientific interest in dynamic and thermodynamic mechanisms for the long term variation of the upper general circulation has led to more sophisticated basin-scale level models which explicitly deal with thermodynamic processes.

The purpose of the present report is the full description of the idealized and useful numerical model for the study of variation of the general circulation of the upper ocean. After introducing the model, a series of response experiments to the anomalous wind stresses will be described in detail.

2. Description of the Model

2.1 Governing equations

The model is based on the primitive equations formulated in spherical coordinates λ , ϕ , and z , where λ is longitude, ϕ latitude, and z height. The vertical coordinate z is positive upward, with the ocean surface $z=0$. The hydrostatic and Boussinesq approximations are used. Hence, the variation of density is neglected in the momentum equations everywhere except in the buoyancy force. The subgrid-scale processes are parameterized by down-gradient mixing hypothesis, where the exchange coefficients are assumed to be constant. Let u , v , and w be the zonal, meridional, and vertical velocity components, respectively. The equations of horizontal motion are

$$\begin{aligned} \frac{\partial u}{\partial t} + \frac{u}{a \cos \phi} \frac{\partial u}{\partial \lambda} + \frac{v}{a} \frac{\partial u}{\partial \phi} + w \frac{\partial u}{\partial z} - \frac{uv \tan \phi}{a} - 2\Omega v \sin \phi \\ = \frac{-1}{\rho_0 a \cos \phi} \frac{\partial p}{\partial \lambda} + A_m \left\{ \nabla^2 u + \frac{(1 - \tan^2 \phi)}{a^2} u - \frac{2 \sin \phi}{a^2 \cos^2 \phi} \frac{\partial v}{\partial \lambda} \right\} + K_m \frac{\partial^2 u}{\partial z^2}, \end{aligned} \quad (2-1)$$

$$\begin{aligned} \frac{\partial v}{\partial t} + \frac{u}{a \cos \phi} \frac{\partial v}{\partial \lambda} + \frac{v}{a} \frac{\partial v}{\partial \phi} + w \frac{\partial v}{\partial z} + \frac{u^2 \tan \phi}{a} + 2\Omega u \sin \phi \\ = \frac{-1}{\rho_0 a} \frac{\partial p}{\partial \phi} + A_m \left\{ \nabla^2 v + \frac{(1 - \tan^2 \phi)}{a^2} v + \frac{2 \sin \phi}{a^2 \cos^2 \phi} \frac{\partial u}{\partial \lambda} \right\} + K_m \frac{\partial^2 v}{\partial z^2}, \end{aligned} \quad (2-2)$$

and the hydrostatic equation is

$$\frac{\partial p}{\partial z} = -\rho g, \quad (2-3)$$

where t is time, a the earth's radius, Ω the angular velocity of the earth's rotation, ρ_0 a constant reference density, p the pressure, A_m the coefficient of horizontal eddy viscosity, K_m the coefficient of vertical eddy viscosity, ρ the density, g the acceleration of gravity, and ∇^2 the horizontal Laplacian operator,

$$\nabla^2 = \frac{1}{a^2 \cos^2 \phi} \frac{\partial^2}{\partial \lambda^2} + \frac{1}{a^2 \cos \phi} \frac{\partial}{\partial \phi} \left(\cos \phi \frac{\partial}{\partial \phi} \right). \quad (2-4)$$

The equation of continuity is

$$\frac{1}{a \cos \phi} \frac{\partial u}{\partial \lambda} + \frac{1}{a \cos \phi} \frac{\partial}{\partial \phi} (v \cos \phi) + \frac{\partial w}{\partial z} = 0. \quad (2-5)$$

The equations for the conservation of heat and salt are

$$\frac{\partial T}{\partial t} + \frac{u}{a \cos \phi} \frac{\partial T}{\partial \lambda} + \frac{v}{a} \frac{\partial T}{\partial \phi} + w \frac{\partial T}{\partial z} = A_h \nabla^2 T + \frac{K_h}{\delta} \frac{\partial^2 T}{\partial z^2}, \quad (2-6)$$

$$\frac{\partial S}{\partial t} + \frac{u}{a \cos \phi} \frac{\partial S}{\partial \lambda} + \frac{v}{a} \frac{\partial S}{\partial \phi} + w \frac{\partial S}{\partial z} = A_h \nabla^2 S + \frac{K_h}{\delta} \frac{\partial^2 S}{\partial z^2}, \quad (2-7)$$

where T is the temperature, S the salinity, A_h the coefficient of horizontal eddy diffusivity, K_h the coefficient of vertical eddy diffusivity, and the coefficient δ is defined as

$$\delta \equiv \begin{cases} 0 \\ 1 \end{cases} \text{ for } \frac{\partial \rho}{\partial z} \begin{cases} \neq 0 \\ \approx 0 \end{cases}. \quad (2-8)$$

δ is introduced for the convective overturning when the stratification is unstable.

As the equation of state, Eckart's approximation formula (Bryan, 1969b) is used. If ρ , ρ_0 , g , and z are given in cgs units, T in degrees Celsius, and S in parts per thousand, the formula reads

$$\rho = \frac{P' + P_0}{1.000027[A + 0.698(P' + P_0)]}, \quad (2-9)$$

where P' , P_0 , and A are defined as follows :

$$P' = \frac{\rho_0 g |z|}{1.013 \times 10^6} + 1.0,$$

$$P_0 = 5890 + 38T - 0.375T^2 + 3S, \quad (2-10)$$

$$A = 1779.5 + 11.25T - 0.0745T^2 - (3.8 + 0.01T)S.$$

2. 2 Model domain and boundary conditions

The model ocean is bounded by two meridians, 100° of longitude apart, and extends from 30° S to 54° N. It has a flat bottom of 5km depth. This domain is considered as the size of the Pacific Ocean. Fig. 2-1 schematically represents it.

The boundary conditions on the velocity are zero normal velocity and no slip at the western and eastern walls, and zero normal velocity and free slip at the southern and northern walls, i. e.,

$$u = v = 0 \quad \text{at } \lambda = 0^\circ, 100^\circ, \quad (2-11)$$

$$\frac{\partial u}{a \partial \phi} = v = 0 \quad \text{at } \phi = -30^\circ, 54^\circ. \quad (2-12)$$

There is neither heat flux nor salinity flux through the lateral walls, i. e.,

$$\frac{\partial T}{a \cos \phi \partial \lambda} = \frac{\partial S}{a \cos \phi \partial \lambda} = 0 \quad \text{at } \lambda = 0^\circ, 100^\circ, \quad (2-13)$$

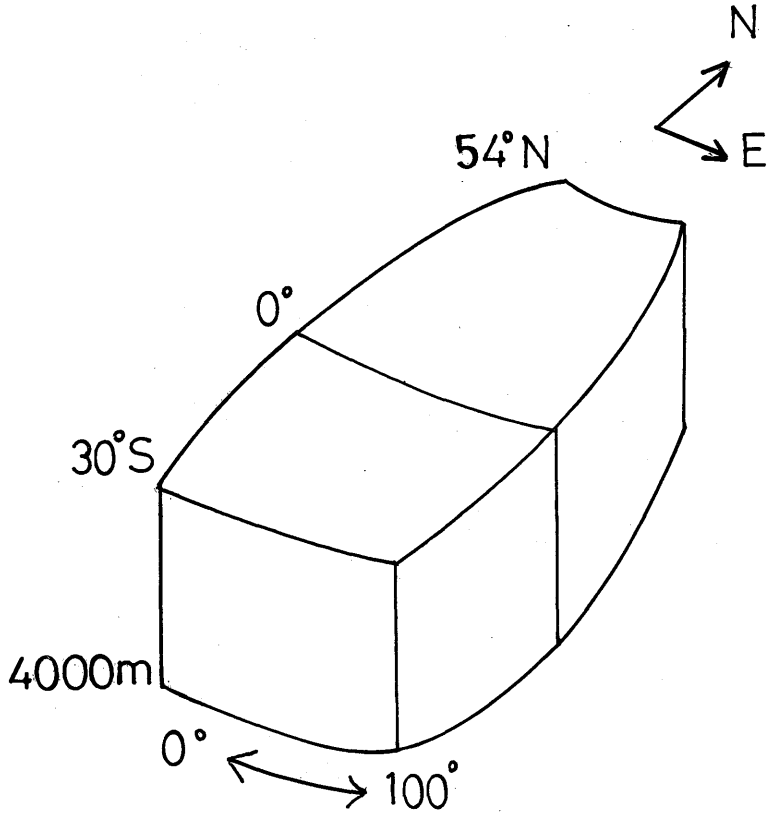


Fig. 2-1 The model domain.

$$\frac{\partial T}{\partial \phi} = \frac{\partial S}{\partial \phi} = 0 \quad \text{at } \phi = -30^\circ, 54^\circ. \quad (2-14)$$

At the ocean bottom, the vertical velocity, heat flux and salinity flux are taken to be zero; thus

$$w = 0, \\ K_h \frac{\partial T}{\partial z} = K_h \frac{\partial S}{\partial z} = 0, \\ \text{at } z = -H. \quad (2-15)$$

$$K_m \frac{\partial u}{\partial z} = \tau_B^u / \rho_0,$$

$$K_m \frac{\partial v}{\partial z} = \tau_B^v / \rho_0.$$

The bottom stress vector (τ_B^u, τ_B^v) is determined on the assumption that the bottom Ekman layer is embedded in the lowest layer of the model ocean in such a way as to satisfy the no-slip condition at the bottom, i. e.,

$$\begin{aligned} \tau_B^\lambda &= \sqrt{\Omega \sin \phi K_m} (u_B - v_B) \\ & \qquad \qquad \qquad (\phi \geq 0), \\ \tau_B^\phi &= \sqrt{\Omega \sin \phi K_m} (u_B + v_B) \\ \text{or} & \\ \tau_B^\lambda &= \sqrt{-\Omega \sin \phi K_m} (u_B + v_B) \\ & \qquad \qquad \qquad (\phi < 0), \\ \tau_B^\phi &= \sqrt{-\Omega \sin \phi K_m} (-u_B + v_B) \end{aligned} \tag{2-16}$$

where u_B and v_B are the horizontal components of the velocity at the lowest layer or at the top of the Ekman layer.

At the ocean surface, the rigid-lid approximation is made to filter out external gravity waves, and the wind stress (τ^λ , τ^ϕ), heat flux (Q_T), and salinity flux (Q_S) are specified, i. e.,

$$\begin{aligned} w &= 0, \\ K_m \frac{\partial u}{\partial z} &= \tau^\lambda / \rho_0, \\ K_m \frac{\partial v}{\partial z} &= \tau^\phi / \rho_0, \qquad \qquad \qquad \text{at } z=0, \\ K_h \frac{\partial T}{\partial z} &= Q_T / \rho_0 c, \\ K_h \frac{\partial S}{\partial z} &= Q_S, \end{aligned} \tag{2-17}$$

where c is the specific heat of the sea water. τ^λ , τ^ϕ , Q_T , and Q_S will be described in section 2.5.

2.3 Prognostic equations

Using the hydrostatic relation (2-3), the pressure at any depth z is given by

$$p = p_s + \int_z^0 g \rho dz, \tag{2-18}$$

where p_s is the pressure at the ocean surface. In terms of p_s , Eqs. (2-1) and (2-2) can be rewritten as

$$\frac{\partial u}{\partial t} = -\frac{1}{\rho_0 a \cos \phi} \frac{\partial p_s}{\partial \lambda} + U + 2\Omega v \sin \phi, \tag{2-19}$$

$$\frac{\partial v}{\partial t} = -\frac{1}{\rho_0 a} \frac{\partial p_s}{\partial \phi} + V - 2\Omega u \sin \phi, \tag{2-20}$$

where

$$\begin{aligned}
 U = & -\frac{1}{\rho_0 a \cos \phi} \frac{\partial}{\partial \lambda} \int_z^0 g \rho dz - \frac{u}{a \cos \phi} \frac{\partial u}{\partial \lambda} - \frac{v}{a} \frac{\partial u}{\partial \phi} - w \frac{\partial u}{\partial z} + \frac{uv \tan \phi}{a} \\
 & + A_m \left\{ \nabla^2 u + \frac{(1 - \tan^2 \phi)}{a^2} u - \frac{2 \sin \phi}{a^2 \cos^2 \phi} \frac{\partial v}{\partial \lambda} \right\} + K_m \frac{\partial^2 u}{\partial z^2}, \quad (2-21)
 \end{aligned}$$

$$\begin{aligned}
 V = & -\frac{1}{\rho_0 a} \frac{\partial}{\partial \phi} \int_z^0 g \rho dz - \frac{u}{a \cos \phi} \frac{\partial v}{\partial \lambda} - \frac{v}{a} \frac{\partial v}{\partial \phi} - w \frac{\partial v}{\partial z} - \frac{u^2 \tan \phi}{a} \\
 & + A_m \left\{ \nabla^2 v + \frac{(1 - \tan^2 \phi)}{a^2} v + \frac{2 \sin \phi}{a^2 \cos^2 \phi} \frac{\partial u}{\partial \lambda} \right\} + K_m \frac{\partial^2 v}{\partial z^2}, \quad (2-22)
 \end{aligned}$$

To integrate the above equations without p_s equation, the horizontal motion (u, v) is decomposed according to Bryan (1969a) as

$$u = \bar{u} + u', \quad (2-23)$$

$$v = \bar{v} + v', \quad (2-24)$$

where \bar{u} and \bar{v} are the vertically averaged velocity components, and u' and v' the deviations from them. By the horizontal nondivergence of the vertical mean current (\bar{u}, \bar{v}), stream function Ψ can be defined such that

$$\bar{u} = \frac{1}{H} \int_{-H}^0 u dz = -\frac{1}{Ha} \frac{\partial \Psi}{\partial \phi}, \quad (2-25)$$

$$\bar{v} = \frac{1}{H} \int_{-H}^0 v dz = \frac{1}{Ha \cos \phi} \frac{\partial \Psi}{\partial \lambda}. \quad (2-26)$$

A prediction equation for Ψ is obtained then by taking the vertical averages of Eqs. (2-19) and (2-20) and eliminating p_s . The result is

$$\begin{aligned}
 & \frac{1}{a^2 \cos^2 \phi} \frac{\partial}{\partial \lambda} \left(\frac{1}{H} \frac{\partial^2 \Psi}{\partial \lambda \partial t} \right) + \frac{1}{a^2 \cos \phi} \frac{\partial}{\partial \phi} \left(\frac{\cos \phi}{H} \frac{\partial^2 \Psi}{\partial \phi \partial t} \right) \\
 & = \frac{1}{a \cos \phi} \frac{\partial}{\partial \lambda} \left\{ \frac{1}{H} \int_{-H}^0 (V - 2\Omega u \sin \phi) dz \right\} \\
 & - \frac{1}{a \cos \phi} \frac{\partial}{\partial \phi} \left\{ \frac{\cos \phi}{H} \int_{-H}^0 (U + 2\Omega v \sin \phi) dz \right\}. \quad (2-27)
 \end{aligned}$$

When H is constant, this equation becomes the Poisson equation :

$$\nabla^2 \frac{1}{H} \frac{\partial \Psi}{\partial t} = \frac{1}{a \cos \phi} \frac{\partial}{\partial \lambda} \left\{ \frac{1}{H} \int_{-H}^0 (V - 2\Omega u \sin \phi) dz \right\}$$

$$-\frac{1}{a \cos \phi} \frac{\partial}{\partial \phi} \left\{ \frac{\cos \phi}{H} \int_{-H}^0 (U + 2\Omega v \sin \phi) dz \right\}. \quad (2-28)$$

From Eqs. (2-19) and (2-20) prediction equations for the vertical shear current are obtained :

$$\frac{\partial u'}{\partial t} = U - \frac{1}{H} \int_{-H}^0 U dz + 2\Omega v' \sin \phi, \quad (2-29)$$

$$\frac{\partial v'}{\partial t} = V - \frac{1}{H} \int_{-H}^0 V dz - 2\Omega u' \sin \phi. \quad (2-30)$$

The temperature and salinity are predicted from Eqs. (2-6) and (2-7), namely,

$$\frac{\partial T}{\partial t} = -\frac{u}{a \cos \phi} \frac{\partial T}{\partial \lambda} - \frac{v}{a} \frac{\partial T}{\partial \phi} - w \frac{\partial T}{\partial z} + A_h \nabla^2 T + \frac{K_h}{\delta} \frac{\partial^2 T}{\partial z^2}, \quad (2-31)$$

$$\frac{\partial S}{\partial t} = -\frac{u}{a \cos \phi} \frac{\partial S}{\partial \lambda} - \frac{v}{a} \frac{\partial S}{\partial \phi} - w \frac{\partial S}{\partial z} + A_h \nabla^2 S + \frac{K_h}{\delta} \frac{\partial^2 S}{\partial z^2}. \quad (2-32)$$

2.4 Grid system and finite difference equations

The finite difference methods used to solve the equations follow those of Semtner (1974), and partly Han (1975). In the following section, the subscripts i , j and k always represent the longitudinal, latitudinal and vertical indices, respectively.

2.4.1 Grid system

The ocean is composed of KM layers, and the grid points are irregularly spaced in the vertical direction. The horizontal spacing of the grid points corresponds to the increments $\Delta \lambda$ and $\Delta \phi$ in the longitudinal and latitudinal directions, respectively.

The arrangement of the variables in the vertical direction is shown in Fig. 2-2. The horizontal velocity components u and v , temperature T , salinity S , density ρ and pressure p are located at the levels denoted by z_k (< 0) ($k=1, \dots, KM$).

The intervals between the levels are defined as

$$\begin{aligned} \Delta z_{1/2} &= -z_1, \\ \Delta z_{k-1/2} &= z_{k-1} - z_k \quad (k=2, \dots, KM), \\ \Delta z_{KM+1/2} &= z_{KM} + H. \end{aligned} \quad (2-33)$$

The thickness of the layers is defined as

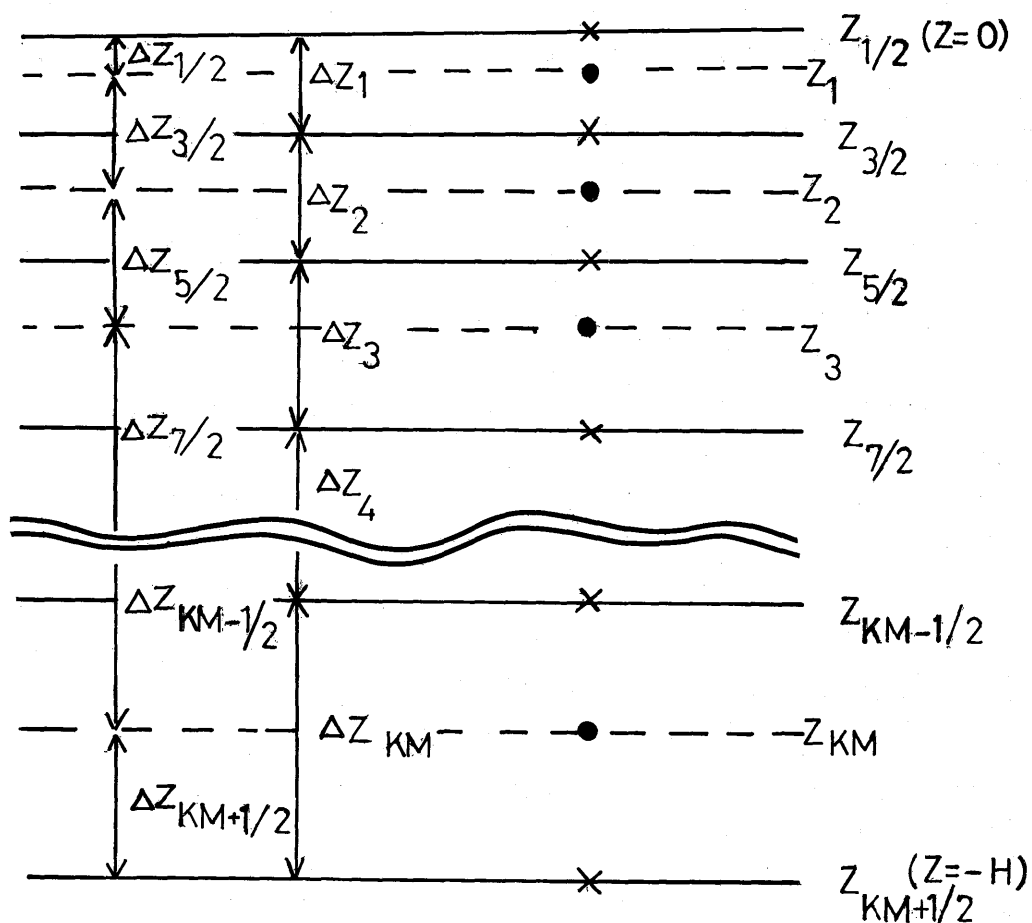


Fig. 2-2 Vertical placement of the variables. Dots are for u, v, T, S, ρ , and p ; crosses are for w .

$$\begin{aligned}
 \Delta z_1 &= \Delta z_{1/2} + 1/2 \Delta z_{3/2}, \\
 \Delta z_k &= 1/2 (\Delta z_{k-1/2} + \Delta z_{k+1/2}) \quad (k=2, \dots, KM-1), \\
 \Delta z_{KM} &= 1/2 \Delta z_{KM-1/2} + \Delta z_{KM+1/2}.
 \end{aligned} \tag{2-34}$$

The vertical velocity w is carried at the intermediate levels

$$z_{k+1/2} (k=0, \dots, KM),$$

where

$$\begin{aligned}
 z_{1/2} &= 0, \\
 z_{k+1/2} &= 1/2 (z_k + z_{k+1}) \quad (k=1, \dots, KM-1),
 \end{aligned} \tag{2-35}$$

$$z_{KM+1/2} = -H .$$

A staggered grid system in the horizontal plane is shown in Fig. 2-3. The temperature T , salinity S , density ρ , pressure p , and stream function Ψ are located at integer grid points (i, j) ($i=1, \dots, IM, j=1, \dots, JM$), where IM and JM are the total numbers of grid points in the longitudinal and latitudinal directions, respectively. The horizontal velocity components u and v are located at half-integer grid points $(i+1/2, j+1/2)$ ($i=1, \dots, IM-1, j=1, \dots, JM-1$). The vertical velocity in the prognostic equations for T and S is evaluated at (i, j) , while that for u and v is evaluated at $(i+1/2, j+1/2)$. The coastlines of the model ocean are placed on (i, j) points, that is, $(2, j), (IM-1, j)$ ($j=2, \dots, JM-1$), and $(i, 2), (i, JM-1)$ ($i=2, \dots, IM-1$). The grid points outside the coastlines are only used for specifying boundary conditions. The horizontal grid distances $\Delta x_j, \Delta x_{j+1/2}$, and Δy are defined as

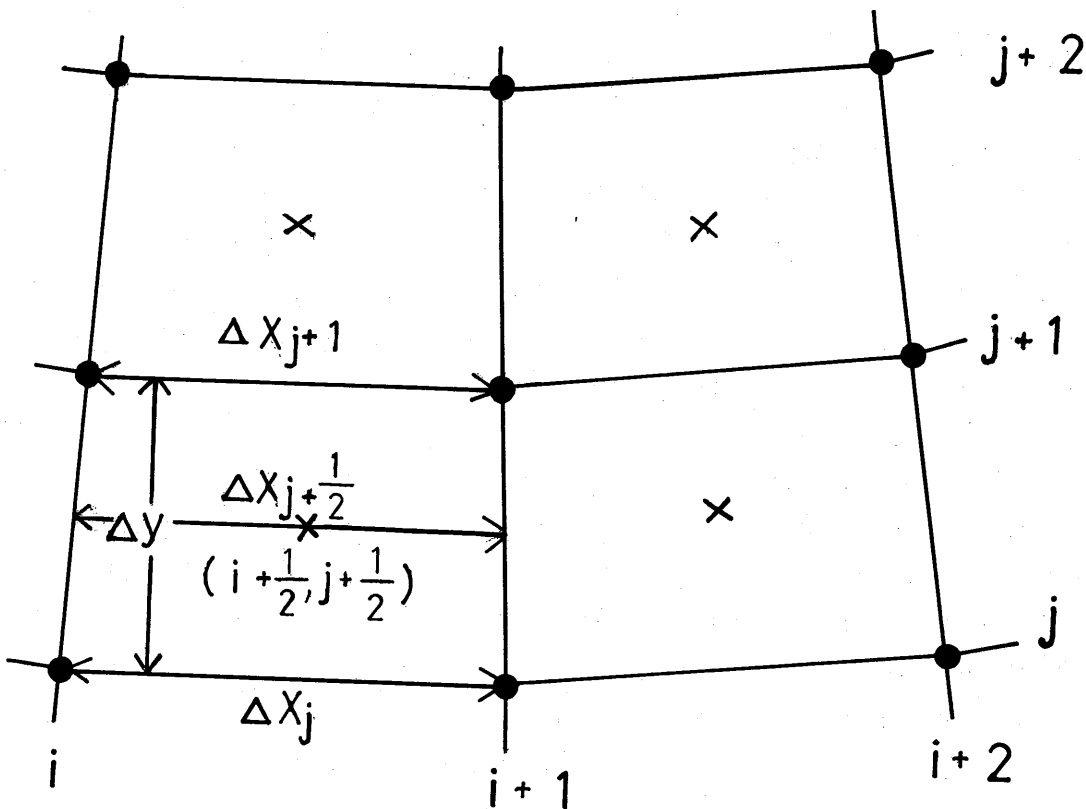


Fig. 2-3 Horizontal placement of the variables. Dots are for T, S, ρ, p, Ψ , and w in the T and S equations; crosses are for u, v , and w in the u and v equations.

$$\begin{aligned} \Delta x_j &= a \cos \phi_j \Delta \lambda, \\ \Delta x_{j+1/2} &= 1/2 (\Delta x_j + \Delta x_{j+1}), \\ \Delta y &= a \Delta \phi. \end{aligned} \tag{2-36}$$

where ϕ_j is the latitude of j point. The trigonometric functions at $j+1/2$ point are given using $\cos \phi_j$ at j point by

$$\begin{aligned} \cos \phi_{j+1/2} &= 1/2 (\cos \phi_j + \cos \phi_{j+1}), \\ \sin \phi_{j+1/2} &= (\cos \phi_j - \cos \phi_{j+1}) / \Delta y, \\ \tan \phi_{j+1/2} &= \sin \phi_{j+1/2} / \cos \phi_{j+1/2}. \end{aligned} \tag{2-37}$$

The area elements Π_j and $\Pi_{j+1/2}$ are defined as

$$\begin{aligned} \Pi_j &= \Delta x_j \Delta y, \\ \Pi_{j+1/2} &= \Delta x_{j+1/2} \Delta y. \end{aligned} \tag{2-38}$$

2.4.2 Time differencing

The principal time differencing utilized in the model is the leapfrog scheme. Every ten time steps, however, a forward scheme is applied to suppress the time splitting associated with the leapfrog scheme. The friction and diffusion terms are always evaluated with a forward scheme. In addition, a trapezoidal implicit scheme is used for the Coriolis terms in order to render inertial oscillations stable with a long time step.

2.4.3 Momentum equations

The finite difference analogs of the equations of motion for the vertical shear current are obtained by rendering Eqs. (2-29) and (2-30) in the finite difference form. In this subsection, notation α is used to denote either u or v .

(a) Pressure gradient

The pressure gradient forces at the k th level relative to those at the first level are written as

$$\begin{aligned} (P\lambda)_{i+1/2, j+1/2, 1} &= 0, \\ (P\lambda)_{i+1/2, j+1/2, k} &= -\frac{1}{2} \frac{1}{\rho_0} \sum_{l=1}^{k-1} (\rho_{i+1, j+1, l+1/2} + \rho_{i+1, j, l+1/2} - \rho_{i, j+1, l+1/2} - \rho_{i, j, l+1/2}) \end{aligned} \tag{2-39}$$

$$\cdot g \Delta z_{l+1/2} / \Delta x_{j+1/2} \quad (k=2, \dots, KM),$$

and

$$(P\phi)_{i+1/2, j+1/2, 1} = 0,$$

$$(P\phi)_{i+1/2, j+1/2, k} = -\frac{1}{2} \frac{1}{\rho_0} \sum_{l=1}^{k-1} (\rho_{i+1, j+1, l+1/2} + \rho_{i, j+1, l+1/2} - \rho_{i+1, j, l+1/2} - \rho_{i, j, l+1/2})$$

$$\cdot g \Delta z_{l+1/2} / \Delta y \quad (k=2, \dots, KM),$$
(2-40)

where $\rho_{i, j, k+1/2}$ is defined as

$$\rho_{i, j, k+1/2} = \frac{1}{2} (\rho_{i, j, k} + \rho_{i, j, k+1}),$$
(2-41)

and the density $\rho_{i, j, k}$ is calculated from the equation of state (2-9) with $T_{i, j, k}$, $S_{i, j, k}$ and z_k .

(b) Horizontal advection

It is convenient to define the following volume fluxes per unit depth in advance (Fig. 2-4

(a)):

$$(FUC)_{i, j, k} = \frac{1}{4} \Delta y (u_{i-1/2, j-1/2, k} + u_{i+1/2, j-1/2, k} + u_{i-1/2, j+1/2, k} + u_{i+1/2, j+1/2, k}),$$

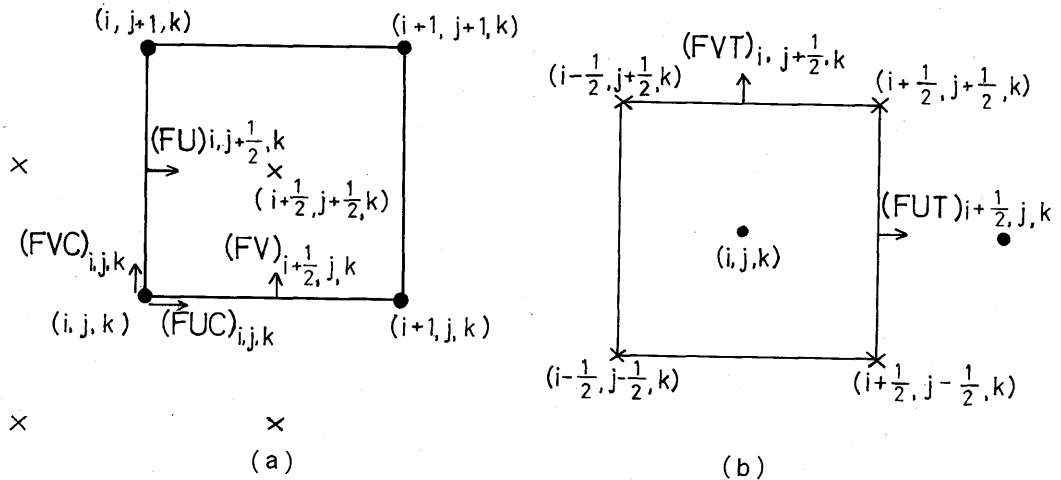


Fig. 2-4 Location of the horizontal volume fluxes defined to obtain finite-difference forms of the horizontal advection terms in (a) the momentum equations and (b) temperature and salinity equations.

$$(FVC)_{i,j,k} = \frac{1}{4} \{ \Delta x_{j-1/2} (v_{i-1/2,j-1/2,k} + v_{i+1/2,j-1/2,k}) + \Delta x_{j+1/2} (v_{i-1/2,j+1/2,k} + v_{i+1/2,j+1/2,k}) \}, \quad (2-42)$$

$$(FU)_{i,j+1/2,k} = \frac{1}{2} \{ (FUC)_{i,j,k} + (FUC)_{i,j+1,k} \},$$

$$(FV)_{i+1/2,j,k} = \frac{1}{2} \{ (FVC)_{i,j,k} + (FVC)_{i+1,j,k} \}.$$

Then the horizontal advection terms are given by

$$(M\lambda)_{i+1/2,j+1/2,k} = -\frac{1}{\Pi_{j+1/2}} \left[\frac{2}{3} \{ (uu)_{i+1,j+1/2,k} - (uu)_{i,j+1/2,k} + (uv)_{i+1/2,j+1,k} - (uv)_{i+1/2,j,k} \} + \frac{1}{3} \{ (uc)_{i+1,j+1,k} - (uc)_{i,j,k} + (uc)_{i,j+1,k} - (uc)_{i+1,j,k} \} \right], \quad (2-43)$$

$$(M\phi)_{i+1/2,j+1/2,k} = -\frac{1}{\Pi_{j+1/2}} \left[\frac{2}{3} \{ (vu)_{i+1,j+1/2,k} - (vu)_{i,j+1/2,k} + (vv)_{i+1/2,j+1,k} - (vv)_{i+1/2,j,k} \} + \frac{1}{3} \{ (vc)_{i+1,j+1,k} - (vc)_{i,j,k} + (vc)_{i,j+1,k} - (vc)_{i+1,j,k} \} \right],$$

where

$$(au)_{i,j+1/2,k} = \frac{1}{2} (\alpha_{i-1/2,j+1/2,k} + \alpha_{i+1/2,j+1/2,k}) (FU)_{i,j+1/2,k},$$

$$(av)_{i+1/2,j,k} = \frac{1}{2} (\alpha_{i+1/2,j-1/2,k} + \alpha_{i+1/2,j+1/2,k}) (FV)_{i+1/2,j,k},$$

$$(ac)_{i+1,j+1,k} = \frac{1}{4} (\alpha_{i+1/2,j+1/2,k} + \alpha_{i+3/2,j+3/2,k}) \{ (FUC)_{i+1,j+1,k} + (FVC)_{i+1,j+1,k} \}, \quad (2-44)$$

$$(ac)_{i,j,k} = \frac{1}{4} (\alpha_{i-1/2,j-1/2,k} + \alpha_{i+1/2,j+1/2,k}) \{ (FUC)_{i,j,k} + (FVC)_{i,j,k} \},$$

$$(ac)_{i,j+1,k} = \frac{1}{4} (\alpha_{i+1/2,j+1/2,k} + \alpha_{i-1/2,j+3/2,k}) \{ -(FUC)_{i,j+1,k} + (FVC)_{i,j+1,k} \},$$

$$(ac)_{i+1,j,k} = \frac{1}{4} (\alpha_{i+1/2,j+1/2,k} + \alpha_{i+3/2,j-1/2,k}) \{ -(FUC)_{i+1,j,k} + (FVC)_{i+1,j,k} \}.$$

(c) Vertical advection

Using the equation of continuity (2-5) and the upper boundary condition (2-17), the

vertical velocity at $(i+1/2, j+1/2, k+1/2)$ is given by

$$w_{i+1/2, j+1/2, 1/2} = 0,$$

$$w_{i+1/2, j+1/2, k+1/2} = \frac{1}{\prod_{l=1}^k} \{ (FU)_{i+1, j+1/2, l} - (FU)_{i, j+1/2, l} + (FV)_{i+1/2, j+1, l} - (FV)_{i+1/2, j, l} \} \Delta z_l \quad (k=1, \dots, KM). \quad (2-45)$$

Then the vertical advection terms are written as

$$(W\lambda)_{i+1/2, j+1/2, k} = - \{ (uw)_{i+1/2, j+1/2, k-1/2} - (uw)_{i+1/2, j+1/2, k+1/2} \} / \Delta z_k,$$

$$(W\phi)_{i+1/2, j+1/2, k} = - \{ (vw)_{i+1/2, j+1/2, k-1/2} - (vw)_{i+1/2, j+1/2, k+1/2} \} / \Delta z_k,$$
(2-46)

where

$$(aw)_{i+1/2, j+1/2, k+1/2} = \frac{1}{2} (\alpha_{i+1/2, j+1/2, k} + \alpha_{i+1/2, j+1/2, k+1}) \cdot w_{i+1/2, j+1/2, k+1/2}. \quad (2-47)$$

(d) Horizontal friction

The finite difference analogs of the horizontal friction terms are

$$(F\lambda)_{i+1/2, j+1/2, k} = A_m \left\{ (\nabla^2 u)_{i+1/2, j+1/2, k} + \frac{(1 - \tan^2 \phi_{j+1/2})}{a^2} u_{i+1/2, j+1/2, k} - \frac{\sin \phi_{j+1/2}}{a^2 \cos^2 \phi_{j+1/2}} \cdot \frac{v_{i+3/2, j+1/2, k} - v_{i-1/2, j+1/2, k}}{\Delta x_{j+1/2}} \right\},$$

$$(F\phi)_{i+1/2, j+1/2, k} = A_m \left\{ (\nabla^2 v)_{i+1/2, j+1/2, k} + \frac{(1 - \tan^2 \phi_{j+1/2})}{a^2} v_{i+1/2, j+1/2, k} + \frac{\sin \phi_{j+1/2}}{a^2 \cos^2 \phi_{j+1/2}} \cdot \frac{u_{i+3/2, j+1/2, k} - u_{i-1/2, j+1/2, k}}{\Delta x_{j+1/2}} \right\},$$
(2-48)

where

$$(\nabla^2 \alpha)_{i+1/2, j+1/2, k} = \{ (\alpha_{i+3/2, j+1/2, k} - \alpha_{i+1/2, j+1/2, k}) - (\alpha_{i+1/2, j+1/2, k} - \alpha_{i-1/2, j+1/2, k}) \} / \Delta x_{j+1/2}^2$$

$$+ \{ \cos \phi_{j+1} (\alpha_{i+1/2, j+3/2, k} - \alpha_{i+1/2, j+1/2, k}) - \cos \phi_j (\alpha_{i+1/2, j+1/2, k} - \alpha_{i+1/2, j-1/2, k}) \} / \cos \phi_{j+1/2} \Delta y^2. \quad (2-49)$$

(e) Vertical friction

The vertical friction terms are written in the following finite difference form :

$$(G\lambda)_{i+1/2, j+1/2, k} = \{ (Du)_{i+1/2, j+1/2, k-1/2} - (Du)_{i+1/2, j+1/2, k+1/2} \} / \Delta z_k,$$

$$(G\phi)_{i+1/2, j+1/2, k} = \{ (Dv)_{i+1/2, j+1/2, k-1/2} - (Dv)_{i+1/2, j+1/2, k+1/2} \} / \Delta z_k,$$
(2-50)

where

$$(Da)_{i+1/2, j+1/2, k+1/2} = K_m(\alpha_{i+1/2, j+1/2, k} - \alpha_{i+1/2, j+1/2, k}) / \Delta z_{k+1/2}. \quad (2-51)$$

From the above, the finite difference analogs of Eqs. (2-29) and (2-30) for u' and v' at the time level $n+1$ are

$$\begin{aligned} \frac{u'_{i+1/2, j+1/2, k}^{(n+1)} - u'_{i+1/2, j+1/2, k}^{(n-1)}}{2 \Delta t} &= U_{i+1/2, j+1/2, k}^{(n, n-1)} - \frac{1}{H} \sum_{l=1}^{KM} U_{i+1/2, j+1/2, l}^{(n, n-1)} \Delta z_l \\ &+ 2\Omega \sin \phi_{j+1/2} (\beta v'_{i+1/2, j+1/2, k}^{(n+1)} + \gamma v'_{i+1/2, j+1/2, k}^{(n-1)}), \end{aligned} \quad (2-52)$$

$$\begin{aligned} \frac{v'_{i+1/2, j+1/2, k}^{(n+1)} - v'_{i+1/2, j+1/2, k}^{(n-1)}}{2 \Delta t} &= V_{i+1/2, j+1/2, k}^{(n, n-1)} - \frac{1}{H} \sum_{l=1}^{KM} V_{i+1/2, j+1/2, l}^{(n, n-1)} \Delta z_l \\ &- 2\Omega \sin \phi_{j+1/2} (\beta u'_{i+1/2, j+1/2, k}^{(n+1)} + \gamma u'_{i+1/2, j+1/2, k}^{(n-1)}), \end{aligned} \quad (2-53)$$

where

$$\begin{aligned} U_{i+1/2, j+1/2, k}^{(n, n-1)} &= (P\lambda)_{i+1/2, j+1/2, k}^{(n)} + (M\lambda)_{i+1/2, j+1/2, k}^{(n)} + (W\lambda)_{i+1/2, j+1/2, k}^{(n)} \\ &+ \frac{\tan \phi_{j+1/2}}{a} u_{i+1/2, j+1/2, k}^{(n)} \cdot v_{i+1/2, j+1/2, k}^{(n)} \\ &+ (F\lambda)_{i+1/2, j+1/2, k}^{(n-1)} + (G\lambda)_{i+1/2, j+1/2, k}^{(n-1)}, \end{aligned} \quad (2-54)$$

$$\begin{aligned} V_{i+1/2, j+1/2, k}^{(n, n-1)} &= (P\phi)_{i+1/2, j+1/2, k}^{(n)} + (M\phi)_{i+1/2, j+1/2, k}^{(n)} + (W\phi)_{i+1/2, j+1/2, k}^{(n)} \\ &- \frac{\tan \phi_{j+1/2}}{a} (u_{i+1/2, j+1/2, k}^{(n)})^2 \\ &+ (F\phi)_{i+1/2, j+1/2, k}^{(n-1)} + (G\phi)_{i+1/2, j+1/2, k}^{(n-1)}, \end{aligned} \quad (2-55)$$

and superscript n indicates the time level n of the variable, and Δt denotes a time increment. Eqs. (2-52) and (2-53) are solved simultaneously for $u'_{i+1/2, j+1/2, k}^{(n+1)}$ and $v'_{i+1/2, j+1/2, k}^{(n+1)}$. The coefficients β and γ are taken to be 0.5 so that inertial oscillations are computationally neutral.

When the forward time difference is applied, the variables at time level $n-1$ in Eqs. (2-52) and (2-53) are replaced by those at time level n , and the denominator $2 \Delta t$ on the lefthand side is replaced by Δt .

2.4.4 Temperature and salinity equations

As the temperature equation (2-31) and salinity equation (2-32) are similar to each other, only the finite difference analog of the temperature equation is written here.

(a) Horizontal advection

It is convenient to define the following volume fluxes per unit depth (see Fig. 2-4 (b)) :

$$(FUT)_{i+1/2, j, k} = \frac{1}{2} \Delta y (u_{i+1/2, j-1/2, k} + u_{i+1/2, j+1/2, k}), \quad (2-56)$$

$$(FVT)_{i, j+1/2, k} = \frac{1}{2} \Delta x_{j+1/2} (v_{i-1/2, j+1/2, k} + v_{i+1/2, j+1/2, k}).$$

Then the horizontal advection terms are given as

$$(M_T)_{i, j, k} = -\frac{1}{H_j} \{ (Tu)_{i+1/2, j, k} - (Tu)_{i-1/2, j, k} + (Tv)_{i, j+1/2, k} - (Tv)_{i, j-1/2, k} \}, \quad (2-57)$$

where

$$(Tu)_{i+1/2, j, k} = \frac{1}{2} (T_{i, j, k} + T_{i+1, j, k}) (FUT)_{i+1/2, j, k}, \quad (2-58)$$

$$(Tv)_{i, j+1/2, k} = \frac{1}{2} (T_{i, j, k} + T_{i, j+1, k}) (FVT)_{i, j+1/2, k}.$$

(b) Vertical advection

The vertical velocity at $(i, j, k+1/2)$ is given by

$$w_{i, j, 1/2} = 0, \quad (2-59)$$

$$w_{i, j, k+1/2} = \frac{1}{H_j} \sum_{l=1}^k \{ (FUT)_{i+1/2, j, l} - (FUT)_{i-1/2, j, l} + (FVT)_{i, j+1/2, l} - (FVT)_{i, j-1/2, l} \} \Delta z_l \quad (k=1, \dots, KM).$$

Then the vertical advection term is written as

$$(W_T)_{i, j, k} = - \{ (Tw)_{i, j, k-1/2} - (Tw)_{i, j, k+1/2} \} / \Delta z_k, \quad (2-60)$$

where

$$(Tw)_{i, j, k+1/2} = \frac{1}{2} (T_{i, j, k} + T_{i, j, k+1}) \cdot w_{i, j, k+1/2}. \quad (2-61)$$

The vertical velocity $w_{i+1/2, j+1/2, k+1/2}$ evaluated by Eq. (2-45) is related to $w_{i, j, k+1/2}$ by the following equation :

$$\begin{aligned} \cos\phi_{j+1/2} w_{i+1/2, j+1/2, k+1/2} = & \frac{1}{4} \{ \cos\phi_j (w_{i, j, k+1/2} + w_{i+1, j, k+1/2}) \\ & + \cos\phi_{j+1} (w_{i, j+1, k+1/2} + w_{i+1, j+1, k+1/2}) \}. \end{aligned} \quad (2-62)$$

(c) Horizontal diffusion

The finite difference analog of the horizontal diffusion term is

$$\begin{aligned} (F_T)_{i, j, k} = & A_h \{ [(T_{i+1, j, k} - T_{i, j, k}) - (T_{i, j, k} - T_{i-1, j, k})] / \Delta x_j^2 \\ & + \{ \cos\phi_{j+1/2} (T_{i, j+1, k} - T_{i, j, k}) \\ & - \cos\phi_{j-1/2} (T_{i, j, k} - T_{i, j-1, k}) \} / \cos\phi_j \Delta y^2 \}. \end{aligned} \quad (2-63)$$

(d) Vertical diffusion

The vertical diffusion term is written as

$$(G_T)_{i, j, k} = \{ (DT)_{i, j, k-1/2} - (DT)_{i, j, k+1/2} \} / \Delta z_k, \quad (2-64)$$

where

$$(DT)_{i, j, k+1/2} = K_h (T_{i, j, k} - T_{i, j, k+1}) / \Delta z_{k+1/2}. \quad (2-65)$$

T and S at time level $n+1$ are obtained from

$$\frac{T_{i, j, k}^{(n+1)} - T_{i, j, k}^{(n-1)}}{2 \Delta t} = (M_T)_{i, j, k}^{(n)} + (W_T)_{i, j, k}^{(n)} + (F_T)_{i, j, k}^{(n-1)} + (G_T)_{i, j, k}^{(n-1)} + (\delta_T)_{i, j, k}^{(n+1)}, \quad (2-66)$$

$$\frac{S_{i, j, k}^{(n+1)} - S_{i, j, k}^{(n-1)}}{2 \Delta t} = (M_S)_{i, j, k}^{(n)} + (W_S)_{i, j, k}^{(n)} + (F_S)_{i, j, k}^{(n-1)} + (G_S)_{i, j, k}^{(n-1)} + (\delta_S)_{i, j, k}^{(n+1)}, \quad (2-67)$$

where $(M_S)_{i, j, k}$, $(W_S)_{i, j, k}$, $(F_S)_{i, j, k}$ and $(G_S)_{i, j, k}$ are counterparts of $(M_T)_{i, j, k}$, $(W_T)_{i, j, k}$, $(F_T)_{i, j, k}$ and $(G_T)_{i, j, k}$, respectively. $(\delta_T)_{i, j, k}^{(n+1)}$ and $(\delta_S)_{i, j, k}^{(n+1)}$ represent time rate of change due to the convective adjustment. If the new density field, which is calculated from the temperature and salinity field without δ terms, contains a statically unstable stratification, $\rho_{i, j, k-1}^{(n+1)} > \rho_{i, j, k}^{(n+1)}$, the temperatures $T_{i, j, k-1}^{(n+1)}$ and $T_{i, j, k}^{(n+1)}$ and salinities $S_{i, j, k-1}^{(n+1)}$ and $S_{i, j, k}^{(n+1)}$ are replaced by the respective weighted mean values.

2.4.5 Boundary conditions

The lateral boundary conditions only for the western boundary ($i=2$) and southern boundary ($j=2$) are given, since the eastern boundary ($i=IM-1$) and northern boundary

($j=JM-1$) are treated similarly.

The condition of zero normal velocity is maintained by imposing antisymmetric conditions on the normal velocity component :

$$\begin{aligned} u_{3/2, j+1/2, k}^{(n)} &= -u_{5/2, j+1/2, k}^{(n)}, \\ v_{i+1/2, 3/2, k}^{(n)} &= -v_{i+1/2, 5/2, k}^{(n)}. \end{aligned} \quad (2-68)$$

For the tangential velocity component, symmetric conditions are imposed :

$$\begin{aligned} v_{3/2, j+1/2, k}^{(n)} &= v_{5/2, j+1/2, k}^{(n)}, \\ u_{i+1/2, 3/2, k}^{(n)} &= u_{i+1/2, 5/2, k}^{(n)}. \end{aligned} \quad (2-69)$$

In the friction terms, the no-slip condition at the western boundary is satisfied by the antisymmetric conditions :

$$\begin{aligned} u_{3/2, j+1/2, k}^{(n-1)} &= -u_{5/2, j+1/2, k}^{(n-1)}, \\ v_{3/2, j+1/2, k}^{(n-1)} &= -v_{5/2, j+1/2, k}^{(n-1)}. \end{aligned} \quad (2-70)$$

The free-slip condition at the southern boundary is satisfied by the symmetric conditions

$$\begin{aligned} u_{i+1/2, 3/2, k}^{(n-1)} &= u_{i+1/2, 5/2, k}^{(n-1)}, \\ v_{i+1/2, 3/2, k}^{(n-1)} &= v_{i+1/2, 5/2, k}^{(n-1)}. \end{aligned} \quad (2-71)$$

On the temperature and salinity, the following symmetric conditions are imposed both in the advection and diffusion terms :

$$\begin{aligned} T_{1, j, k}^{(n)} &= T_{3, j, k}^{(n)}, \quad T_{1, j, k}^{(n-1)} = T_{3, j, k}^{(n-1)}, \quad T_{i, 1, k}^{(n)} = T_{i, 3, k}^{(n)}, \quad T_{i, 1, k}^{(n-1)} = T_{i, 3, k}^{(n-1)}, \\ S_{1, j, k}^{(n)} &= S_{3, j, k}^{(n)}, \quad S_{1, j, k}^{(n-1)} = S_{3, j, k}^{(n-1)}, \quad S_{i, 1, k}^{(n)} = S_{i, 3, k}^{(n)}, \quad S_{i, 1, k}^{(n-1)} = S_{i, 3, k}^{(n-1)}. \end{aligned} \quad (2-72)$$

The conditions at the ocean bottom are, referring to Eqs. (2-51) and (2-65), satisfied by setting as follows :

$$\begin{aligned} w_{i, j, KM+1/2}^{(n)} &= w_{i+1/2, j+1/2, KM+1/2}^{(n)} = 0, \\ (Du)_{i+1/2, j+1/2, KM+1/2}^{(n-1)} &= (\tau_B^{\lambda})_{i+1/2, j+1/2}^{(n-1)} / \rho_0, \\ (Dv)_{i+1/2, j+1/2, KM+1/2}^{(n-1)} &= (\tau_B^{\phi})_{i+1/2, j+1/2}^{(n-1)} / \rho_0, \\ (DT)_{i, j, KM+1/2}^{(n-1)} &= (DS)_{i, j, KM+1/2}^{(n-1)} = 0. \end{aligned} \quad (2-73)$$

At the ocean surface, the following conditions are imposed :

$$\begin{aligned}
 w_{i,j,1/2}^{(n)} &= w_{i+1/2,j+1/2,1/2}^{(n)} = 0, \\
 (Du)_{i+1/2,j+1/2,1/2}^{(n-1)} &= (\tau^\lambda)_{i+1/2,j+1/2}^{(n-1)} / \rho_0, \\
 (Dv)_{i+1/2,j+1/2,1/2}^{(n-1)} &= (\tau^\theta)_{i+1/2,j+1/2}^{(n-1)} / \rho_0, \\
 (DT)_{i,j,1/2}^{(n-1)} &= (Q_T)_{i,j}^{(n-1)} / \rho_0 c, \\
 (DS)_{i,j,1/2}^{(n-1)} &= (Q_S)_{i,j}^{(n-1)} / \rho_0.
 \end{aligned} \tag{2-74}$$

2.4.6 Vorticity equation

The finite difference analog of Eq. (2-28) for the stream function is

$$\begin{aligned}
 L(q_{i,j}) &= ZTD_{i,j} \\
 &= \frac{1}{2\Delta x_j} (VM_{i+1/2,j+1/2} + VM_{i+1/2,j-1/2} - VM_{i-1/2,j+1/2} - VM_{i-1/2,j-1/2}) \\
 &\quad - \frac{1}{2\cos\phi_j \Delta y} \{ \cos\phi_{j+1/2} (UM_{i-1/2,j+1/2} + UM_{i+1/2,j+1/2}) \\
 &\quad \quad - \cos\phi_{j-1/2} (UM_{i-1/2,j-1/2} + UM_{i+1/2,j-1/2}) \},
 \end{aligned} \tag{2-75}$$

where L denotes the finite difference analog of the Laplacian operator ∇^2 ,

$$\begin{aligned}
 L(q_{i,j}) &= \frac{1}{\Delta x_j^2} (q_{i+1,j} + q_{i-1,j} - 2q_{i,j}) \\
 &\quad + \frac{1}{\cos\phi_j \Delta y^2} \{ \cos\phi_{j+1/2} (q_{i,j+1} - q_{i,j}) - \cos\phi_{j-1/2} (q_{i,j} - q_{i,j-1}) \},
 \end{aligned} \tag{2-76}$$

and

$$\begin{aligned}
 q_{i,j} &= \frac{\Psi_{i,j}^{(n+1)} - \Psi_{i,j}^{(n-1)}}{2\Delta t H}, \\
 UM_{i+1/2,j+1/2} &= \frac{1}{H} \sum_{k=1}^{KM} (U_{i+1/2,j+1/2,k}^{(n,n-1)} + 2\Omega \sin\phi_{j+1/2} \cdot v_{i+1/2,j+1/2,k}^{(n)}) \Delta z_k, \\
 VM_{i+1/2,j+1/2} &= \frac{1}{H} \sum_{k=1}^{KM} (V_{i+1/2,j+1/2,k}^{(n,n-1)} - 2\Omega \sin\phi_{j+1/2} \cdot u_{i+1/2,j+1/2,k}^{(n)}) \Delta z_k.
 \end{aligned} \tag{2-77}$$

The difference equation (2-76) is solved together with the boundary conditions, $q_{i,j} = 0$ along the lateral boundaries.

In the present model, the following Fourier direct method (Williams, 1969) is used to solve the Poisson equation. Let

$$q_{i,j} = \sum_{l=3}^{IM-2} Q_{l,j} \sin \left\{ \frac{(l-2)(i-2)}{IM-3} \pi \right\}, \tag{2-78}$$

then Eq. (2-75) may be written after a little manipulation as

$$\begin{aligned} & \frac{\cos\phi_{j-1/2}}{R_j \cos\phi_j \Delta y^2} Q_{l,j-1} + \left[\frac{2}{R_j \Delta x_j^2} \cos\left\{ \frac{(l-2)}{IM-3} \pi \right\} - 1 \right] Q_{l,j} + \frac{\cos\phi_{j+1/2}}{R_j \cos\phi_j \Delta y^2} Q_{l,j+1} \\ & = \frac{2}{IM-3} \sum_{i=3}^{IM-2} \sin\left\{ \frac{(l-2)(i-2)}{IM-3} \pi \right\} \frac{ZTD_{i,j}}{R_j}, \end{aligned} \quad (2-79)$$

where

$$R_j = \frac{2}{\Delta x_j^2} + \frac{\cos\phi_{j-1/2} + \cos\phi_{j+1/2}}{\cos\phi_j \Delta y^2}. \quad (2-80)$$

The equation (2-79) is solved for the Fourier coefficient $Q_{i,j}$. Then the stream function tendency $q_{i,j}$ can be obtained from $Q_{i,j}$ through Eq. (2-78).

2.4.7 Programming

The computer program for the model is coded according to the program flow of Semtner (1974), and changed to take advantage of the array processor.

To check the coding of the program, volume integrals over the entire basin of the terms in the temperature and salinity equations (2-66) and (2-67) are taken on a certain time step. The integrals of the advective terms and of the horizontal diffusion terms should be essentially zero. The integrals of the vertical diffusion terms should also be zero except the surface flux terms. Thus the time changes of the volume integrals of temperature and salinity must be equal to the surface fluxes to within truncation error.

A further check is made as to the energy balance. The time change of the volume averaged kinetic energy of the vertical shear current is derived from Eqs. (2-29) and (2-30) as

$$\frac{1}{V} \int_V \frac{\partial}{\partial t} \left(\frac{u'^2 + v'^2}{2} \right) dm = \frac{1}{V} \int_V (u'U + v'V) dm = \sum_{i=1}^7 E_i', \quad (2-81)$$

where V denotes the total volume of the model ocean. For the time change of the kinetic energy of the vertical mean current, the following equation is derived from Eq. (2-28):

$$\begin{aligned} & \frac{1}{S} \int_S \frac{\partial}{\partial t} \left(\frac{\bar{u}^2 + \bar{v}^2}{2} \right) ds = -\frac{1}{V} \int_S \Psi ZTD ds \\ & = -\frac{1}{V} \int_S \Psi \left\{ \frac{1}{a \cos\phi} \frac{\partial \bar{V}}{\partial \lambda} - \frac{1}{a \cos\phi} \frac{\partial}{\partial \phi} \cdot (\cos\phi \bar{U}) \right\} ds \\ & = \sum_{i=1}^7 \bar{E}_i, \end{aligned} \quad (2-82)$$

where S denotes the area of the ocean and ZTD the righthand side of Eq. (2-28). E'_1 and \bar{E}_1 represent the contributions associated with the horizontal pressure gradient E'_1 and \bar{E}_1 , horizontal advection E'_2 and \bar{E}_2 , vertical advection E'_3 and \bar{E}_3 , horizontal diffusion E'_4 and \bar{E}_4 , vertical diffusion E'_5 and \bar{E}_5 , wind stress E'_6 and \bar{E}_6 , and bottom friction E'_7 and \bar{E}_7 , respectively. The contribution associated with the metric terms is included in E'_2 and \bar{E}_2 . \bar{E}_1 and \bar{E}_5 should be zero. The equality (2-81) must hold except for a small residual, which comes from the semi-implicit treatment of the Coriolis terms. Furthermore, the following relations which represent the transformation of kinetic energy from the vertical shear component to the vertically uniform component and the transformation of potential energy to shear kinetic energy must hold :

$$\begin{aligned}
 E'_2 + E'_3 &= \frac{1}{V} \int_V \left\{ u' \left(-\frac{u}{a \cos \phi} \frac{\partial u}{\partial \lambda} - \frac{v}{a} \frac{\partial u}{\partial \phi} - w \frac{\partial u}{\partial z} + \frac{uv}{a} \tan \phi \right) \right. \\
 &\quad \left. + v' \left(-\frac{u}{a \cos \phi} \frac{\partial v}{\partial \lambda} - \frac{v}{a} \frac{\partial v}{\partial \phi} - w \frac{\partial v}{\partial z} - \frac{u^2 \tan \phi}{a} \right) \right\} dm \\
 &= -\frac{1}{V} \int_V \left\{ \bar{u} \left(-\frac{u}{a \cos \phi} \frac{\partial u}{\partial \lambda} - \frac{v}{a} \frac{\partial u}{\partial \phi} - w \frac{\partial u}{\partial z} + \frac{uv}{a} \tan \phi \right) \right. \\
 &\quad \left. + \bar{v} \left(-\frac{u}{a \cos \phi} \frac{\partial v}{\partial \lambda} - \frac{v}{a} \frac{\partial v}{\partial \phi} - w \frac{\partial v}{\partial z} - \frac{u^2 \tan \phi}{a} \right) \right\} dm \\
 &= -(\bar{E}_2 + \bar{E}_3), \tag{2-83}
 \end{aligned}$$

$$\begin{aligned}
 E'_1 &= \frac{1}{V} \int_V \left\{ u' \left(-\frac{1}{\rho_0 a \cos \phi} \frac{\partial}{\partial \lambda} \int_z^0 \rho g dz \right) + v' \left(-\frac{1}{\rho_0 a} \frac{\partial}{\partial \phi} \int_z^0 \rho g dz \right) \right\} dm \\
 &= \frac{1}{V} \int_V -\frac{\rho g w}{\rho_0} dm. \tag{2-84}
 \end{aligned}$$

2.4.8 Notes

(1) To maintain the no-slip boundary condition at the western and eastern walls, the antisymmetric conditions are imposed on the horizontal velocity in the friction terms. Nevertheless, the symmetric conditions are imposed on the tangential velocity component in the advection terms. Otherwise the mass may not be conserved. This is because the boundary condition on the vertically integrated current (i. e., $\Psi = \text{constant}$ along the lateral walls) guarantees no normal flow, but does not mean no tangential flow.

(2) The boundary conditions on vertical velocity — $w = 0$ at the ocean surface and bottom

— can not be thoroughly satisfied at the same time. Let $w=0$ at the ocean surface, then w at the bottom is calculated from Eq. (2-45) or Eq. (2-59). In the present calculations, vertical velocities at the bottom are less than 10^{-4} of those in the interior. Therefore, the condition at the bottom is satisfied to within truncation error.

2.5 External forcing

The model ocean is driven by wind stress and heat and salinity fluxes through the sea surface. The forcing functions used to obtain a steady state are steady in time and constant in longitude.

The wind stress has no meridional component, $\tau^{\phi}=0$. The zonal component τ^{λ} is taken from the annual mean zonal wind stress for the Pacific Ocean given in Wyrтки and Meyers (1976) for $30^{\circ}\text{S}-30^{\circ}\text{N}$ and Kutsuwada and Sakurai (1982) for $30^{\circ}\text{N}-54^{\circ}\text{N}$ (Fig. 2-5 (a)). The tropical westward stress is minimum at 1°N .

The thermal forcing is given by the approximate formula proposed by Haney (1971). The heat flux through the surface is calculated from

$$Q_{\tau}(\lambda, \phi, t) = Q \{ T_a^*(\phi) - T_1(\lambda, \phi, t) \}, \quad (2-85)$$

where T_a^* is apparent atmospheric equilibrium temperature,

$$T_a^*(\phi) = 13.0 + 17.0 \cos\left(\frac{\phi}{40} \frac{\pi}{2}\right), \quad (2-86)$$

(Fig. 2-5 (b)), T_1 the calculated temperature of the top layer of the model ocean, and Q a coupling coefficient. In this study, Q is taken to be a constant of $50 \text{ cal/cm}^2 \cdot \text{day} \cdot \text{K}$. This value indicates that the temperature of the uppermost layer (60 m) is adjusted to T_a^* on a time scale of about 120 days.

The salinity flux through the surface is calculated from

$$Q_s(\lambda, \phi, t) = S_1(\lambda, \phi, t) \{ E(\phi) - P(\phi) \}, \quad (2-87)$$

where S_1 is the calculated salinity of the top layer, E the evaporation, and P the precipitation. $E(\phi)$ is taken from the zonal mean annual evaporation for the Pacific Ocean estimated by Wyrтки (1965), Weare et al. (1981), and Saiki (private communication, 1981). $P(\phi)$ is taken from the zonal mean annual precipitation for the Pacific Ocean estimated by Dorman and Bourke (1979). The meridional profile of $(P-E)(\phi)$, with addition of some constant value for zero total $(P-E)$, is shown in Fig. 2-5 (c).

2.6 Vertical resolution of the model ocean and initial conditions

The model ocean is divided into eight layers in the vertical, with boundaries at 0, 60, 190, 380, 590, 850, 1450, 2700, and 5000 m. The depth of the levels z_k is given in Table 2-1.

The initial state of the model is a horizontally uniform stratification with no motion. The vertical distributions of temperature and salinity are given in Table 2-1. Except for the upper two levels, they are taken from hydrographic data in the western tropical North

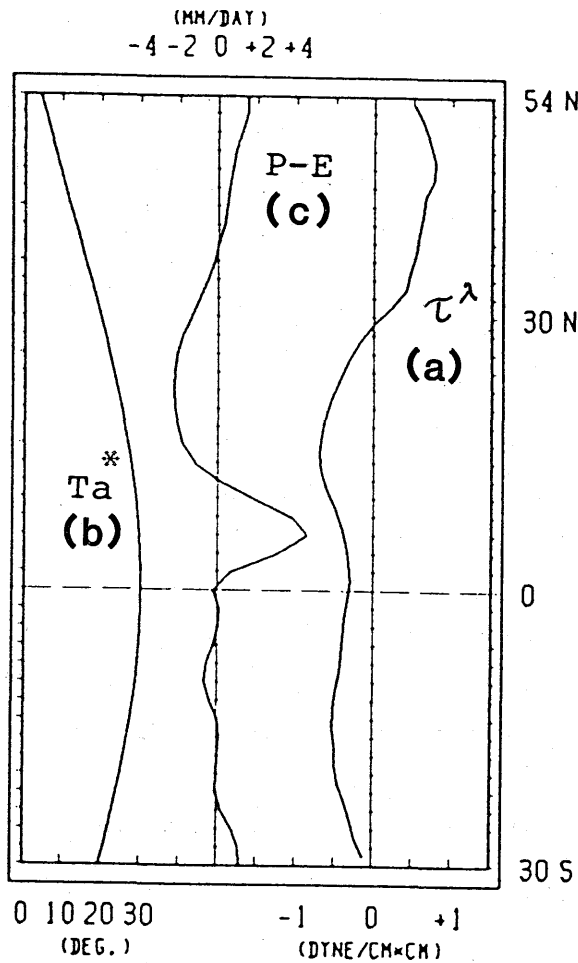


Fig. 2-5 The prescribed external forcing function: (a) the zonal wind stress τ^{λ} , (b) the apparent atmospheric equilibrium temperature Ta^* , and (c) the precipitation minus evaporation ($P-E$).

Pacific. Fig. 2-6 shows the corresponding density profile.

2.7 Computation and parameters

The convergence of the solution to an equilibrium is accelerated by two ways, in addition to the numerical and programming techniques mentioned in the previous sections. One way

Table 2-1 Depth of levels z_k and initial values of temperature and salinity.

No.	Depth (m)	T (°C)	S (‰)
1	20	9.2	34.515
2	100	9.1	34.52
3	280	9.0	34.525
4	480	7.2	34.54
5	700	5.9	34.52
6	1000	4.55	34.545
7	1900	2.35	34.62
8	3500	1.55	34.68

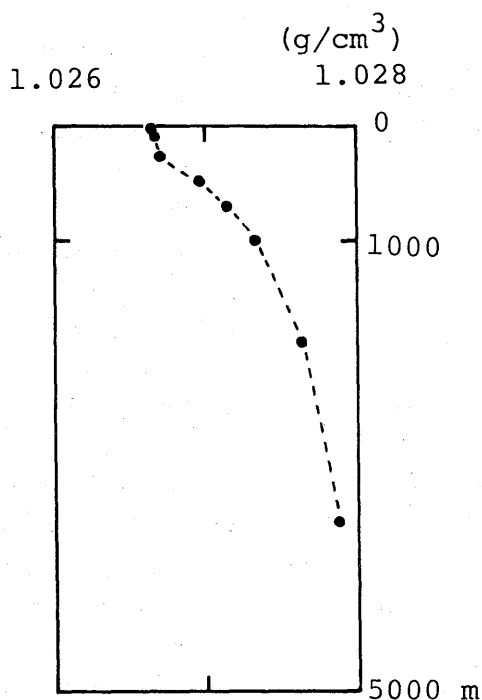


Fig. 2-6 Initial density stratification.

is to separate the integration into two stages, stage I and stage II, where the zonal grid spacing in stage I is twice as large as that in stage II. The other way is to use $\Delta t/a$ ($a > 1$) as the time step for integration of the barotropic vorticity equation. The latter treatment is equivalent to taking a shorter time step for the rapidly adjusting barotropic field than for the baroclinic field. This is justified when all local time derivatives vanish.

The values of all parameters used in the model are given in Table 2-2. The magnitude of A_m is determined so that the frictional width of the western boundary current is marginally resolved by the zonal grid spacing $\Delta \lambda$ (Takano, 1974). For A_h , a much smaller value is chosen than that required for A_m , because the horizontal diffusion and surface flux will nearly balance if the same value is chosen, especially in stage I. But a further decrease of A_h excites a computational mode.

As noted above, external gravity waves are filtered out by employing the rigid-lid assumption, and inertial oscillations are handled by treating the Coriolis terms implicitly. Hence, the maximum time step which can be used in this system is determined approximately

Table 2-2 Values of parameters used in the model.

parameters	stage I	stage II	
a	6375 km		radius of the earth
Ω	$7.292 \times 10^{-5} \text{sec}^{-1}$		rotation rate of the earth
g	980 cm/sec ²		acceleration of gravity
ρ_0	1.025 g/cm ³		reference density of sea water
c_p	($\rho_0 c_p = 1.0 \text{ cal/cm}^3 \cdot \text{K}$)		specific heat of sea water
KM	8		number of levels in vertical
H	5000 m		total ocean depth
JM	45		number of T, S points in latitude
$\Delta \phi$	2.0°		meridional grid separation
IM	23	43	number of T, S points in longitude
$\Delta \lambda$	5.0°	2.5°	zonal grid separation
K_m	1.0 cm ² /sec		vertical eddy viscosity
K_h	1.0 cm ² /sec		vertical eddy conductivity
A_m	$2.0 \times 10^9, 3.0 \times 10^8 \text{ cm}^2/\text{sec}$		horizontal eddy viscosity
A_h	$2.0 \times 10^7 \text{ cm}^2/\text{sec}$		horizontal eddy conductivity
Δt	4.8	4.0 hr	time step
a	10		($\Delta t/a$: time step for the vorticity equation)
Q	50 cal/cm ² ·day·K		coupling coefficient

by the phase speed of internal gravity waves. We set $\alpha=10$. If $\alpha=1$, that is, if the same time step is taken for the vertical mean current as for the vertical shear current, Δt must be reduced to about one hour in order to suppress computational instability.

3. Normal State

3.1 Time integration

As already indicated in section 2.7, the calculation was carried out in two stages. The integration of stage I, in which $\Delta\lambda=5.0^\circ$, was made over a period of 100 years, starting from the initial state given in section 2.6. Then, instantaneous fields at the end of stage I were interpolated linearly to the grids of stage II, in which $\Delta\lambda=2.5^\circ$, and the stage II was calculated for another 40 years.

Fig. 3-1(a) shows the time history of the overall mean kinetic energies. The total kinetic energy reaches its maximum value at the beginning of each stage, the 220th day of stage I and the 60th day of stage II. Then, it begins to decrease until the 6th year of stage I and the 220th day of stage II. For the rest of each stage, the total kinetic energy

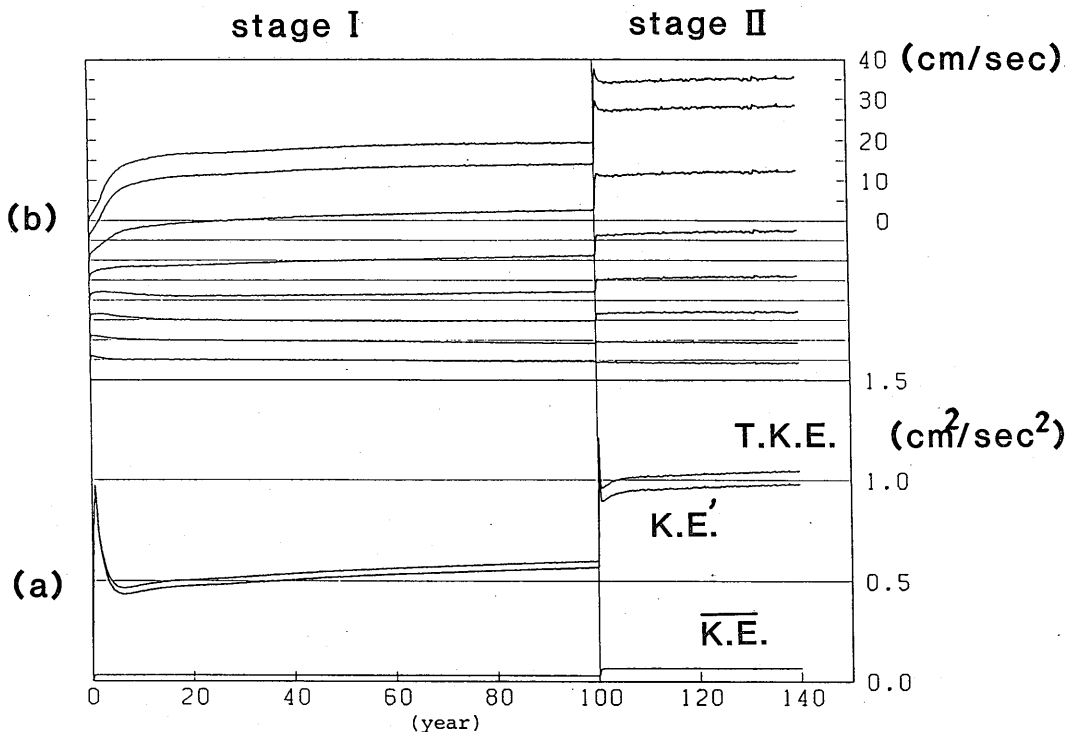


Fig. 3-1 (a) Time history of the overall mean kinetic energies per unit mass. $\overline{K.E.}$, $K.E'$, and $T.K.E.$ mean the kinetic energies of the vertical mean current, vertical shear current, and total current, respectively.

(b) Time development of the western boundary current at $(33^\circ\text{N}, 2.5^\circ\text{E})$ during stage I and at $(33^\circ\text{N}, 1.25^\circ\text{E})$ during stage II. The curves correspond to the northward velocities at level 1 (top) through level 8 (bottom).

continues to increase very slowly. Almost 95% of the kinetic energy is contributed by the vertical shear current. The kinetic energy of the vertical mean current is almost constant except for the first 100 days of each stage. (It should be remembered that the rate of change of the vertical mean current was reduced to one tenth in the present model.) The available potential energy (not shown here) increases from zero at the initial time to $415(\text{cm}/\text{sec})^2$ at the end of the 140th year. The northward component of the western boundary current is shown as a function of time in Fig. 3-1(b). The current continues to speed up in the upper ocean except for a short term at the beginning of stage II.

The thermal response is rapid near the surface, and the temperature averaged over level 1 is almost constant during the last 60 years. On the other hand, the mean temperatures of levels 5 and 6 increase at the rate of $0.01\sim 0.02^\circ\text{C}/\text{year}$ in stage II. This reflects that the thermocline given as an initial state diffuses with time. The overall mean temperature continues to increase slowly throughout the computation. An inspection of the time development of the temperature and salinity patterns in a meridional plane along the central longitude shows that their main features are developed during the first 50 years.

In this chapter the final state of stage II, which is defined as the normal state in the subsequent studies, is described briefly. Overall characteristics are similar to the numerical solutions of Bryan and Cox (1968), Haney (1974), and Takano (1981).

3.2 Horizontal distributions

Fig. 3-2 shows the stream function of the vertically integrated transport. Five circulation gyres are developed in the model ocean. The general characteristics of the pattern, such as the latitudinal extent, relative strength, and rotating direction of each gyre, are basically identical to those predicted by the Stommel-Munk theory of a wind-driven ocean. But there are some discrepancies. The maximum poleward transport, for example, by the anticyclonic subtropical gyre in the northern ocean occurs at 28°N , while the wind stress curl is maximum at 30°N . The maximum transport of $44.8 \times 10^{12} \text{ cm}^3/\text{sec}$ is smaller by about 20% than that computed according to the Sverdrup relation, 55.4×10^{12} . These discrepancies are mainly caused by the smoothing effect of the large eddy viscosity used in the model. In fact, the transport given by the Sverdrup relation is 29.8×10^{12} at 26°N , 36.2×10^{12} at 28°N , 38.4×10^{12} at 32°N , and 12.8×10^{12} at 34°N (cf. Fig. 3-13, which shows a result for a weakly viscous model).

The fields of temperature, salinity, density, and horizontal velocity at level 1 are shown

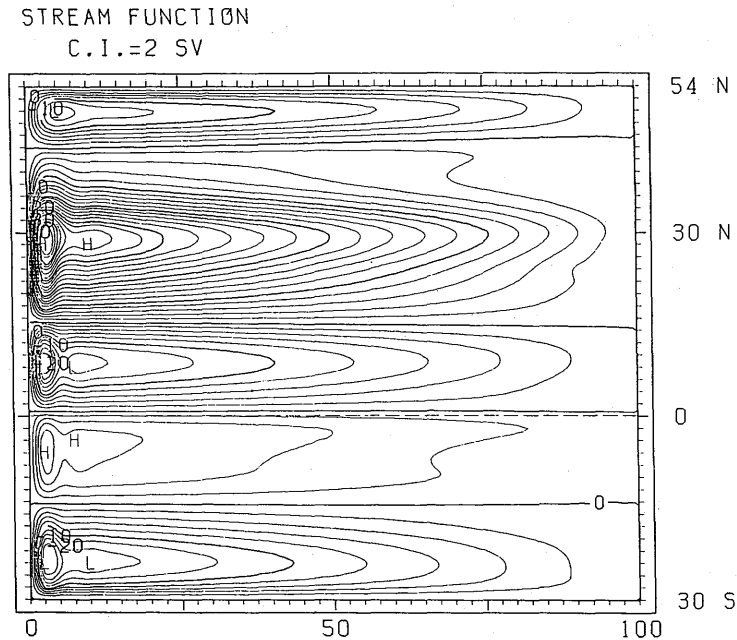


Fig. 3-2 Stream function of the vertically integrated transport. The contour interval is given at the top left. Thick lines are drawn every five intervals. $1 \text{ SV} = 10^6 \text{ m}^3/\text{sec}$.

in Figs. 3-3(a) through (d). Although the general patterns of isotherms and isohalines are zonal and are principally governed by the external parameters T_a^* and $(P-E)$, several features dynamically produced are clearly seen. In particular, a cold water band is developed along the equator where T_a^* is maximum. This is a result of the strong divergence of the wind-driven Ekman currents, which builds up a narrow band of strong upwelling (w is 5×10^{-3} cm/sec at the bottom of the uppermost layer) along the equator. In addition, there is a warm tongue extending northward along the western boundary in the north subtropical latitudes. This feature is due to the horizontal temperature advection in the anticyclonic gyre. The model analog of the subtropical front can be seen in the temperature field between 25°N and 30°N , which shifts northward in the eastern part of the ocean (Takeuchi, 1984).

The density distribution is primarily determined by the temperature. The salinity acts to strengthen the density front around 20°N , and to weaken it north of about 25°N .

The current vectors clearly show the model analogs of the Kuroshio, the North Pacific Current, and the Subtropical Counter Current. The western boundary current attains a

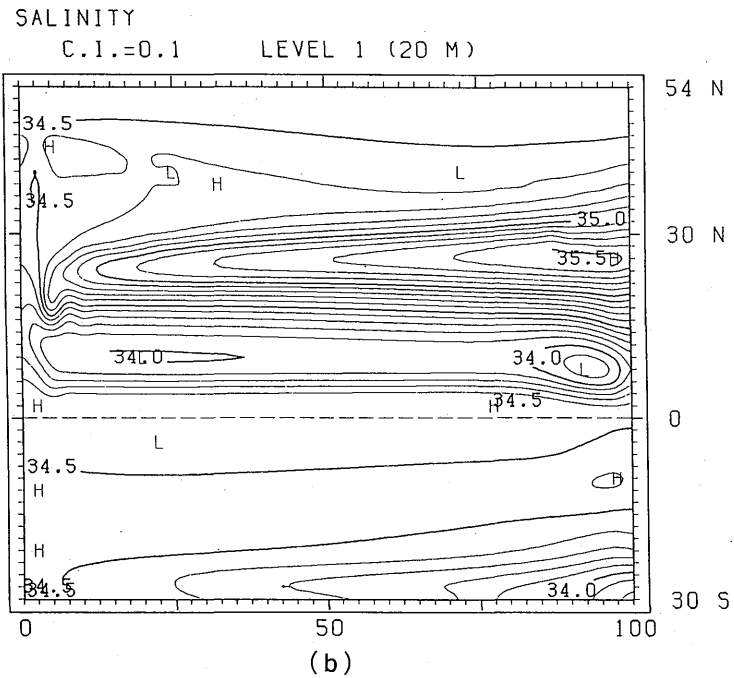
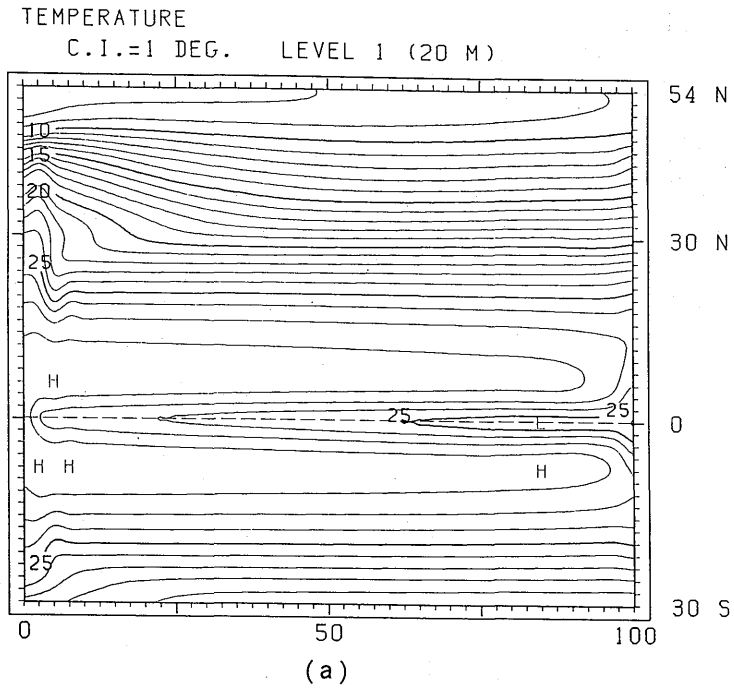
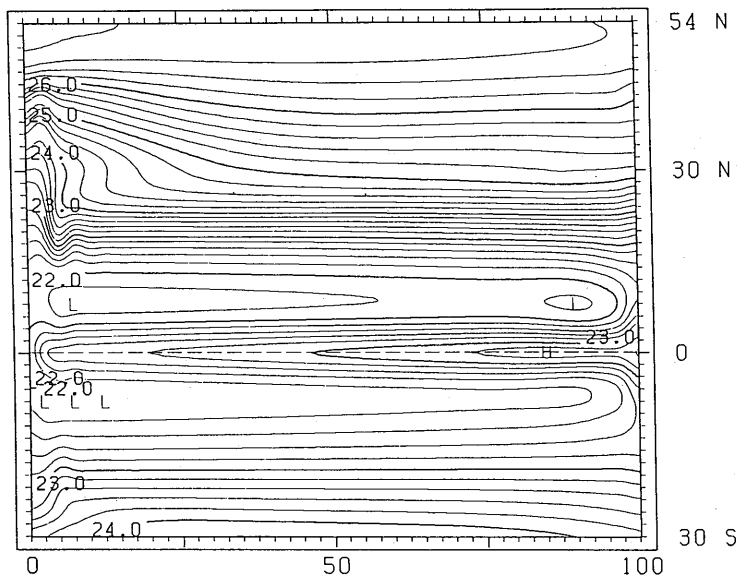


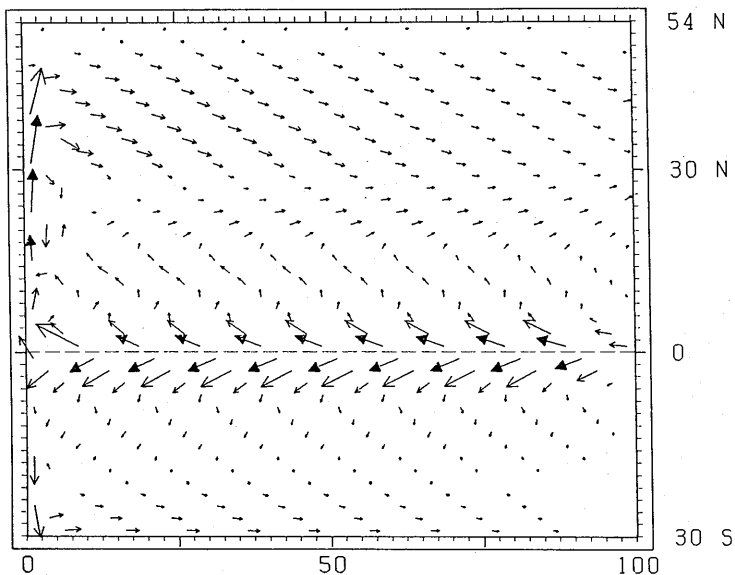
Fig. 3-3 (a) Temperature, (b) salinity, (c) density, and (d) horizontal velocity vectors at level 1. Velocity vectors are plotted only at every 10° of longitude. The arrows are scaled by the vectors given at the top left.

DENSITY IN SIGMA T
C.I.=0.2 LEVEL 1 (20 M)



(c)

HORIZONTAL VELOCITY
→ : 10 → : 20 CM/S LEVEL 1 (20 M)



(d)

Fig. 3-3 Continued.

maximum speed of 40 cm/sec at 31°N. The model analogs of the North Equatorial Counter Current and the North Equatorial Current, on the other hand, are very weak. In the tropical latitudes the currents have a discernible poleward component, of which the dominant part is the Ekman current driven by the easterly wind stress. As a result the zonality of currents in the tropics is very poorly reproduced. The analogs of the California Current and westward subarctic currents are completely missing at level 1.

Figs. 3-4(a) and (b) show the temperature and velocity fields at level 2. The cold water along the equator is much less extensive than at level 1, and a warm water pool is developed in the western part of the tropics. The flow pattern near the equator is a reversal of that at level 1. The model analog of the Equatorial Undercurrent is produced, though it has a considerable equatorward component. (It should be noted that velocity vectors are plotted at every fourth grid in the longitudinal direction.) The subsurface extension of the model's North Equatorial Counter Current at 7°N is merged with the equatorial undercurrent. The subtropical gyre of the northern ocean is clearly seen at level 2 since the model's North Equatorial Current is stronger than at level 1. But the eastward transport in the gyre is much larger than the westward transport. A large part of the eastward flowing mass bumps against the eastern boundary and sinks to deeper layers there. Weak westward currents are seen along the northern boundary. The model's Equatorial Undercurrent is almost zonal at level 3 (not shown here).

Figs. 3-5(a) and (b) show the temperature and velocity fields at level 4. The temperature is relatively low in the tropical region, and warm water pools are developed in the subtropics. In the equatorial region, noted are the eastward currents symmetrically located about the equator. In the eastern half of the equator, they are separated by westward currents centered on the equator. The eastward currents are the model analog of the Equatorial Subsurface Counter Currents. The most unrealistic feature of level 4 is a warm tongue extending west-southwestward from the eastern boundary near 30°N. The warm water is supplied by strong downwellings in the vicinity of the eastern boundary, and it is advected along the southern flank of the subtropical gyre. (The realistic temperature pattern is a westward intensified pool of warm water, like that produced in the southern ocean.) The same unrealistic feature is also seen at level 3, where a warm tongue is generated around 25°N.

The fields at the lower four levels are not shown here. The warm tongue extending from the eastern boundary is also seen at level 5 and level 6 around 38°N and 44°N, re-

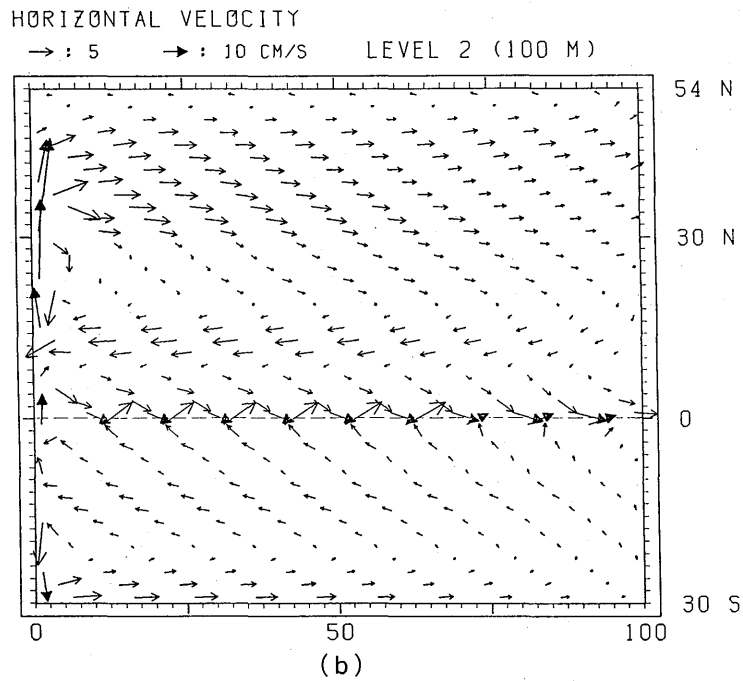
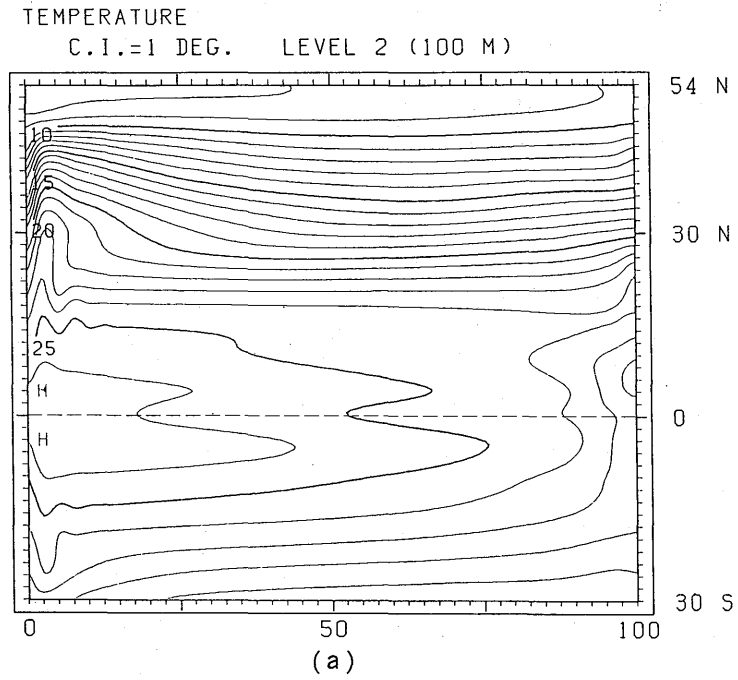
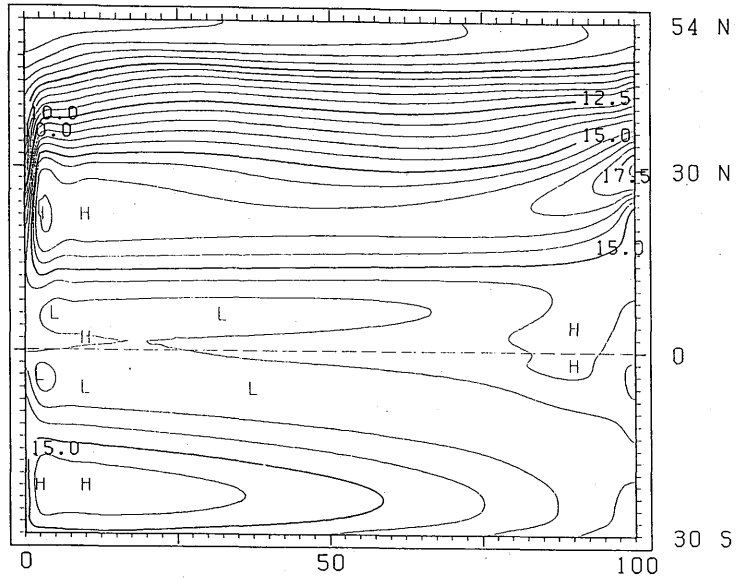


Fig. 3-4 (a) Temperature and (b) horizontal velocity vectors at level 2.

TEMPERATURE

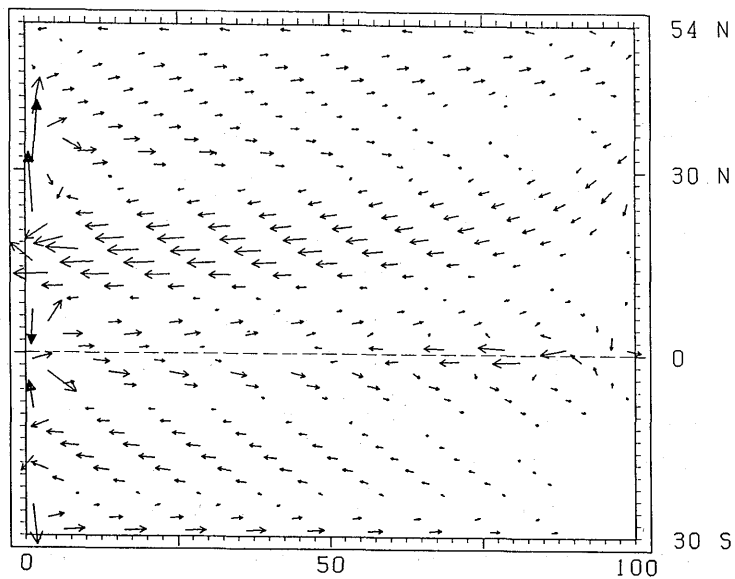
C.I.=0.5 DEG. LEVEL 4 (480 M)



(a)

HORIZONTAL VELOCITY

→ : 3 → : 6 CM/S LEVEL 4 (480 M)



(b)

Fig. 3-5 As in Fig. 3-4 except for level 4.

spectively. At level 7 warm temperatures are produced in the vicinity of the northern boundary.

3.3 Vertical sections

The three-dimensional structure of physical property is almost uniform in the zonal direction except near the western and eastern boundaries. Figs. 3-6(a), (b), and (c) show the distribution of temperature, salinity, and density in a cross-section along the central longitude. (Note that in the following vertical sections, the uppermost one kilometer of the ocean is shown in an expanded scale.) The temperature section shows a tendency for the thermocline to be shallow in the equatorial region. Near 8°N the thermocline bifurcates into an upper and a lower portion. The upper one gradually shallows poleward and surfaces at about 25°N. It is associated with the model's Subtropical Counter Current. The lower one, which slopes down toward the north, is associated with the westward flowing branch of the subtropical gyre. The water below 1 km has no outcrop at the surface, since the convective overturning adjacent to the northern boundary penetrates only to 1 km. (In the vicinity of the eastern boundary the convective overturning penetrates down to about 2 km. See Fig. 3-8 (a).)

In the salinity section, relatively high or low salinity water is extended downward from the sea surface with the latitude where the imposed ($P-E$) takes a minimum or maximum value.

The salinity-minimum layer at an intermediate depth extending southward from the subarctic, which is one of the most salient features observed in the North Pacific, is not reproduced. The density field is quite similar to that of temperature.

Fig. 3-6(d) shows a cross-section of the eastward velocity component. The vertical profile is complicated at the equator where eastward and westward currents alternate between level 5 and level 8. The eastward velocity corresponding to the model's North Equatorial Counter Current is only slightly discerned and merges with the model's Equatorial Undercurrent as described above.

In the northern extratropics there are three maxima of eastward current speed. One at 23°N corresponds to the model's Subtropical Counter Current. The other two are caused by the latitudinal profile of the imposed wind stress curl (cf. Fig. 3-12).

The temperature section along the equator is shown in Fig. 3-7. The model reproduces two interesting features which are also seen in the observed temperature sections (Moore and

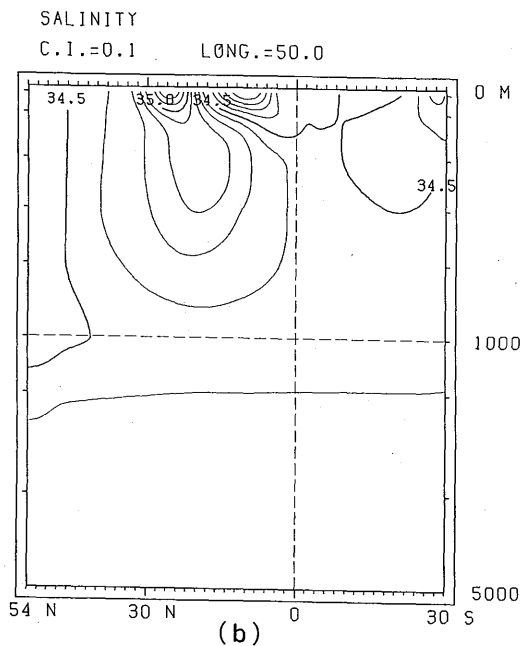
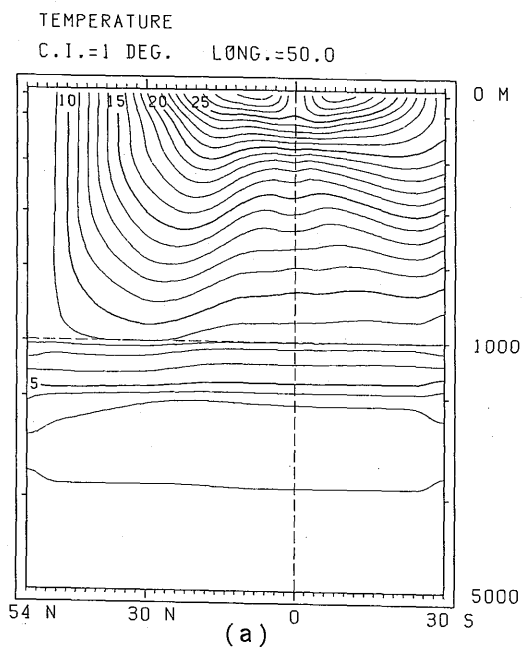


Fig. 3-6 Vertical sections of (a) the temperature, (b) salinity, (c) density, and (d) zonal velocity component. (a), (b), and (c) are along 50°E, and (d) is along 51.25°E. Westward motion is shaded. The vertical scale is exaggerated in the upper one kilometer.

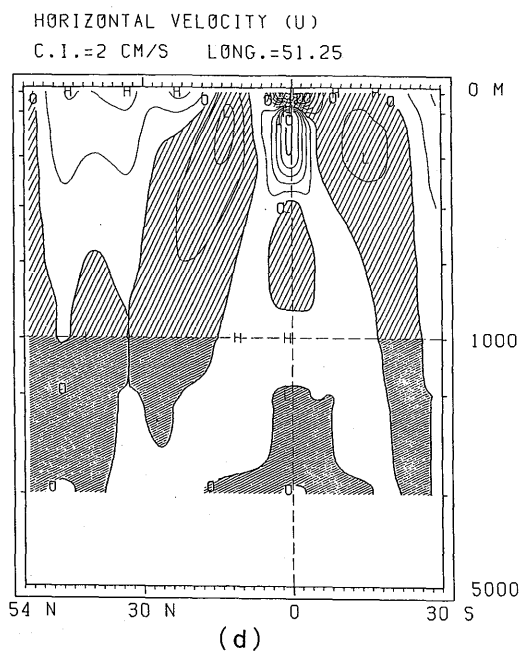
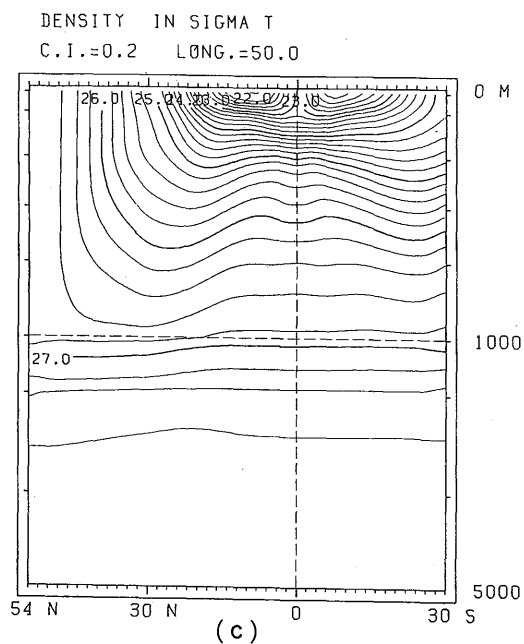


Fig. 3-6 Continued.

TEMPERATURE

C.I.=1 DEG. LAT.=0

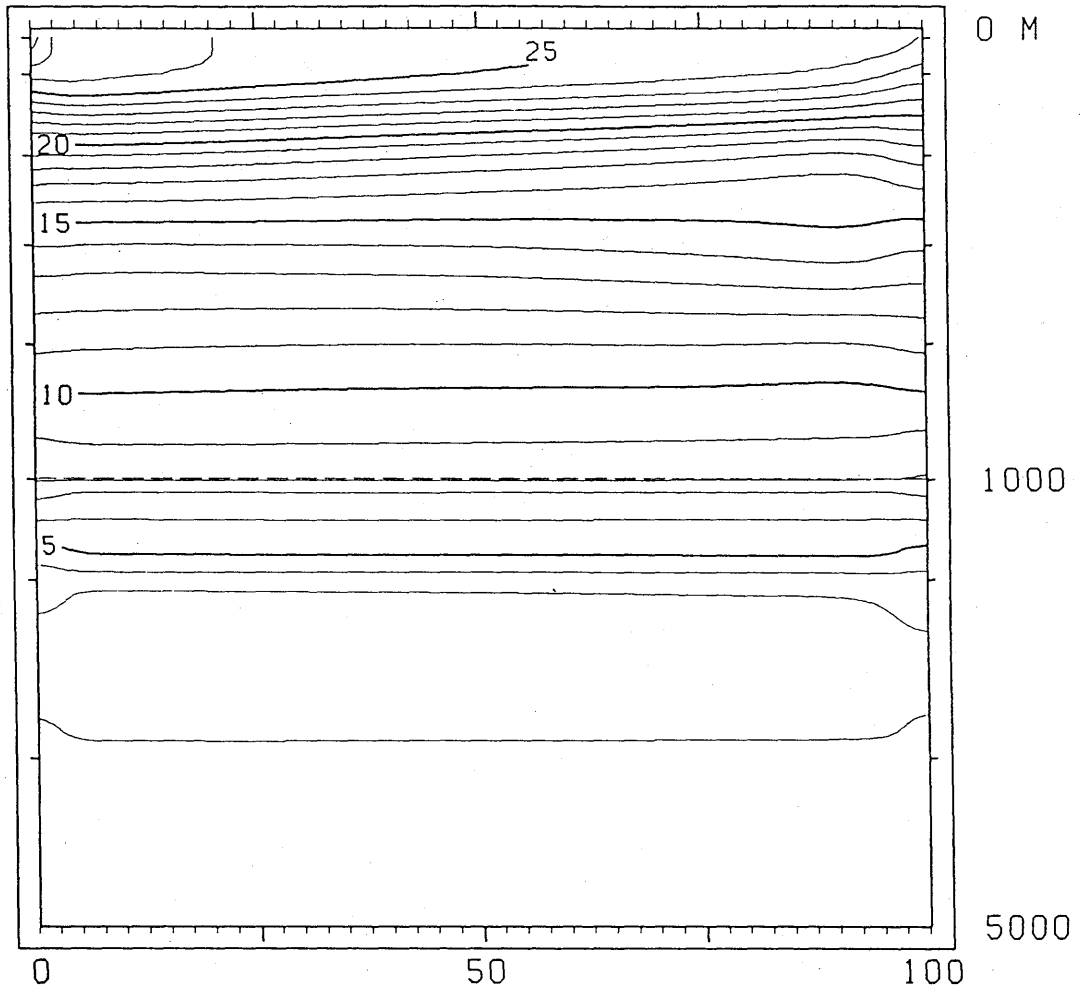


Fig. 3-7 A vertical section of the temperature along the equator.

Philander, 1977). The first is the thermocline which slopes upward to the east. The second is a relatively homogeneous layer near 400 m in the eastern equatorial region. (The model's Equatorial Subsurface Counter Currents described in the preceding section are located at the poleward ends of this thermostat.) The degree of similarity, however, is not satisfactory. The thermocline in the observed sections is sharper and shallower in the eastern region. Furthermore, the thermostat is located at a shallower depth of 200–300 m. It is also noted that the model does not produce the correct zonal gradient of surface temperature. In

observations, the zonal temperature gradient is large in the eastern region and relatively isothermal warm water is located in the western region. In the model, on the other hand, the gradient is relatively large near the western boundary (see Fig. 3-3(a)). This discrepancy can be partly attributed to the zonal structure of the wind stress. A zonally uniform stress is imposed in the model, while several analyses of the tropical wind field (Wyrtki and Meyers, 1976) indicate that the annual mean wind stress significantly varies in the zonal direction and the westward wind is strongest in the central Pacific Ocean.

Now the vertical thermal structure associated with the warm tongue seen in the southern flank of the northern subtropical gyre is described. Fig. 3-8(a) shows the vertical temperature section along the eastern boundary. It indicates that, north of 20°N, surface warm water penetrates to a greater depth with latitude. The zonal temperature section along 30°N, which cuts through the center of the subtropical gyre, is shown in Fig. 3-8(b). The isotherm pattern is not realistic in the eastern part where strong downwelling takes place. In observed sections, isotherms generally slope upward to the east except in the western boundary current region.

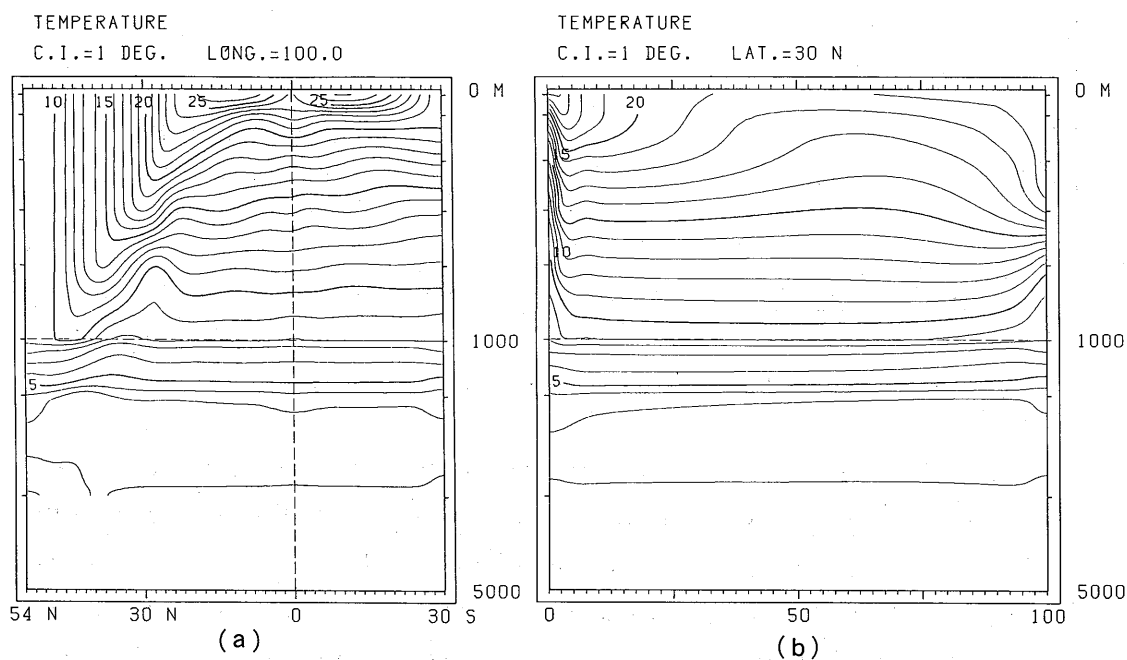


Fig. 3-8 Vertical sections of the temperature along (a) the eastern boundary (100°E) and (b) 30°N.

3.4 Meridional circulation and meridional heat transport

Integrating the continuity equation (2-5) from the western to the eastern boundary, the following equation is obtained:

$$\int_0^{100\pi/180} \cos\phi \frac{\partial w}{\partial z} d\lambda + \int_0^{100\pi/180} \frac{\partial}{\partial \phi} (v \cos\phi) d\lambda = 0. \quad (3-1)$$

From this relationship the meridional circulation integrated over the zonal extent of the ocean basin can be specified in terms of a transport stream function Φ , such that

$$\int_0^{100\pi/180} a \cos\phi \cdot w d\lambda = \frac{\partial \Phi}{\partial \phi},$$

$$\int_0^{100\pi/180} a \cos\phi \cdot v d\lambda = -\frac{\partial \Phi}{\partial z}. \quad (3-2)$$

The streamfunction is shown in Fig. 3-9. A direct meridional cell of basin-wide scale dominates in the northern ocean. The general sinking motion, which primarily occurs near the eastern boundary, extends deep to the north. This thermohaline circulation is confined to the upper 2 km, and the abyssal part of the basin is isolated. The isolated water, whose temperature and salinity gradually change from each initial value mainly due to vertical diffusion, is heavier than the dense water formed by the model cooling. The shallow cells in the equatorial region are primarily wind-driven.

Fig. 3-10 shows the heat flux through the ocean surface. Major heating occurs in the equatorial region, and major cooling occurs in the western boundary region of the northern subtropics and in the northern boundary region. Weak cooling and heating occur in the northern interior region between 13°N and 25°N and between 25°N and 40°N, respectively. In an equilibrium state, the heat absorbed in the tropics must be transported poleward to compensate the upward heat flux in the higher latitudes. The total meridional heat transport is given by

$$H = \rho_0 c_p \int_{-H}^0 \int_0^{100\pi/180} (vT - A_h \frac{\partial T}{\partial \phi}) a \cos\phi d\lambda dz$$

$$= \rho_0 c_p \int_{-H}^0 \int_0^{100\pi/180} (\bar{v}\bar{T} + \overline{v'T'}) - A_h \frac{\partial \bar{T}}{\partial \phi}) a \cos\phi d\lambda dz, \quad (3-3)$$

where the overbars indicate the zonal averages, and the primes the deviations from them. The first term represents the heat transport associated with the mean meridional circulation shown in Fig. 3-9. The second term is the effect of correlations between deviations from zonal averages, and represents the heat transport associated with horizontal gyres. The last

term represents the contribution of the northward diffusion of heat. The total heat transport and three components are shown in Fig. 3-11. The heat transport associated with the mean meridional circulation dominates except in the vicinity of the northern and southern boundaries where the effect of horizontal diffusion becomes significant. The total transport has a maximum value of $9 \times 10^{14} \text{W}$ at 15°N .

3.5 Comments

We describe here two aspects of the general circulation which the model fails to reproduce.

The first is on the North Equatorial Counter Current. The second is on the southward

MERIDIONAL CIRCULATION

C.I. = 2 SV

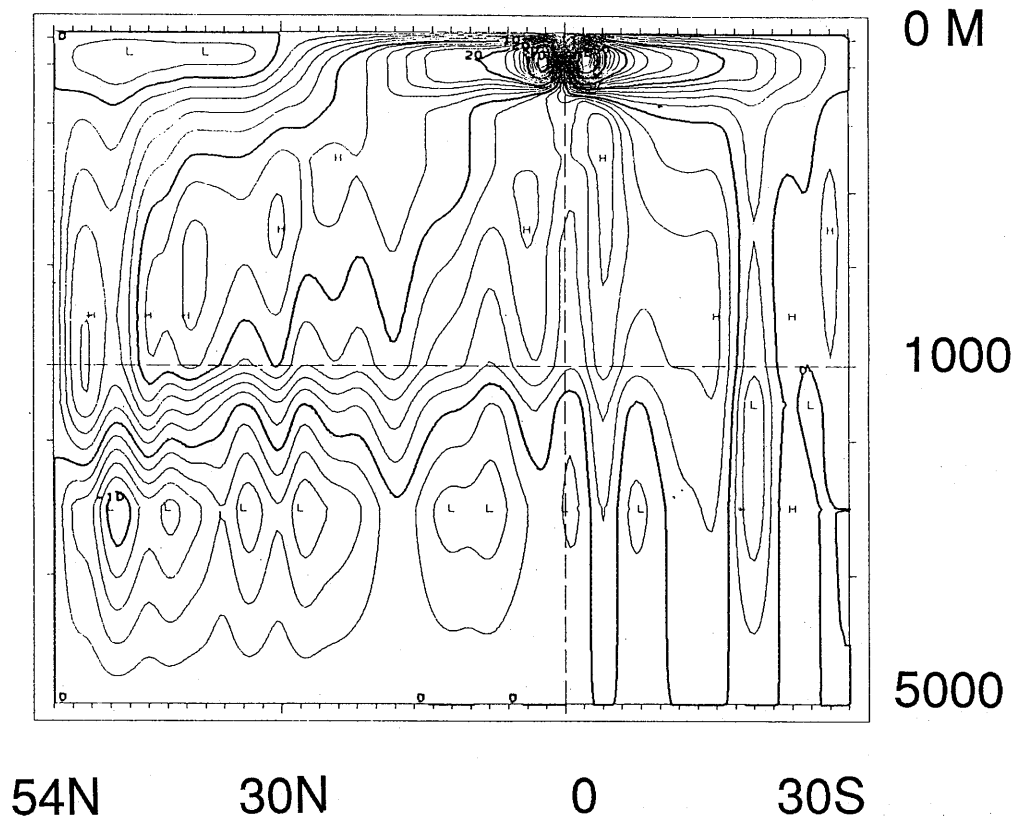


Fig. 3-9 Total transport in the meridional plane.

HEAT FLUX

C.I. = 10 W/M**2

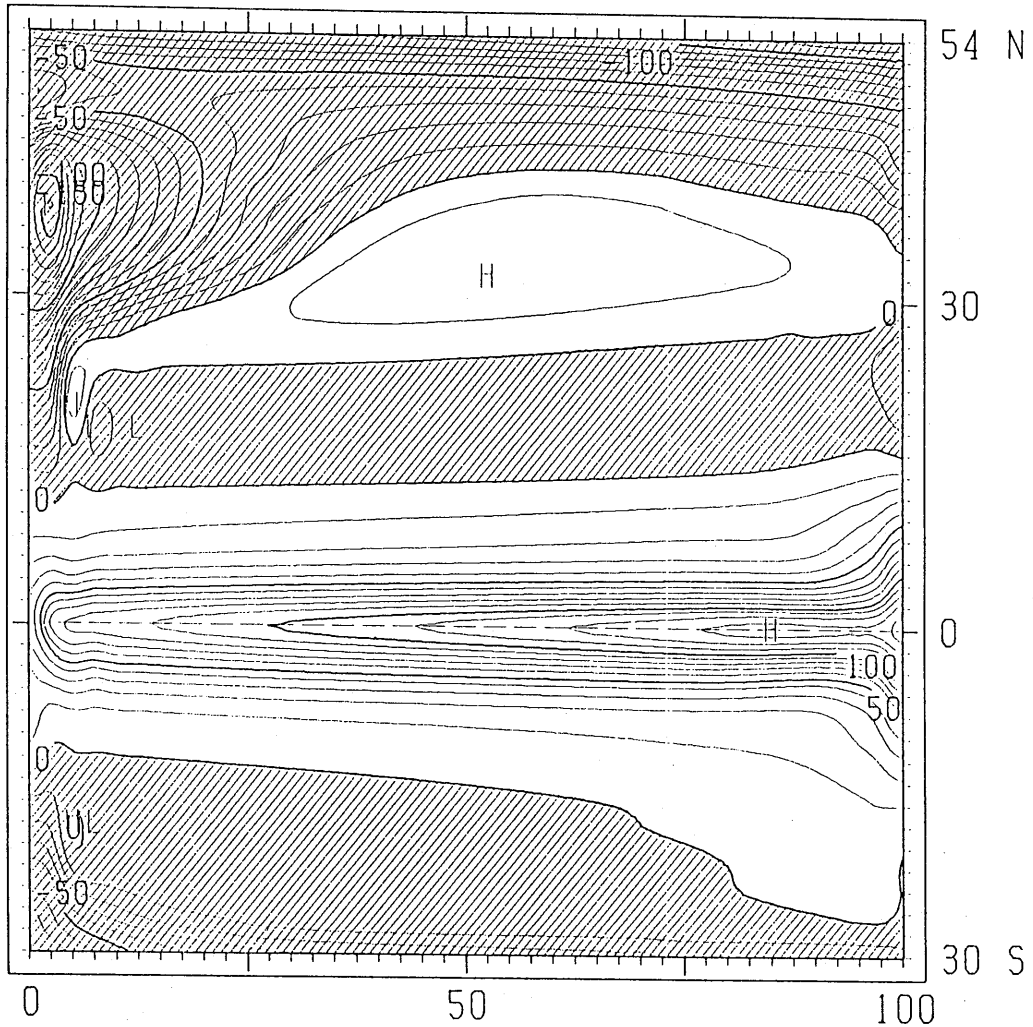


Fig. 3-10 Downward heat flux through the ocean surface.

currents in the eastern part of the northern subtropical gyre and the associated density structure. They are both one of the salient elements in the observed upper ocean structure.

Although these defects do not cause any significant errors in the response studies given in the next chapter, they would give quantitatively inaccurate results.

(1) In the tropics, currents are generally zonal and narrow in the north-south direction. It is supposed, therefore, that the lateral viscosity coefficient used in the model is too large

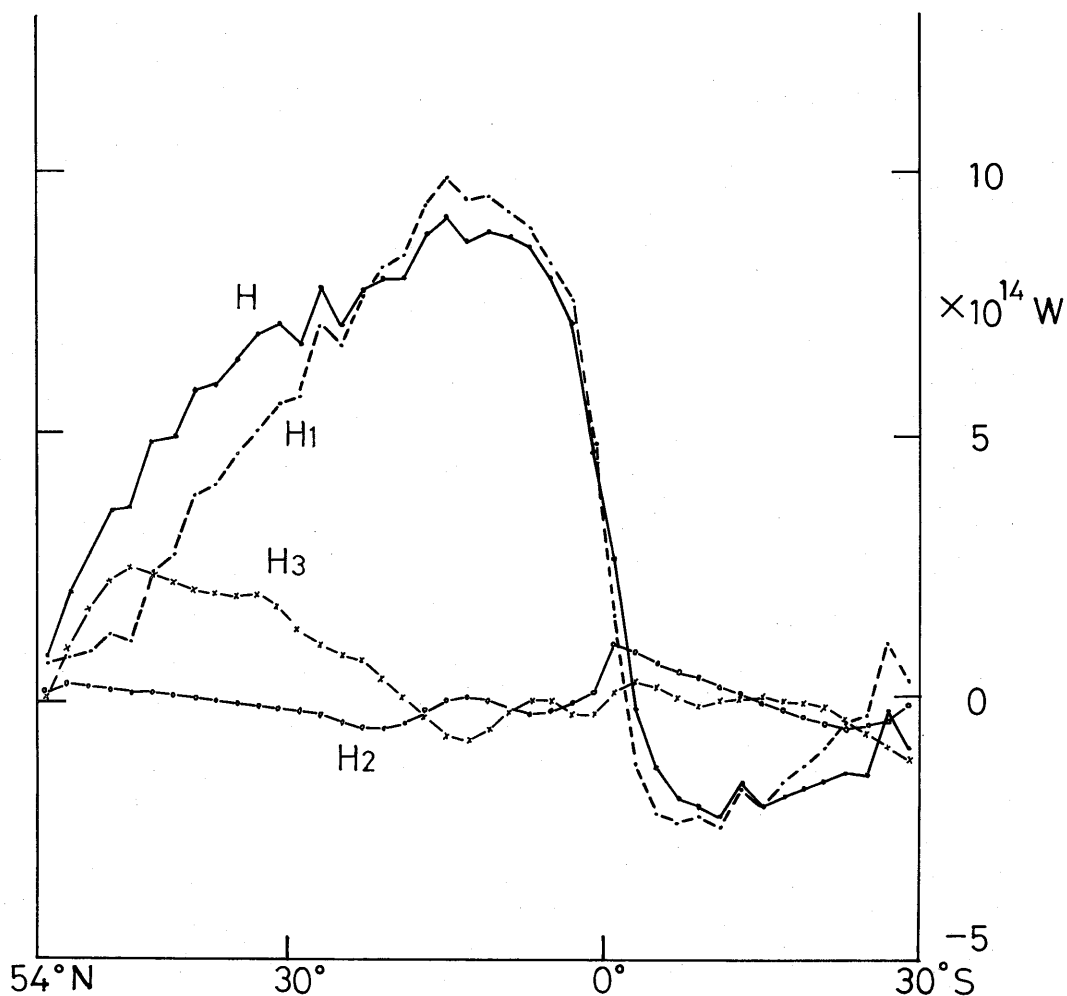


Fig. 3-11 Northward heat transport. H_1 , H_2 , H_3 , and H indicate the contributions of the mean meridional circulation, horizontal gyres, horizontal diffusion, and their sum, respectively.

to resolve the equatorial current pattern. From this viewpoint, a weakly viscous model, in which $A_m = 3.5 \times 10^7$ cm²/sec and $\Delta \lambda = 1.25^\circ$, was integrated over a period of 10 years, starting from the initial state of rest given in section 2.6. In this model, the salinity was held constant, i.e., $S = 34.5$, because salinity has only a minor effect on the density structure in the low latitudes.

Fig. 3-12 shows a meridional section of the eastward velocity component at the end of the 10th year. The model's North Equatorial Counter Current is clearly produced, with a core at the surface. It thus appears that the meridional grid distance of 2° would marginally

HORIZONTAL VELOCITY (U)

C.I. = 2 CM/S LONG. = 50.625

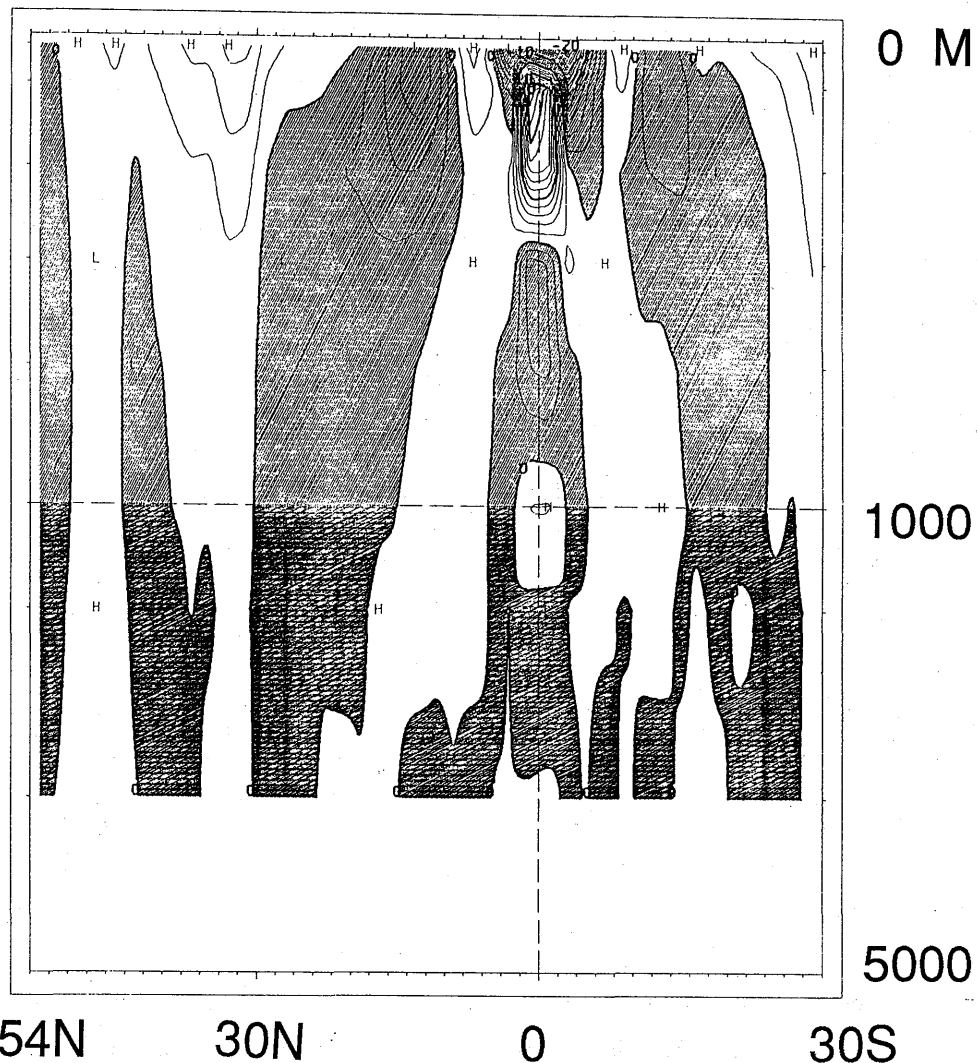


Fig. 3-12 As in Fig. 3-6 (d) except for the weakly viscous model and along 50.625°E.

resolve the equatorial current pattern if the viscosity coefficient is small enough. In the figure, an eastward cell, which is a south equatorial counter current, is also seen at 9°S. This is attributed to the imposed wind stress curl, having maxima at 2°S and 10°S. Fig. 3-13 shows the stream function of the vertically integrated transport. The southern tropical gyre and the northern subtropical gyre have both split into two gyres as a result of the reduction

STREAM FUNCTION

C.I. = 2 SV

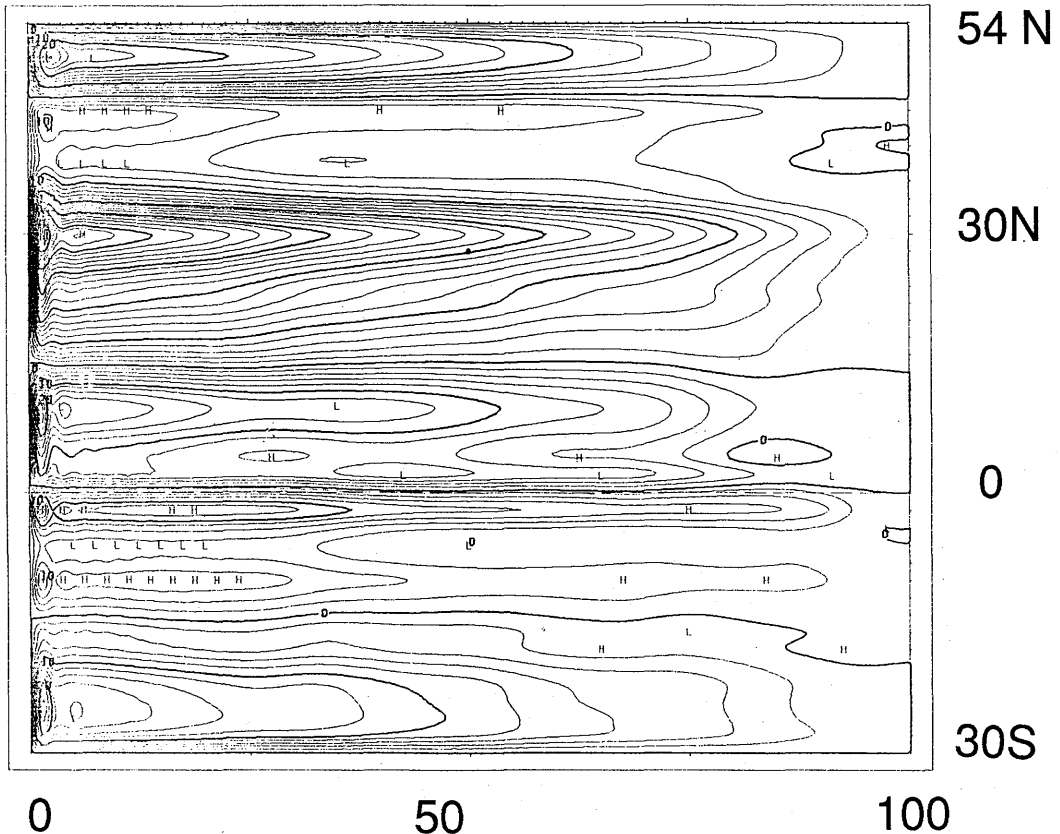


Fig. 3-13 As in Fig. 3-2 except for the weakly viscous model.

of viscosity (cf. Fig. 3-2). The split patterns reflect the curl τ pattern.

(2) In the eastern subtropics, the same feature, that is, a warm tongue extending westward from the eastern boundary, appears more or less in the results as previously reported, for example, by Haney (1974) and Takano (1981). (It is also seen in the result of an eddy resolving model by Han (1975), in which the calculation was started from the quasi-steady state obtained with a coarse grid model.)

This feature is due to the heat-driven circulation, as shown in Takano (1981). The upper boundary condition on temperature forces the temperature of the upper ocean to take a southward gradient in the eastern subtropics where horizontal currents are weak. Therefore, a baroclinic current normal to the boundary is developed near the eastern

boundary, where the vertical mean current has no normal component. (The warm tongue feature apparently does not appear in Semtner and Mintz (1977). The gradient of the apparent air temperature is not parallel to the eastern boundary in their model, but it is not clear how this condition affects the dynamics near the eastern boundary.)

4. Response Studies

4.1 Introduction

In this chapter, numerical experiments are presented which examine the generation and evolution of large-scale oceanic anomalies in response to anomalous wind forcing, on time scales of a month to a few years. Anomalous winds corresponding to a relaxation of the easterly winds in the equatorial region (section 4.2) and an intensification of the trade winds in the tropical and subtropical region (section 4.3) are imposed for several months. These wind anomalies are known as one of the atmospheric phenomena involved in ENSO (e. g., Rasmusson and Carpenter, 1982). Also is presented an additional experiment which demonstrates the evolution of an existing temperature anomaly under no anomalous wind forcing.

The experiments are summarized in Table 4-1-1. The corresponding anomalous winds and initial temperature anomaly are also shown in Fig. 4-1-1. Case 101 and case 201, whose normals are horizontally uniform and motionless, are the counterparts of case 100 and case 200.

Before anomaly experiments are carried out, the model is integrated over two years, starting from the state at the 140th year described in Chapter 3. During this integration and the following anomaly experiments, the heat and salinity fluxes through the ocean surface are kept to be the same as those at the end of the 140th year. This condition is chosen simply in order to isolate the effects of anomalous wind forcing and the ocean's internal adjustment mechanisms on anomaly development. The heat flux calculated according to Eq. (2-85) has a tendency to damp the temperature anomalies. The effects of anomalies in the surface heat and salinity fluxes on the generation and evolution of oceanic anomalies are not studied here.

The following description refers mainly to the temperature anomalies. *The anomaly of a variable is defined as the deviation from its normal which is obtained by the integration for the same period under no anomalous forcing.* Since the normal run is almost steady except in the deeper layers, the state is similar to that described in Chapter 3. The definition is employed because the temperature of the deeper layers changes slightly due to the vertical diffusion even in the absence of anomalous forcing. The prediction equation for a temperature anomaly can be written as

$$\frac{\partial T'}{\partial t} = -u' \frac{\partial \bar{T}}{a \cos \phi \partial \lambda} - v' \frac{\partial \bar{T}}{a \partial \phi} - \bar{u} \frac{\partial T'}{a \cos \phi \partial \lambda} - \bar{v} \frac{\partial T'}{a \partial \phi} - w' \frac{\partial \bar{T}}{\partial z} - \bar{w} \frac{\partial T'}{\partial z} - u' \frac{\partial T'}{a \cos \phi \partial \lambda}$$

(A) (B) (C) (D) (E) (F) (G)

Table 4-1-1 Description of the experiments, (a) response to anomalous wind forcing and (b) evolution of an initial temperature anomaly. τ^λ indicates the normal wind stress. Period means the term for which anomalous winds are imposed. The normal state (*) is almost identical to the quasi-steady state described in Chapter 3, while that (**) for case 101 and case 201 is horizontally uniform and motionless.

(a)

case	anomalous wind stress	period (days)	normal state
100	$0.35 \cdot \sin\left(\frac{\lambda-1.25}{65}\pi\right) \cdot \frac{1}{2}\{1+\cos\left(\frac{\phi}{10}\pi\right)\}$	90	*
101	$1.25 \leq \lambda \leq 66.25$ $-9 \leq \phi \leq 9$	90	**
110	$ \tau^\lambda(\phi) $ $1.25 \leq \lambda \leq 28.75$ $-9 \leq \phi \leq 9$	90	*
120	$ \tau^\lambda(\phi) $ $36.25 \leq \lambda \leq 63.75$ $-9 \leq \phi \leq 9$	90	*
130	$ \tau^\lambda(\phi) $ $71.25 \leq \lambda \leq 98.75$ $-9 \leq \phi \leq 9$	90	*
200	$-0.35 \cdot \sin\left(\frac{\lambda-33.75}{65}\pi\right) \cdot \frac{1}{2}\{1+\cos\left(\frac{\phi-15}{15}\pi\right)\}$	180	*
201	$33.75 \leq \lambda \leq 98.75$ $1 \leq \phi \leq 29$	180	**
210	$- \tau^\lambda(\phi) $ $51.25 \leq \lambda \leq 98.75$ $11 \leq \phi \leq 29$	90	*

(b)

case	initial temperature anomaly	normal state
250	$3 \cdot \cos\left(\frac{\lambda-50}{25}\pi\right) \cdot \cos\left(\frac{\phi-14}{12}\pi\right)$ $37.5 \leq \lambda \leq 62.5$ $8 \leq \phi \leq 20$ $-380 \leq z \leq 0$	*

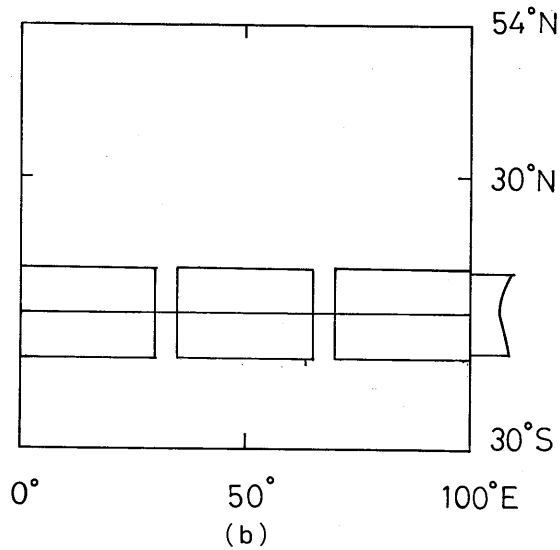
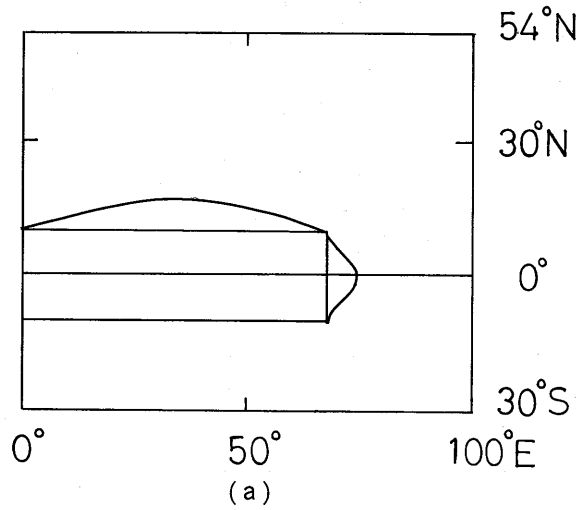


Fig. 4-1-1 Location and structure of the anomalous zonal wind stress, (a) case 100 and case 101, (b) case 110, case 120, and case 130, (c) case 200 and case 201, (d) case 210 and (e) location and structure of the initial temperature anomaly of case 250. The zonal and meridional structures, unless they are zonally uniform, are shown along the longitude and latitude through the centers of the anomalously forced regions. The initial anomaly of case 250 uniformly extends from the surface to 380 m depth.

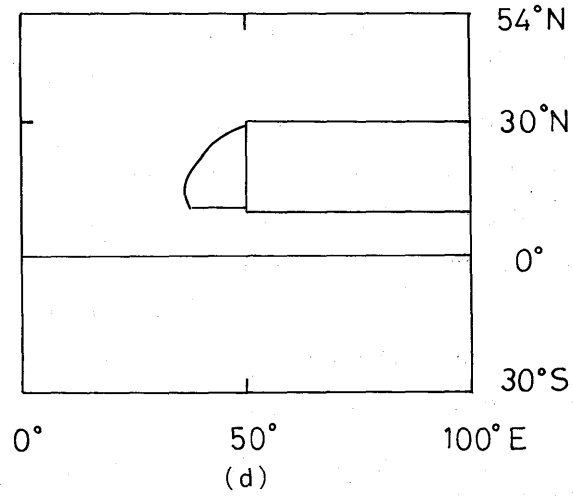
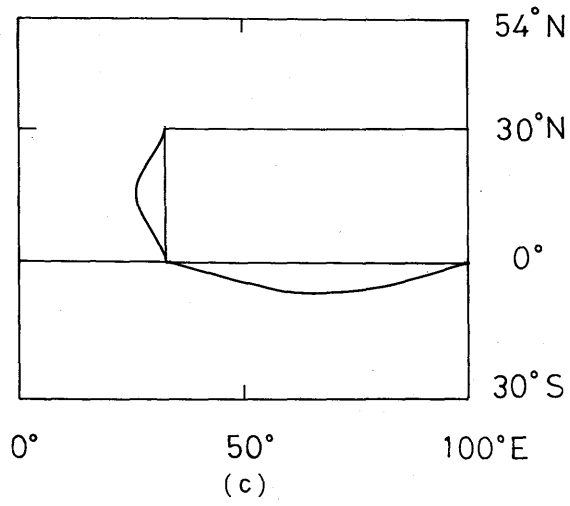


Fig. 4-1-1 Continued.

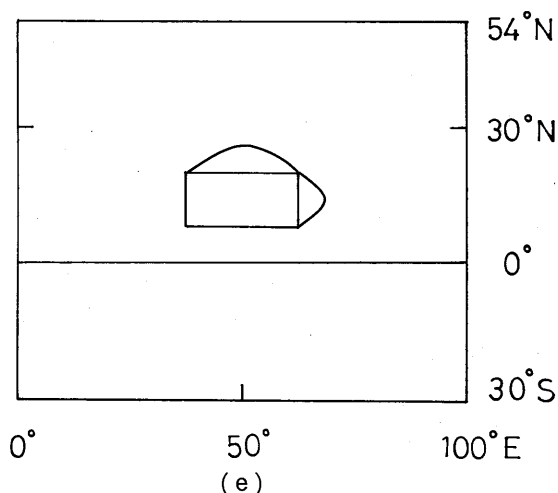


Fig. 4-1-1 Continued.

$$\begin{aligned}
 & -v' \frac{\partial T'}{\partial \phi} - w' \frac{\partial T'}{\partial z} + A_h \nabla^2 T' + \frac{K_h}{\delta} \frac{\partial^2 T'}{\partial z^2}, \quad (4-1) \\
 & \quad \quad \quad \text{(H)} \quad \quad \text{(I)} \quad \quad \text{(J)} \quad \quad \text{(K)}
 \end{aligned}$$

where the overbars denote the normals, and primes the anomalies. Terms (A), (B), and (E) denote the effect of advection of normal temperature field by anomalous currents, terms (C), (D), and (F) the effect of advection of anomalous temperature field by normal currents, and terms (G), (H), and (I) the effect of advection of anomalous temperature field by anomalous currents. Terms (J) and (K) are the diffusive change of anomalous temperature. If the normal state is horizontally uniform and motionless, as in case 101 and case 201, terms (A), (B), (C), (D), and (F) are always zero, and term (E) plays the most important role in the initial development of temperature anomalies.

It would be helpful for describing the oceanic response to tabulate the characteristics of the vertical normal modes in the model ocean in advance. Typical values for the first three baroclinic modes are given in Table 4-1-2 for a few typical stratifications. h is the equivalent depth associated with the given mode. $c = \sqrt{gh}$ is the phase speed of the corresponding gravity wave. L_R , the Rossby radius of deformation, is a characteristic horizontal length scale. c_R is the westward phase speed of the non-dispersive Rossby wave :

$$c_R = \frac{1}{3} \sqrt{gh} = \frac{1}{3} c \quad (\text{for an equatorial mode with meridional mode number } 1),$$

Table 4-1-2 Characteristics of the first three baroclinic modes in the model ocean, (a) (0°, 50°E), (b) (6°N, 50°E), and (c) (18°N, 50°E). d and y in the last line indicate that the unit is day and year, respectively.

	(a)			(b)			(c)		
mode	1	2	3	1	2	3	1	2	3
h cm	133	40	18	132	42	18	140	37	17
c cm/s	361	198	132	360	203	134	371	191	128
L_R km	397	294	240	236	133	88	82	42	28
c_R cm/s	120	66	44	127	40	17	15	3.9	1.8
T_R	107d	195d	294d	101d	318d	2.0y	2.3y	8.6y	19.1y

$$= \frac{\beta g h}{f^2} \quad (\text{for an off-equatorial mode}). \quad (4-2)$$

where β is the northward gradient of the Coriolis parameter f ($=2\Omega \sin\phi$). The eastward phase speed of the equatorially trapped Kelvin wave is equal to c . T_R indicates the time required for the Rossby wave to propagate from the eastern to the western boundary at each latitude. Fig. 4-1-2 shows the eigen modes of temperature change associated with the first three baroclinic modes. These changes arise through term (E) in Eq. (4-1). If we project the wind stress which acts as a body force in the uppermost layer into the vertical normal modes for the equatorial region, the second baroclinic mode is shown to have a slightly larger projection than the first. (Figures appearing in sections 4.2 and 4.3 are summarized in Table 4-1-3.)

4.2 Response to anomalous forcing in the equatorial ocean

4.2.1 Anomalous eastward wind (cases 100 and 101)

In case 100, anomalous eastward winds are imposed in the western two-thirds of the equatorial region (10°S—10°N) for 90 days (day 1—day 90) (Table 4-1-1(a), Fig. 4-1-1(a)). The maximum wind stress anomaly of 0.35 dyne/cm² nearly cancels the normal westward wind stress on the equator. There are no oceanic anomalies at the initial time. This experiment is intended to examine the oceanic response to *an abrupt relaxation of the easterly winds in the western equatorial ocean.*

Case 101 is an experiment which employs the same anomalous winds as case 100, whereas the initial state is horizontally uniform and motionless. The initial temperature and salinity

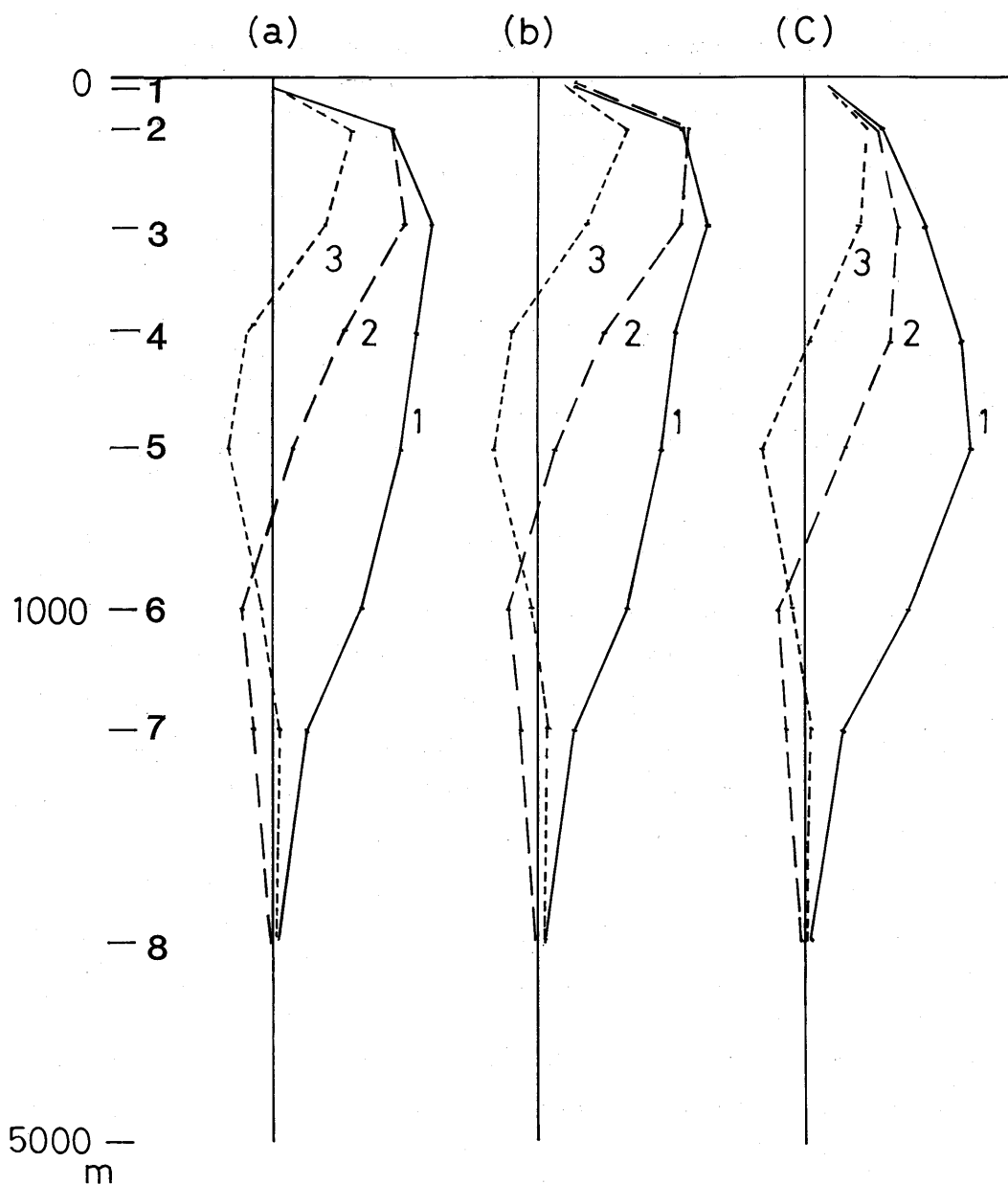


Fig. 4-1-2 Vertical structure of the temperature changes associated with the first three baroclinic modes, (a) ($0^\circ, 50^\circ\text{E}$), (b) ($6^\circ\text{N}, 50^\circ\text{E}$), and (c) ($18^\circ\text{N}, 50^\circ\text{E}$). Horizontal scale is arbitrary.

are those obtained by averaging the initial state of case 100 over the region from 10°S to 10°N and from 0° to 100°E . In this section, the results of case 100 are described first, then they are compared with those of case 101.

Table 4-1-3 List of figure numbers given in sections 4.2 and 4.3. λ , ϕ , z , k and t are longitude, latitude, height, level, and time, respectively. Units of (λ, ϕ) and t are degree and day, respectively.

Anomaly Case	$T'(\lambda, \phi)$ $t=90$	$T'(\lambda, \phi)$ $t=120$	$T'(\lambda, \phi)$ $t=180$	$T'(\lambda, \phi)$ $t=300$	$T'(\lambda, \phi)$ $t=360$	$T'(\lambda, \phi)$ $t=720$	$T'(\phi, z)$ $t=90$	$T'(\phi, z)$ $t=180$	$T'(\lambda, z)$ $\phi=0$	$T'(\lambda, z)$ $\phi=6$	$T'(\lambda, z)$ $\phi=14$	$T'(\lambda, z)$ $\phi=18$	$T'(\lambda, t)$ $\phi=0$	$T'(\lambda, t)$ $\phi=6$	$T'(\lambda, t)$ $\phi=18$	$T'(\phi, t)$ $k=1$	$T'(\lambda, t)$ $\phi=0$	Others	
100	4-2-2 (a)k=1 (b)k=2		4-2-6 (a)k=1 (b)k=2		4-2-7 (a)k=1 (b)k=2		4-2-3 (a) $\lambda=15$ (b) $\lambda=85$	4-2-4 (a) $\lambda=15$ (b) $\lambda=85$	4-2-5 (a)t=90 (b)t=180				4-2-8 (a)k=1 (b)k=2				4-2-10 (a) $\lambda=0$ (b) $\lambda=10$	4-2-9 (a)k=1 (b)k=2	4-2-1
101	4-2-11 (a)k=1 (b)k=2												4-2-12 (a)k=1 (b)k=2						
110	4-2-13 (a)k=1 (b)k=2		4-2-13 (c)k=1 (d)k=2										4-2-14 (a)k=1 (b)k=2					4-2-14 (c)k=1 (d)k=2 (e)k=6	
120													4-2-15 (a)k=2					4-2-15 (b)k=1	
130	4-2-17 (a)k=1 (b)k=2		4-2-17 (c)k=1 (d)k=2										4-2-16 (a)k=2					4-2-16 (b)k=1	
200			4-3-1 (a)k=1 (b)k=3		4-3-4 (a)k=1 (b)k=3	4-3-5 (a)k=1 (b)k=3			4-3-3 (b)t=180		4-3-3 (a)t=180		4-3-7 (a)k=1 (b)k=3	4-3-6 (a)k=1 (b)k=3				4-3-2 4-3-8	
201					4-3-9 (a)k=1 (b)k=3														
250		4-3-10 (a)k=1 (b)k=4		4-3-12 (a)k=1 (b)k=4								4-3-11 t=120							

The relaxation of the easterly winds results in an eastward acceleration in the upper ocean because of the initial eastward pressure force balanced with the normal westward wind stress.

Therefore, the westward equatorial current of the uppermost level decelerates, and then reverses its direction. This is evident in Fig. 4-2-1, which shows the evolution of the surface currents along the equator (see also Fig. 4-2-9(a)). As a result, the westward advection of the cold water upwelled on the equator weakens, and then an eastward advection of the warm water pooled in the western equatorial region takes place.

In the meridional section, anomalous equatorward convergent currents are induced in the surface layer, which are compensated by downwelling on the equator, upwelling on both sides of it, and poleward divergent motion at depth. This anomalous meridional circulation tends to raise the surface temperature along the equator by means of suppression of the equatorial upwelling, and also by horizontal heat advection since the normal temperature is maximum at 8°N and 8°S (Fig. 3-3(a)). Due to the combined effects of the anomalous horizontal and vertical advectons of normal temperature field (terms (A), (B), and (E) in Eq. (4-1)), anomalous temperatures initially develop in the forced region. Moreover, unforced regions may be affected by Kelvin and Rossby waves or advection of anomalies by normal currents.

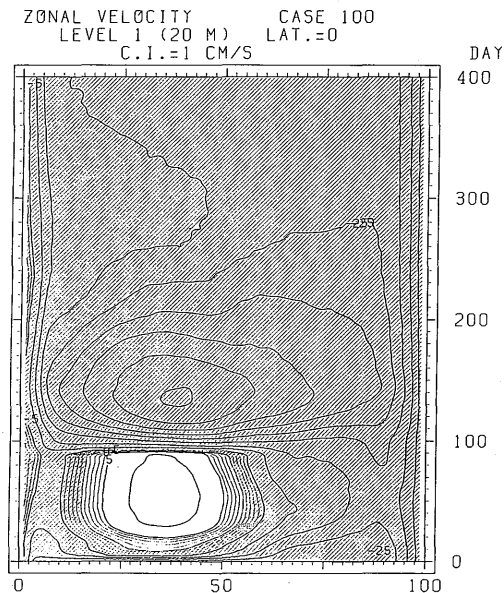


Fig. 4-2-1 Zonal velocity variations along the equator at level 1 in case 100. Shaded areas indicate westward flow.

Fig. 4-2-2 shows the temperature anomalies of level 1 and level 2 on day 90 when the anomalous winds are instantaneously turned off. A warm anomaly is formed along the equator at level 1. The anomaly is extended poleward along the eastern boundary. On either side of the equator, cold anomalies are formed along 8°N and 8°S . The anomaly pattern of level 2 is widely different from that of level 1. Anomalously cold water is developed under the surface warm anomaly in the western part of the forced region.

In the unforced equatorial region and along the eastern boundary warm anomalies develop at both levels. Magnitudes of the anomaly near the eastern boundary are larger at level 2 than at level 1. The cold anomalies of both level 1 and level 2 are centered at the latitudes where the normal temperature is maximum, i. e., 8°N and 8°S at level 1 and 4°N and 4°S at level 2. The pattern of level 2 is fairly similar to that of Fig. 6.6 in Leetmaa et al. (1981), which shows the adjustment of the model thermocline topography after a weakening of the westward trade winds in a longitudinally and latitudinally confined region.

Meridional sections within and east of the forced region are shown in Figs. 4-2-3 and 4-2-4. There is considerable difference in the development of anomalies between the forced and the unforced region. The anomaly pattern at 15°E on day 45 (not shown) is similar to that on day 90. At 85°E , on the other hand, the pattern changes between day 45 and day 90, which reflects the appearance of a deep cold anomaly after day 45.

The longitudinal dependence of the vertical structure is also evident in Fig. 4-2-5(a). The warm anomaly seen in Fig. 4-2-2(a) is confined to the uppermost level in the western half of the forced region, while it extends down to level 3 in the eastern half. Near the eastern boundary the warm anomaly penetrates to a deeper level and has a maximum value at level 2.

When the anomalous winds are turned off, the normal westward wind stress causes westward acceleration in the upper ocean since the normal eastward pressure force has already collapsed during the first 90 days. A much faster jet than the normal westward equatorial current appears for a certain period due to the acceleration (see Figs. 4-2-1 and 4-2-9(a)).

The temperature anomalies on day 180 are shown in Fig. 4-2-6. The cold and warm anomalies of level 1 that existed in the equatorial region on day 90 have moved away from the equator. Along the equator, cold anomalies are newly formed both at level 1 and level 2. Changes in meridional sections are seen in Figs. 4-2-3 and 4-2-4. (The warm anomalies centered at 20°N and 20°S in Fig. 4-2-4(b) are due to the convective adjustment.) The

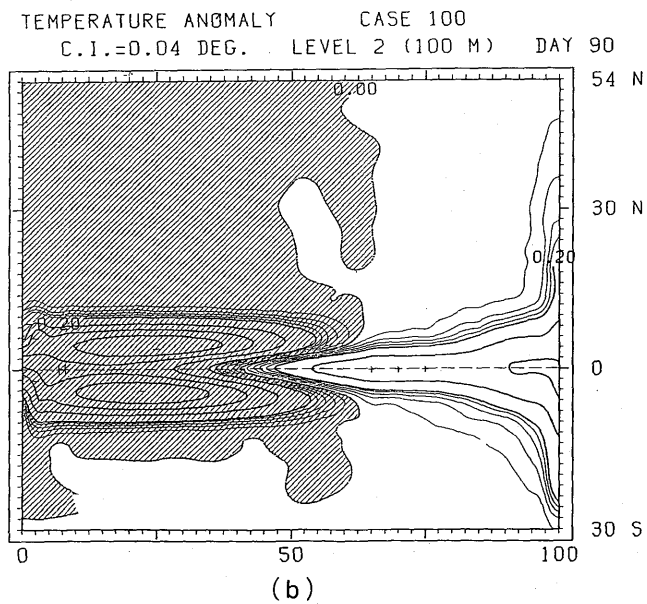
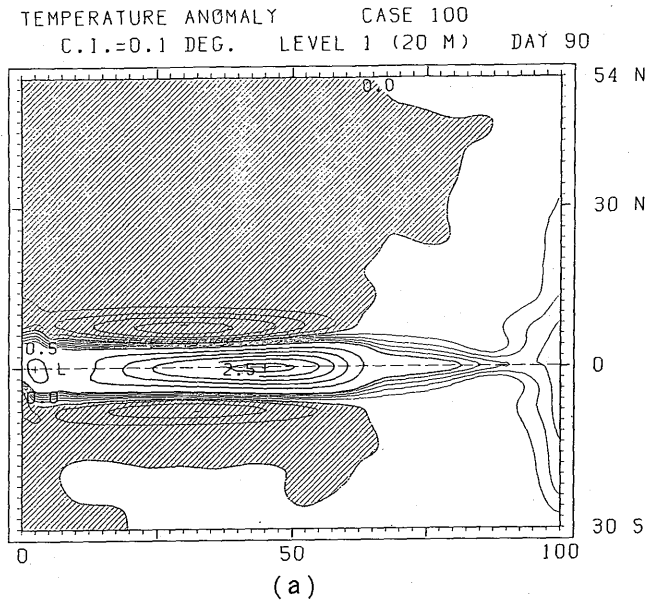
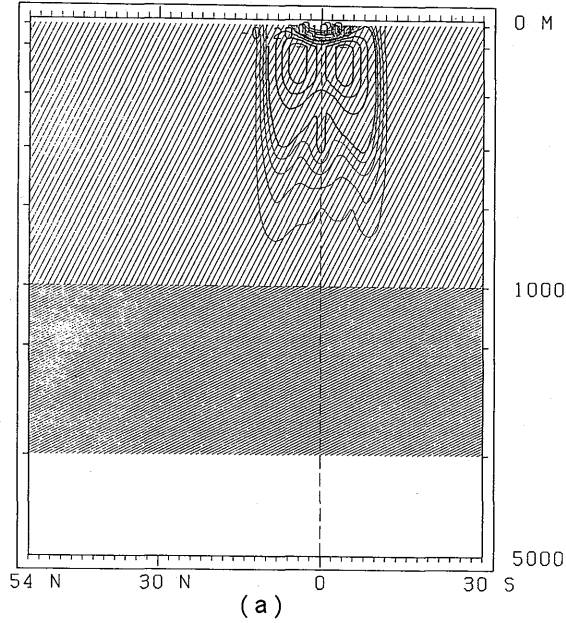


Fig. 4-2-2 Temperature anomalies on day 90 in case 100. (a) Level 1 and (b) level 2. Negative anomalies are shaded. *C.I.* indicates the interval of thin lines, while the interval of bold lines is five times *C.I.*. + and *L* indicate maximum and minimum in positive anomalies, and - and *H* indicate maximum and minimum in negative anomalies, respectively.

TEMPERATURE ANOMALY CASE 100
C.I.=0.04 DEG. LONG. =15.0 DAY 90



TEMPERATURE ANOMALY CASE 100
C.I.=0.04 DEG. LONG. =85.0 DAY 90

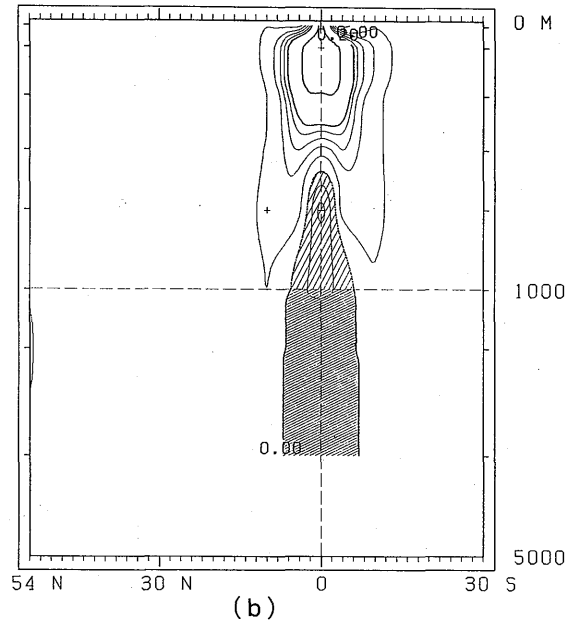
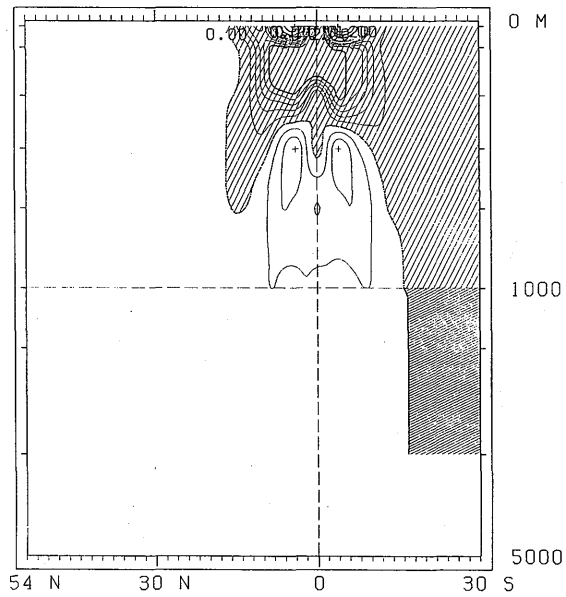


Fig. 4-2-3 Meridional cross-sections of the temperature anomalies on day 90 in case 100. (a) Along 15°E and (b) along 85°E.

TEMPERATURE ANOMALY CASE 100
C.I.=0.04 DEG. LONG. =15.0 DAY 180



TEMPERATURE ANOMALY CASE 100
C.I.=0.04 DEG. LONG. =85.0 DAY 180

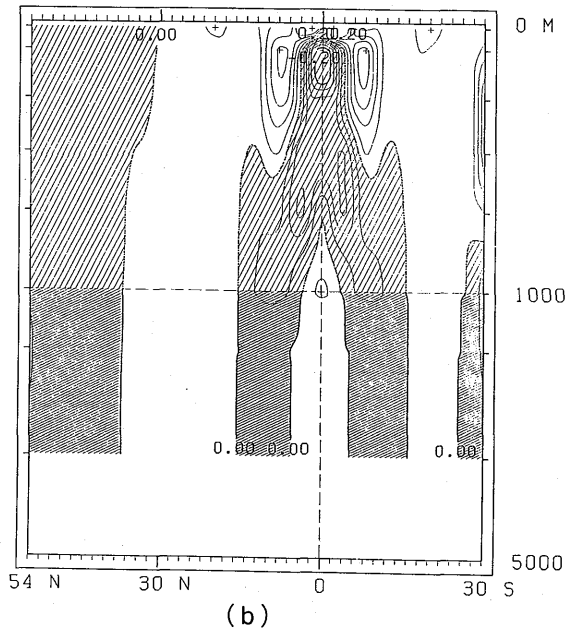


Fig. 4-2-4 As in Fig. 4-2-3 except for day 180.

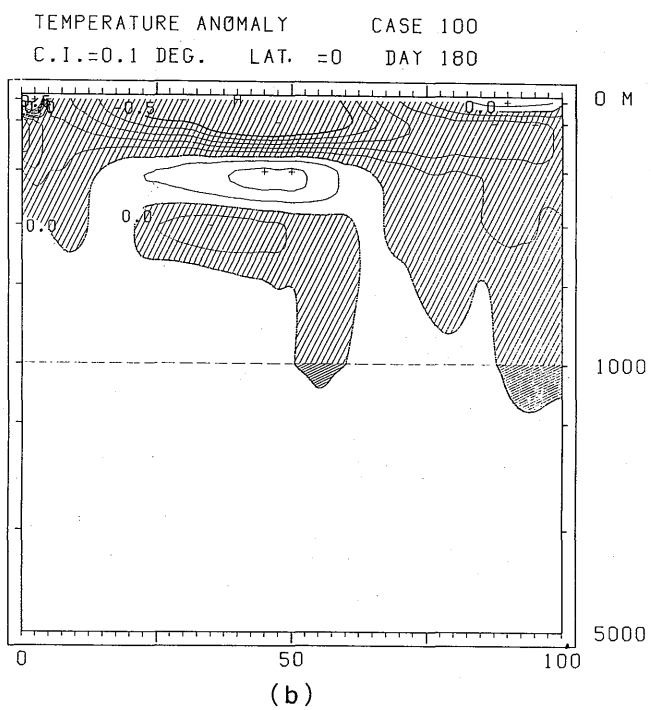
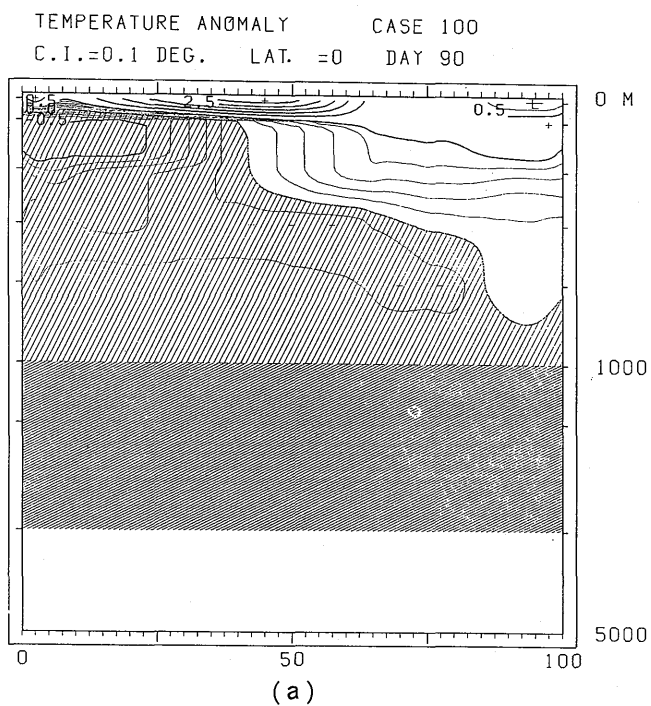


Fig. 4-2-5 Zonal cross-sections of the temperature anomalies along the equator in case 100. (a) Day 90 and (b) day 180.

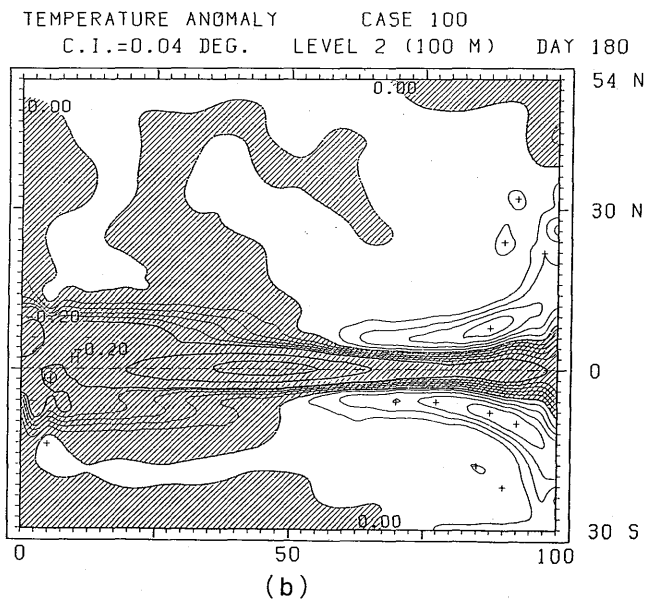
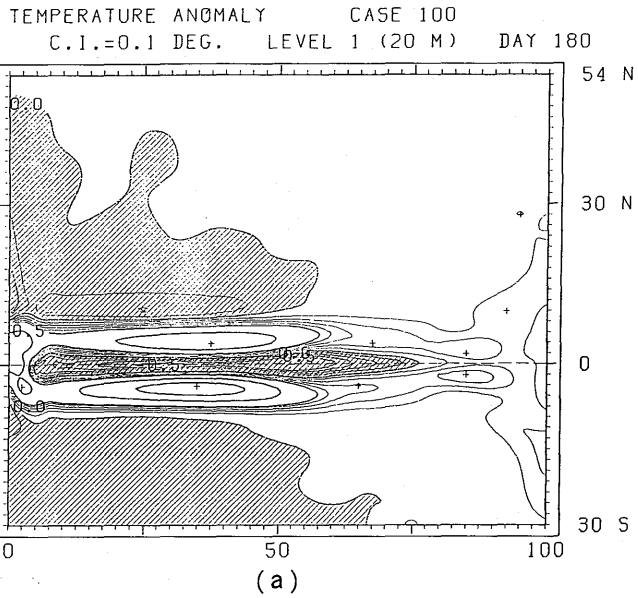


Fig. 4-2-6 As in Fig. 4-2-2 except for day 180.

section along the equator shown in Fig. 4-2-5(b) is entirely different from that on day 90.

It is not easy to identify which terms in Eq. (4-1) are responsible for the development of anomalies after day 90, since the anomalies produced during the first 90 days are large enough to change the normal state significantly. However, advection of anomalies by normal currents can presumably explain the anomaly development along the equator to some extent. At level 1, after anomalous forcing was switched off, the upwelling of cold water and poleward advection of warm water tend to diminish the existing warm anomaly, and then to generate a cold anomaly. At level 2, the normal equatorial motion converges the cold water on the equator and advects to the east.

Fig. 4-2-7 shows the temperature anomalies on day 360. The newly produced cold anomaly of level 1 is also split into two centers. At level 2, the cold anomaly along the equator is almost stationary.

Fig. 4-2-8 shows the temperature anomaly variations along the equator at level 1 and level 2. At level 1, anomalous water, both warm and cold, develops in the anomalously forced region. At level 2, the relatively fast eastward movement of a warm anomaly center and slow movement of a cold anomaly center are seen.

Fig. 4-2-9 shows the variations of the zonal velocity anomalies. At level 1, velocity anomalies are produced in the anomalously forced region. However, the phase of the velocity anomalies does not coincide with that of the temperature anomalies. The zonal velocity anomaly u' basically develops as a result of imbalance between pressure force and wind stress. The anomaly u' produced strongly affects the temperature anomaly development through the term $u' \partial \bar{T} / \partial x$ in Eq. (4-1). As long as u' does not change sign, the contribution of $u' \partial \bar{T} / \partial x$ to the anomaly development $\partial T' / \partial t$ has the same sign. It results in a delay of the phase of the temperature anomalies. At level 2, both eastward and westward displacements of anomalies are seen. When the easterly winds relax, the eastward current anomalies develop and the eastward equatorial undercurrent accelerates. Then the undercurrent decelerates (except near the western edge) due to weakening of the eastward pressure force in the upper ocean, and subsequently dies out in the eastern forced region. For a short period after day 90, westward currents appear. Then the equatorial undercurrent reappears.

As seen in Figs. 4-2-6 and 4-2-7, anomalies drift or extend poleward along the western boundary. The northward movement of the anomalies formed to the north of the equator is obvious from Fig. 4-2-10, which shows the surface temperature anomaly variations near the

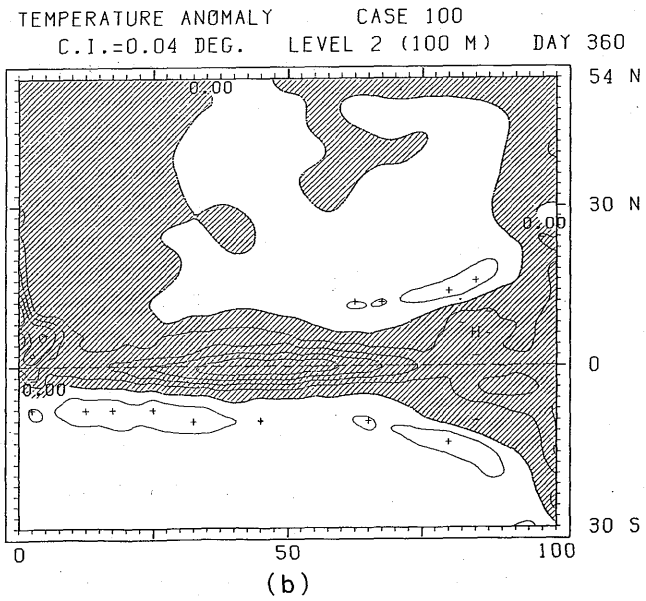
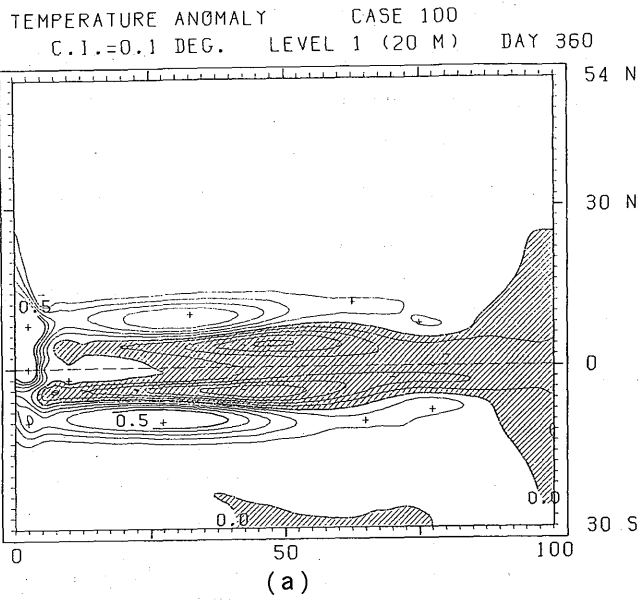


Fig. 4-2-7 As in Fig. 4-2-2 except for day 360.

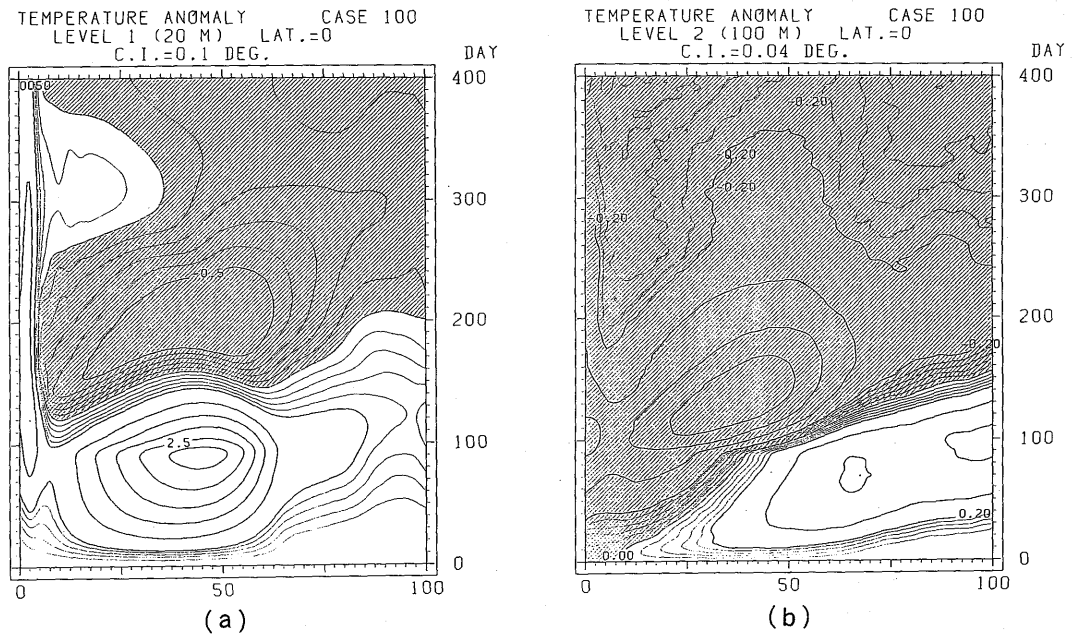


Fig. 4-2-8 Temperature anomaly variations along the equator in case 100.
(a) Level 1 and (b) level 2.

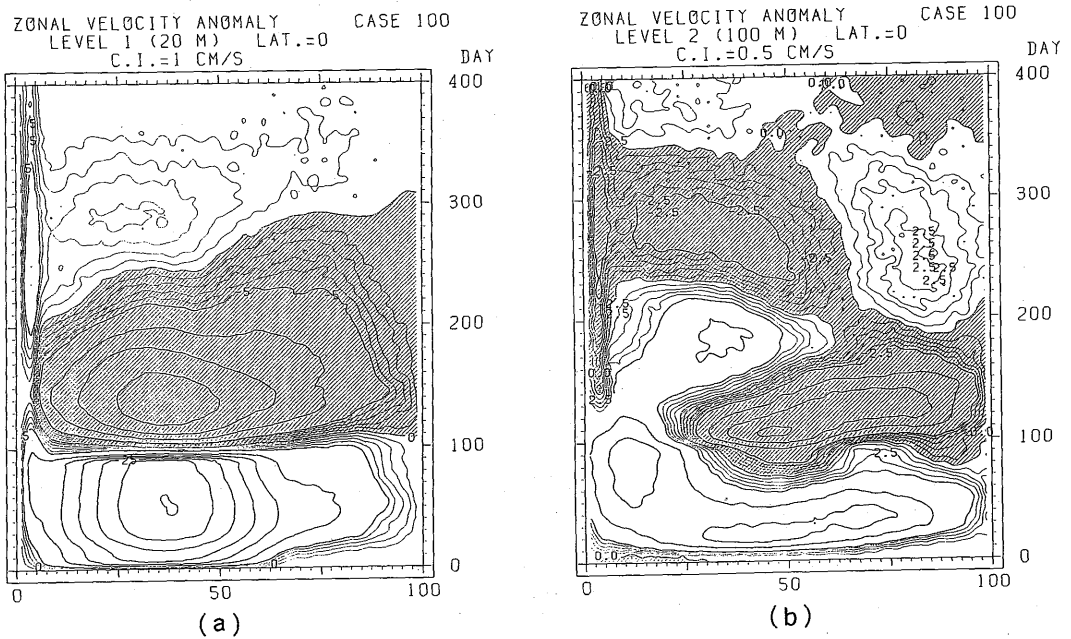
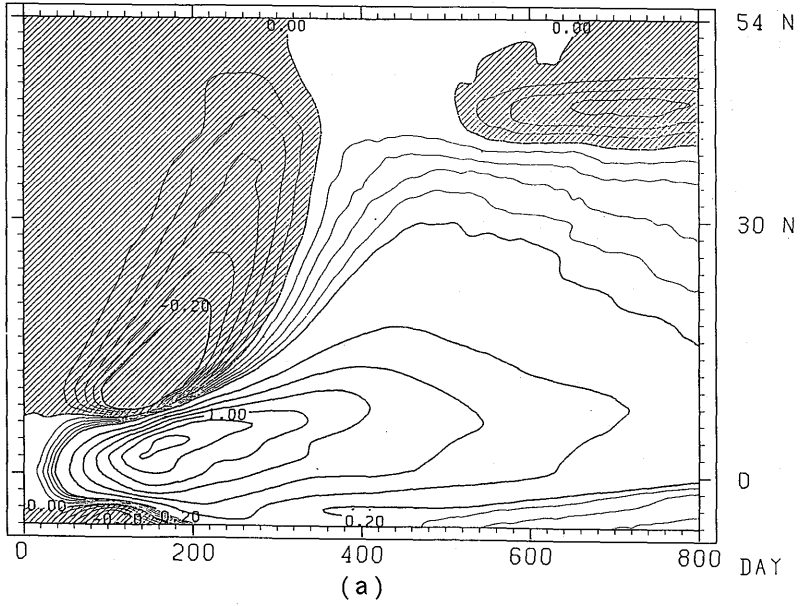


Fig. 4-2-9 As in Fig. 4-2-8 except for the zonal velocity anomalies.

TEMPERATURE ANOMALY CASE 100
LEVEL 1 (20 M) LONG.=0.0
C.I.=0.04 DEG.



TEMPERATURE ANOMALY CASE 100
LEVEL 1 (20 M) LONG.=10.0
C.I.=0.02 DEG.

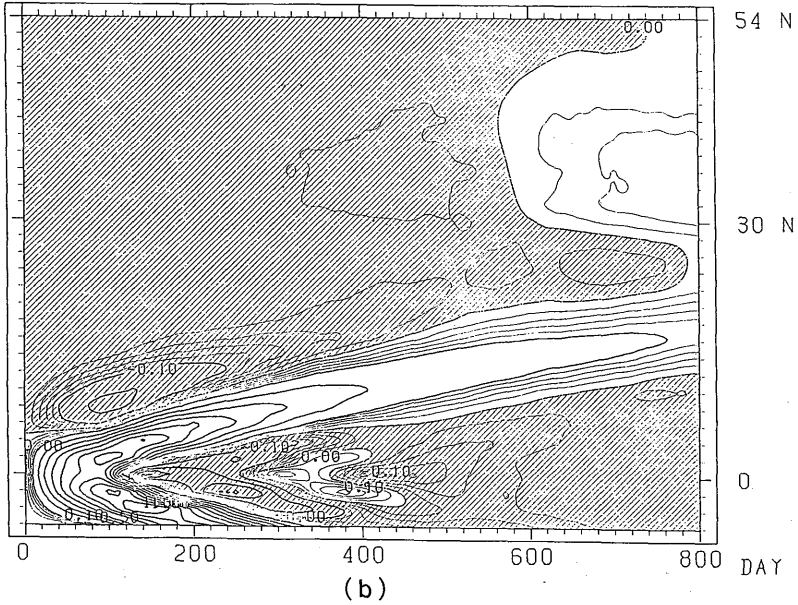


Fig. 4-2-10 Temperature anomaly variations at level 1 in case 100.
(a) Along the western boundary and (b) 10°E.

western boundary. The movement, 25° in latitude in 100 days at the western boundary (Fig. 4-2-10(a)) and 20° in 600 days at 10°E (Fig. 4-2-10(b)), is equivalent to speeds of about 30 cm/sec and 4 cm/sec, respectively. They are nearly equal to the normal current speed at the uppermost level (cf. Fig. 3-3 (d)). The cold anomaly which is seen at the western boundary north of 40°N after day 500 is partially due to surfacing of the cold water advected northward at level 2. The anomalous water north of 30°N at 10°E is advected eastward from the western boundary region.

Now, compare case 101 with case 100 in order to clarify the role of the normal temperature and currents on the anomaly development.

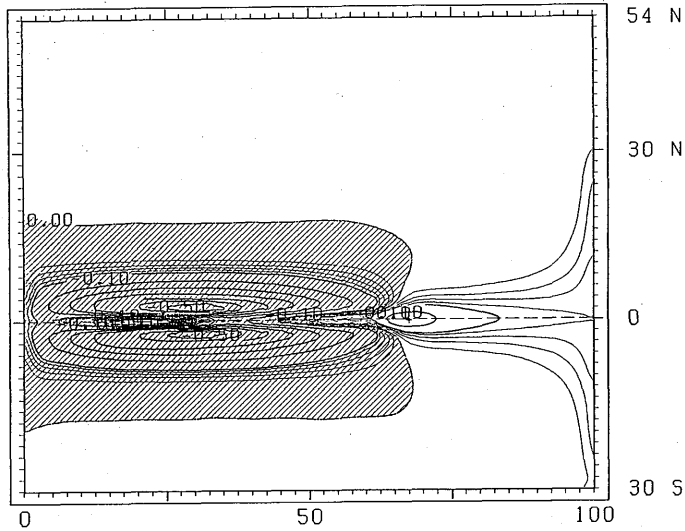
The results of case 101, the horizontal temperature anomaly distribution on day 90 and the temperature anomaly variations along the equator, are shown in Figs. 4-2-11 and 4-2-12. The largest difference between Figs. 4-2-2 and 4-2-11 is in the intensity and extent of surface warm anomaly in the anomalously forced region. In case 101, the warm water is only slightly seen on the equator. This difference in the anomaly development on the equator is also evident from Figs. 4-2-8(a) and 4-2-12(a).

In case 100, the surface warm anomaly in the forced region continues to grow until anomalous winds are turned off. In case 101, on the other hand, it ceases to grow halfway, and then begins to diminish except near the eastern edge. Vertical currents induced by the anomalous winds generate a warm anomaly on the equator in both cases. In case 101, however, once cold anomalies are generated by upwelling on both sides of the equator, the equatorward advection by meridional circulation comes into play. In case 100, as explained above, the eastward advection of normal temperature field by longitudinal circulation plays an important role in generating the warm anomaly. This process, further, is able to explain a relatively large magnitude of the warm anomaly near the eastern boundary in case 100 compared to case 101.

The anomaly distribution at level 2 is not so different as that at level 1. However, two differences between Figs. 4-2-8(b) and 4-2-12(b) are noted. One is that the warm anomaly in the forced region grows more rapidly in case 101 than in case 100. The other is that the eastward expansion of the cold anomaly region is swifter in case 100.

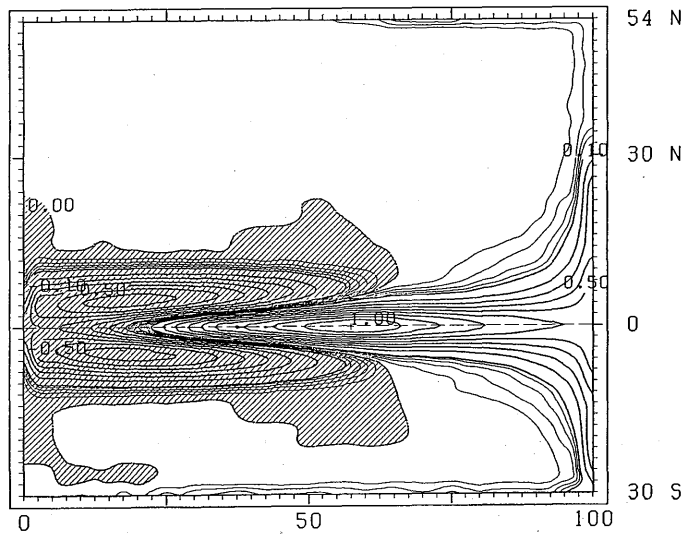
The evolutions after day 90 are very different between the two cases. All anomalies simply diminish to zero in case 101.

TEMPERATURE ANOMALY CASE 101
C.I.=0.02 DEG. LEVEL 1 (20 M) DAY 90



(a)

TEMPERATURE ANOMALY CASE 101
C.I.=0.02 DEG. LEVEL 2 (100 M) DAY 90



(b)

Fig. 4-2-11 As in Fig. 4-2-2 except for case 101.

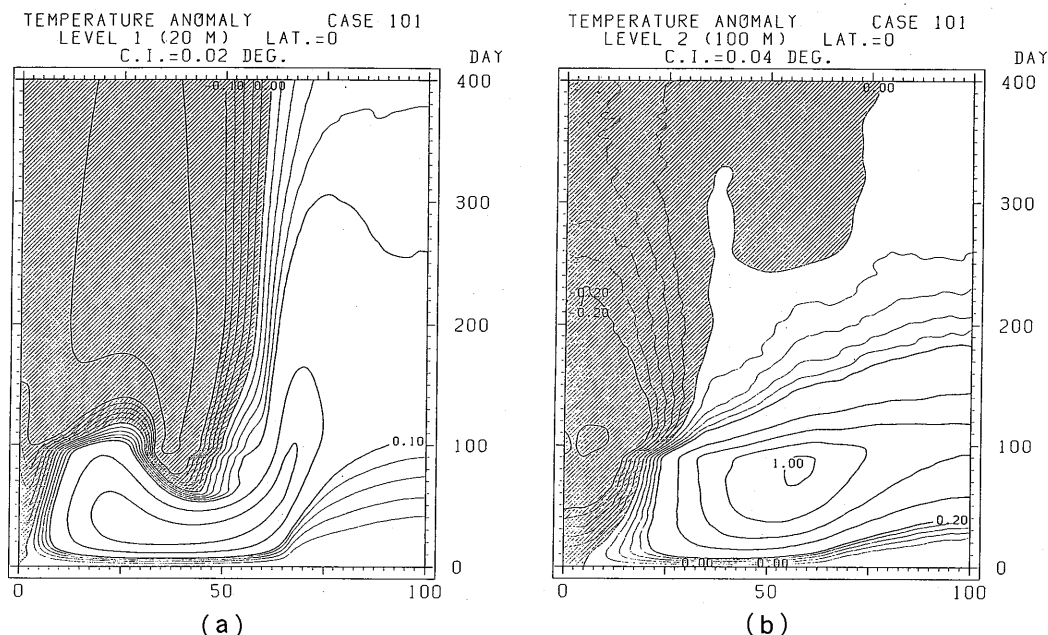


Fig. 4-2-12 As in Fig. 4-2-8 except for case 101.

4.2.2 Effect of the difference in the longitude of the forcing anomaly (cases 110, 120 and 130)

In this section, three experiments are described, in which anomalous eastward winds are imposed in the western, central, and eastern thirds of the equatorial region (10°S – 10°N), respectively (Table 4-1-1(a), Fig. 4-1-1(b)). The purpose of the experiments is to see how the generation and evolution of anomalies depend on the longitudinal location of the anomalously forced region. The anomalous winds are introduced by stopping the normal westward winds in each region for 90 days.

Figs. 4-2-13 and 4-2-14 show the results of case 110. They are qualitatively similar to the results of case 100, but there are some differences caused by the change in the anomalous wind forcing region (cf. Figs. 4-2-2, 4-2-6, 4-2-8, and 4-2-9).

Firstly, the cold anomalies on both sides of the equator on day 90 are centered at latitudes further poleward. Secondly, the warm anomalies in the unforced region are smaller. Thirdly, Kelvin and Rossby waves are more clearly discernible. The reason for the last difference is that the western and eastern edges of the anomalous winds are more sharply defined in case 110. When the anomalous winds are imposed or turned off, Kelvin and Rossby waves are excited at each of the edges. In addition to these waves, Rossby waves are excited at the eastern boundary due to the reflection of the initially excited Kelvin

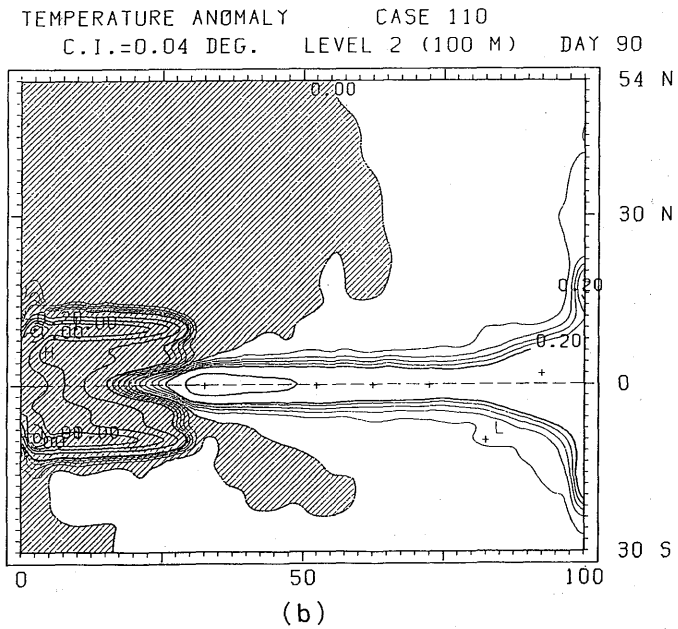
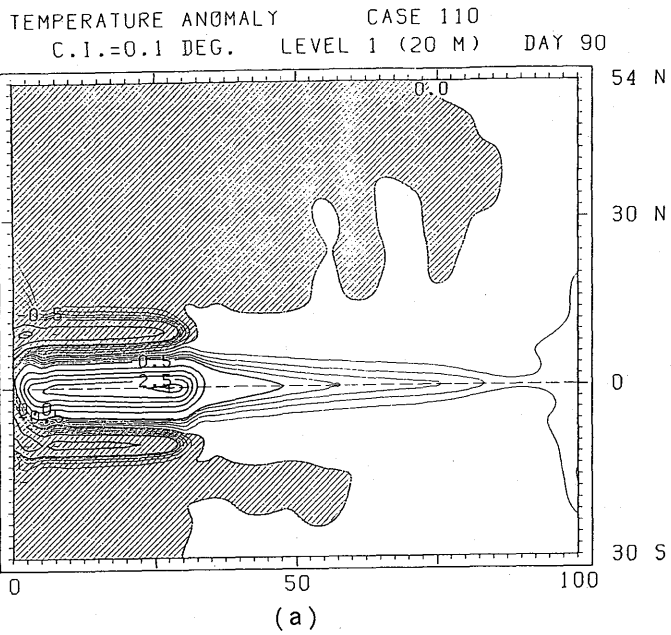
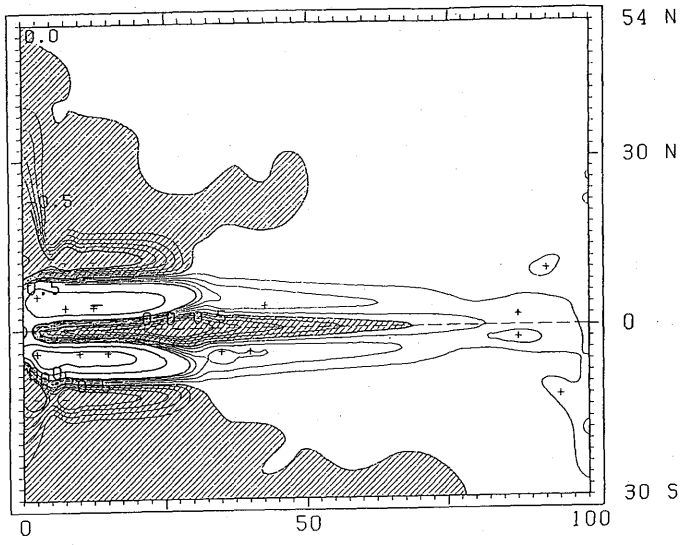


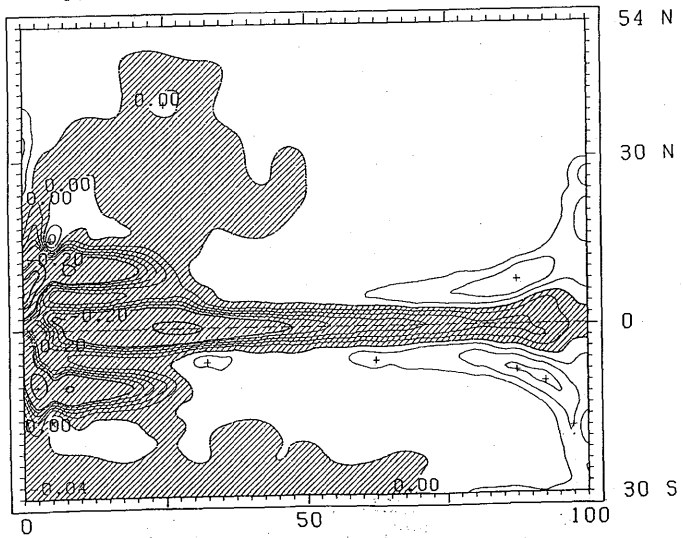
Fig. 4-2-13 Temperature anomalies in case 110. (a) Level 1 and (b) level 2 on day 90, and (c) level 1 and (d) level 2 on day 180.

TEMPERATURE ANOMALY CASE 110
C.I.=0.1 DEG. LEVEL 1 (20 M) DAY 180



(c)

TEMPERATURE ANOMALY CASE 110
C.I.=0.04 DEG. LEVEL 2 (100 M) DAY 180



(d)

Fig. 4-2-13 Continued.

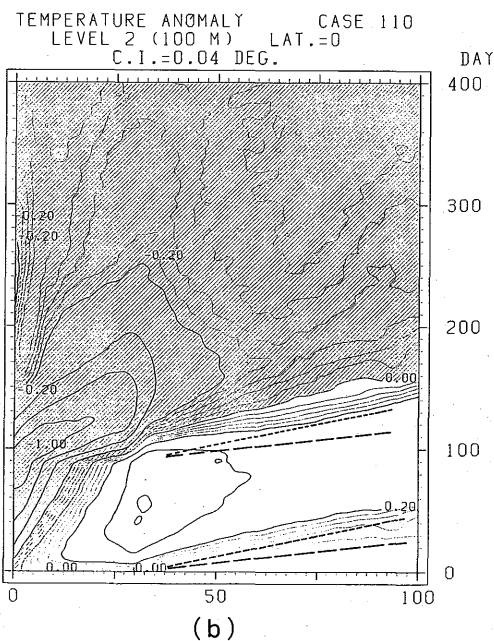
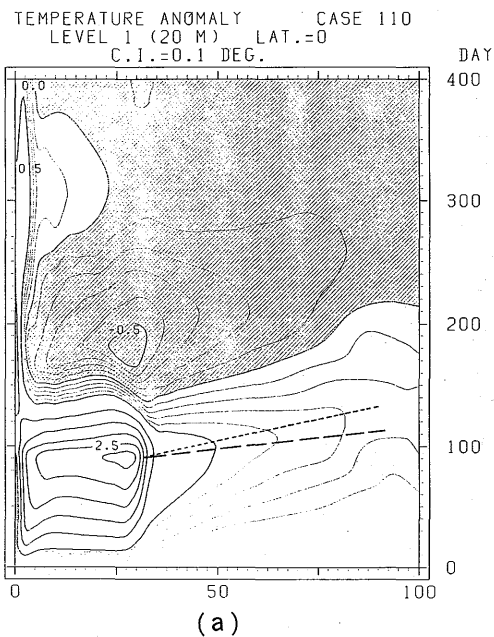


Fig. 4-2-14 Evolution of the conditions along the equator in case 110. The temperature anomalies at (a) level 1 and (b) level 2, and the zonal velocity anomalies at (c) level 1, (d) level 2, and (e) level 6. The dashed lines and the dotted lines correspond to Kelvin and non-dispersive Rossby waves of the first baroclinic mode and the second baroclinic mode, respectively.

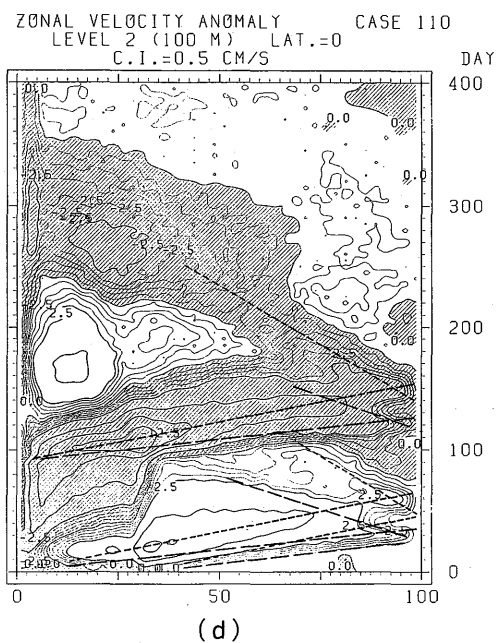
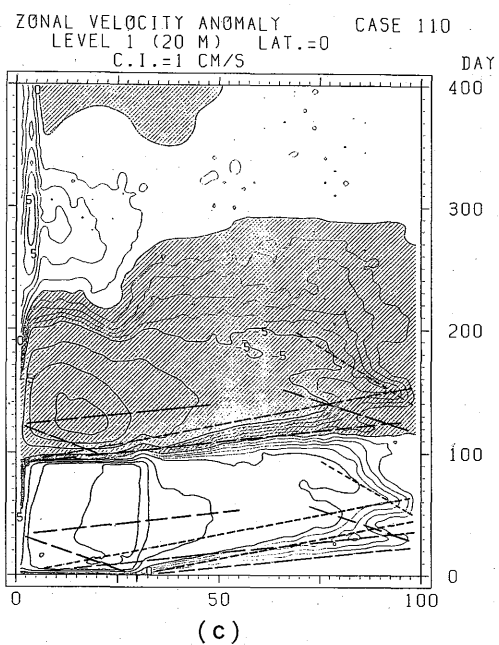


Fig. 4-2-14 Continued.

waves, and Kelvin waves are excited at the western boundary due to the reflection of the initially excited Rossby waves. The dashed lines and dotted lines in Fig. 4-2-14 correspond to the first baroclinic mode and second baroclinic mode Kelvin and non-dispersive Rossby waves. The horizontal velocity components (not shown here) of the first mode have a node between level 6 and level 7, while those of the second baroclinic mode have maximum amplitudes at level 1, level 6, and level 8. Hence the second mode is dominant in the horizontal motion at level 6, which is seen in Fig. 4-2-14(e). Rossby waves due to reflections at the eastern boundary are not clearly seen, especially in the temperature changes.

Figs. 4-2-15 and 4-2-16 show anomaly variations in case 120 and case 130. In the anomalously forced region, the response is qualitatively similar within the three. To the east of the forced region, temperature anomalies are produced as far as the eastern boundary, whereas to the west, significant anomalies are confined to the vicinity of the forced region. Velocity anomalies, in contrast to temperature anomalies, propagate westward as well as eastward, although westward propagating signals are generally weak. Thus, the equatorial region west of the forced region is less affected compared with the region to the east. The reason is related to the presence of the eastward undercurrent (Philander, 1981). Fig. 4-2-17 shows the temperature anomalies of case 130. The pattern in the forced region on

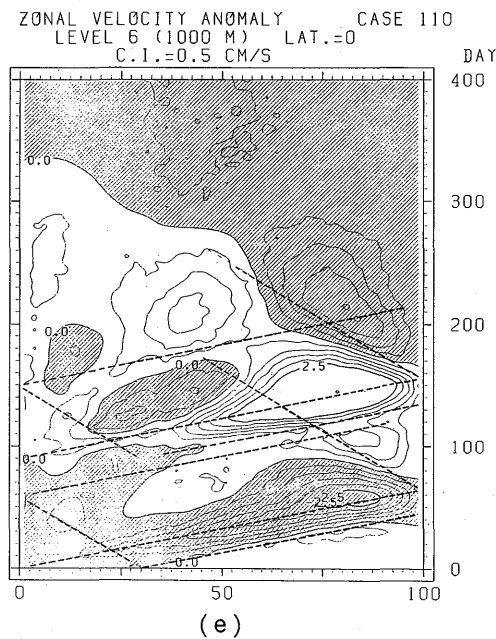


Fig. 4-2-14 Continued.

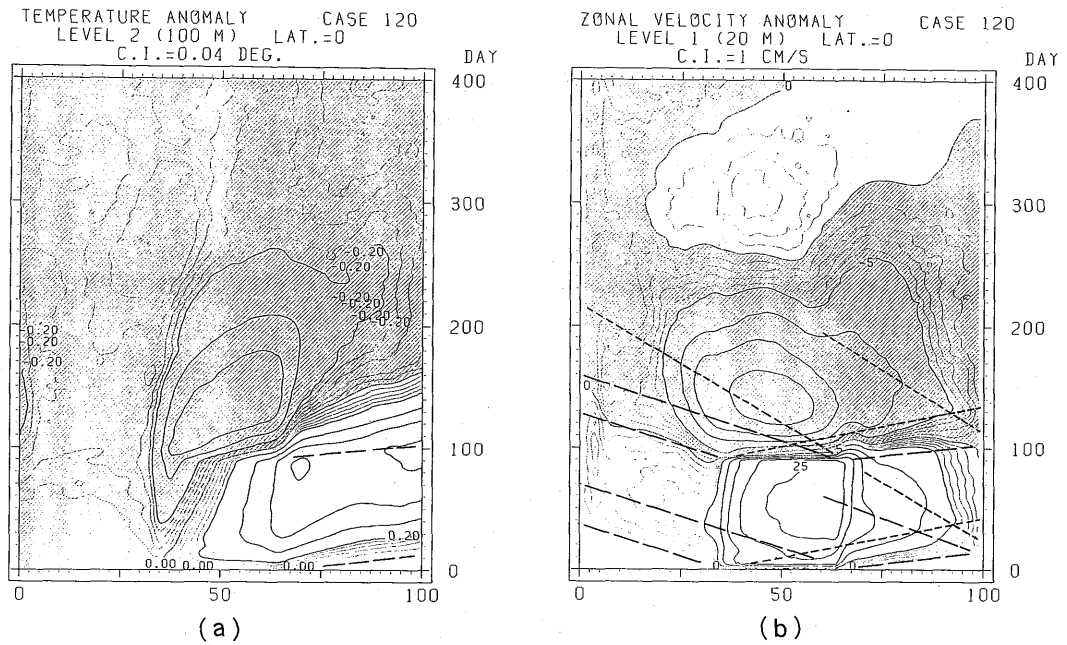


Fig. 4-2-15 Evolution of (a) the temperature anomalies at level 2 and (b) zonal velocity anomalies at level 1 along the equator in case 120.

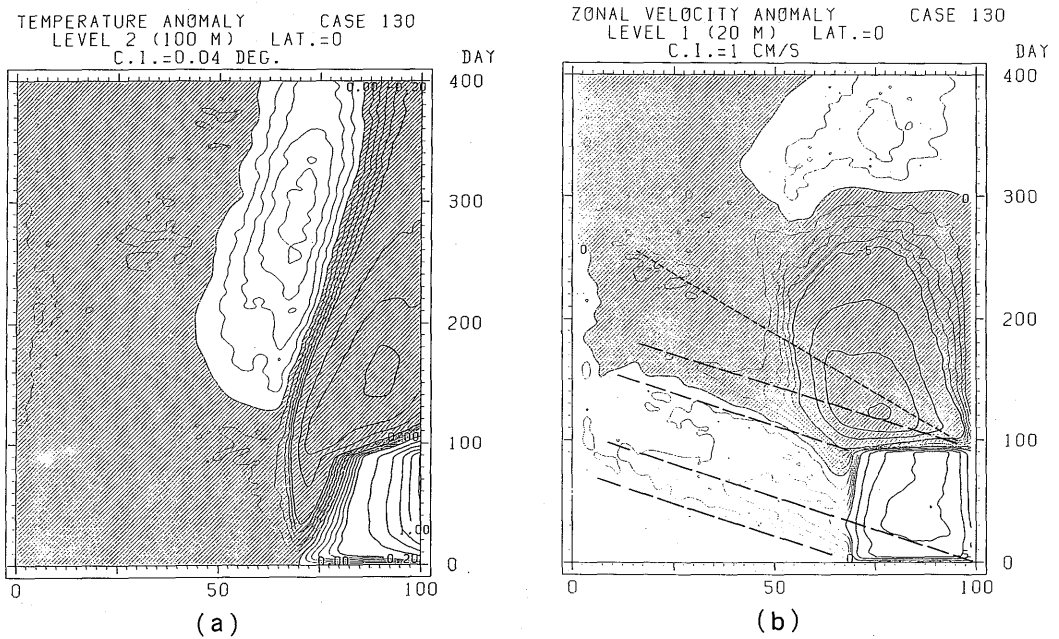


Fig. 4-2-16 As in Fig. 4-2-15 except for case 130.

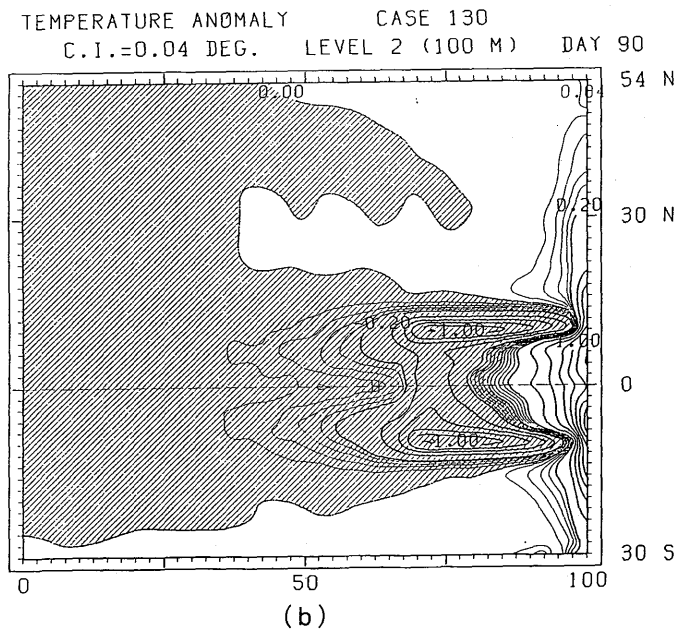
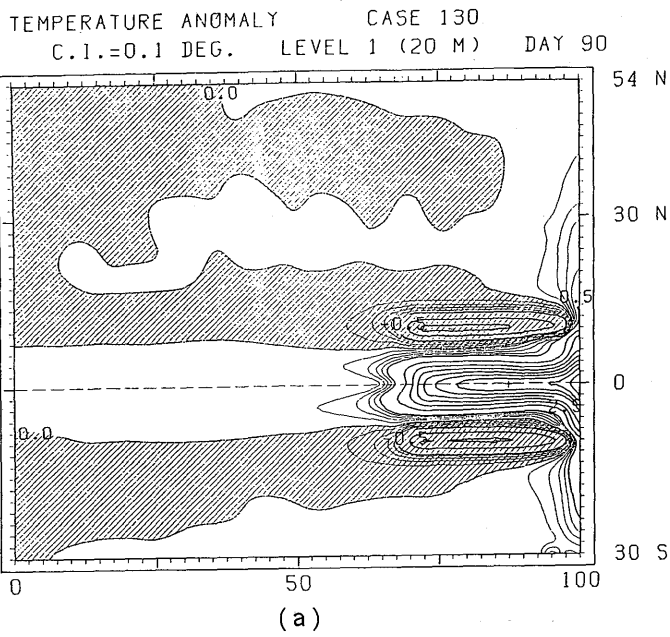


Fig. 4-2-17 As in Fig. 4-2-13 except for case 130.

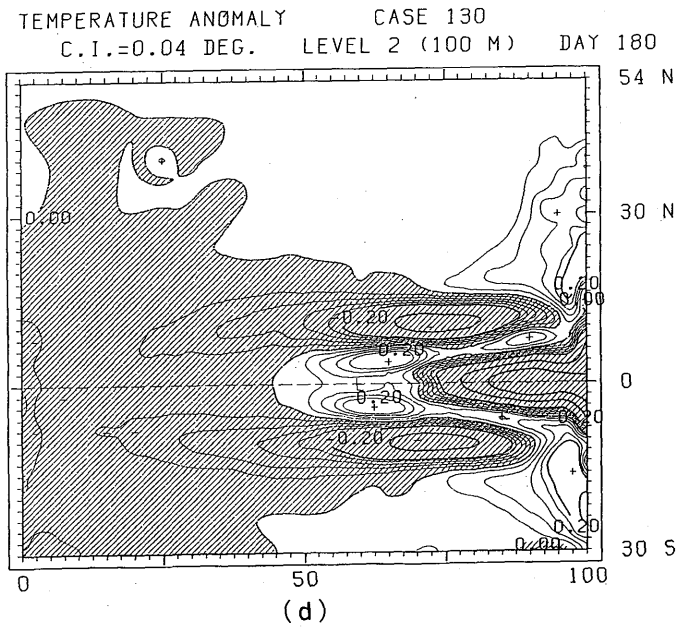
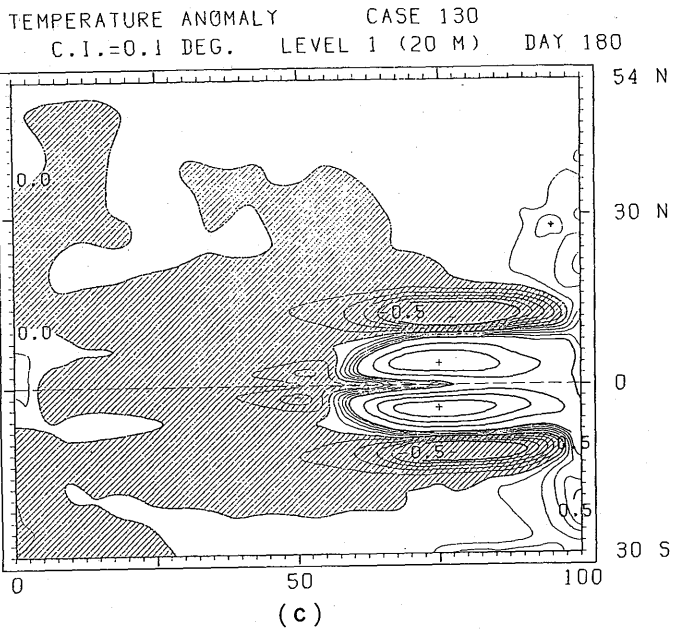


Fig. 4-2-17 Continued.

day 90 is almost the same as that of case 110 (Figs. 4-2-13 (a) and (b)) except near the eastern and western edges. The cold anomalies generated on either side of the equator propagate to the west in contrast to the temperature changes along the equator (see Fig. 4-2-17 (d)).

4.3 Response to anomalous forcing in the extra-equatorial ocean

4.3.1 Anomalous trade wind increase (cases 200 and 201)

In case 200, anomalous westward winds are imposed in the eastern two-thirds of the tropical and subtropical ocean (0° – 30° N) for 180 days (day 1—day 180) (Table 4-1-1(a), Fig. 4-1-1(c)). The maximum wind stress anomaly of 0.35 dyne/cm^2 increases the normal westward stress at 15° N by about 50%. The purpose of the experiment is to see how the thermal field evolves in response to an abrupt intensification of the trade winds.

The anomalous westward winds induce anomalous northward Ekman currents in the surface layer. The Ekman currents converge on the north side of 11° N and diverge on the south side. (Due to the meridional variation of the Coriolis parameter, the maximum Ekman currents are induced on the south side of the latitude of the maximum wind stress anomaly.) The horizontal convergence and divergence induce anomalous vertical advection of heat. Consequently, a pair of anomalous warm temperature and cold temperature develops in the forced region. The northward advection of normal temperature field by the anomalous Ekman currents (up to about 2 cm/sec) amplifies both the warm and the cold anomalies at level 1 because warm water is located along 8° N (Fig. 3-3(a)). Moreover, horizontal advection of normal temperature field by the anomalous geostrophic currents associated with the anomalous temperatures plays a significant role in the anomaly development at upper levels, especially at level 1.

Fig. 4-3-1 shows the temperature anomalies of level 1 and level 3 on day 180 when the anomalous winds are instantaneously turned off. A warm anomaly is generated to the north of 12° N and a cold anomaly to the south. The anomaly distribution is different between level 1 and level 3. The anomalies of level 1, centered at (20° N, 62.5° E) and (6° N, 70° E), are mostly confined to the forced region, while those of level 3 are displaced westward. The displacement of the cold anomaly is larger than that of the warm anomaly. Fig. 4-3-2 shows the time development of anomalies at two stations where the warm and cold anomaly centers of level 1 are located on day 180. It is evident that anomaly development in the forced region is predominant at level 1. Horizontal advection of normal temperature field is the most

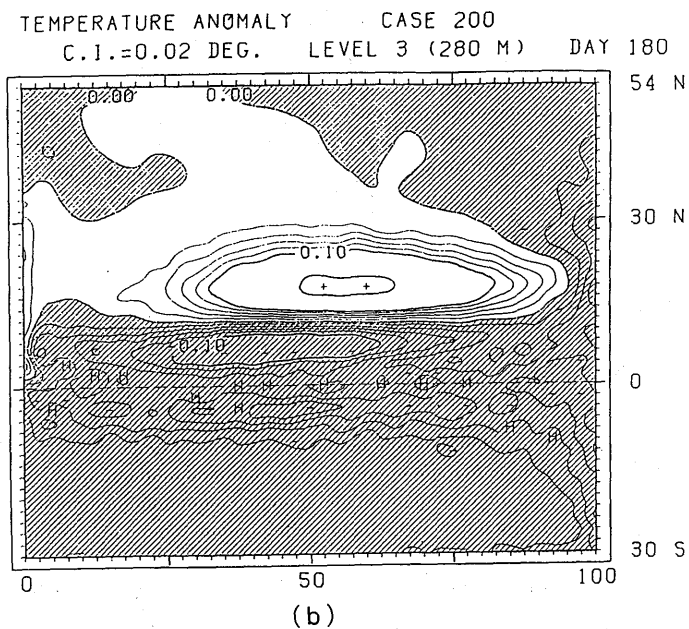
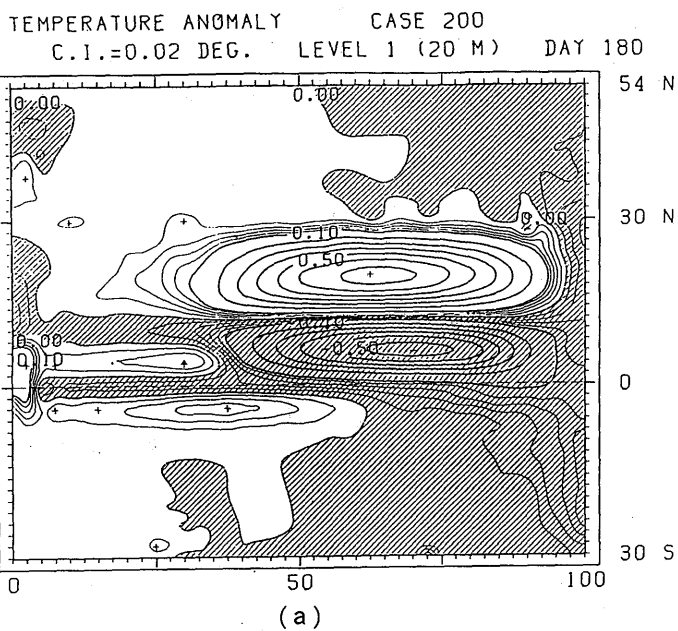


Fig. 4-3-1 Temperature anomalies on day 180 in case 200. (a) Level 1 and (b) level 3.

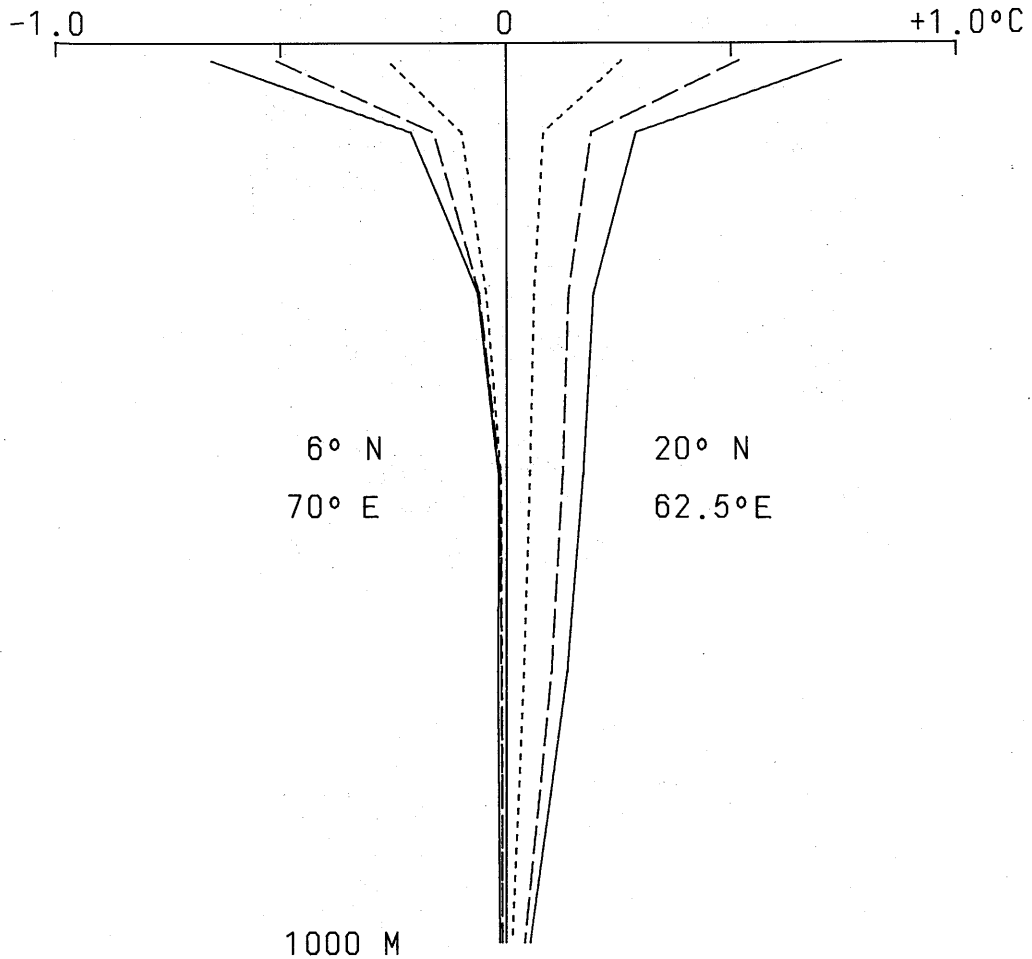


Fig. 4-3-2 Time development of the temperature anomalies at two stations, (20°N, 62.5°E) and (6°N, 70°E), in case 200. The dotted, dashed, and solid lines show the profiles on day 60, 120, and 180, respectively.

important factor in generating anomalies at level 1, which will be discussed later in connection with case 200.

The small-scale anomalies close to the western boundary in Fig. 4-3-1 are due to the meridional advection of normal temperature field by intensified western boundary currents. Although anomalous winds are imposed in the northern ocean, the anomaly distribution in the western equatorial region is symmetric about the equator. Cold anomalies are also symmetric along the eastern boundary.

Dividing the wind stress anomaly imposed in the equatorial region into a symmetric and an antisymmetric part with respect to the equator, the response in linear dynamics can be

considered as a sum of responses to the symmetric part and to the antisymmetric part. The latter response is confined to the equatorial region (McCreary, 1976). The warm anomalies on both sides of the equator of level 1 are due to the advection of warm water by the anomalous currents associated with the subsurface cold anomalies.

Fig. 4-3-3 shows zonal vertical sections through the warm and the cold anomalies in Fig. 4-3-1. There are two remarkable differences between the anomaly patterns. The first is that the warm anomaly penetrates to a greater depth than the cold anomaly. The second is that the subsurface center of the cold anomaly is displaced further westward than that of the warm anomaly. The western edge of the cold anomaly has already reached the western boundary at the subsurface (see Fig. 4-3-7 (b)). These differences are also obvious in Figs. 4-3-1 and 4-3-2. The latter difference can be attributed to the different phase speeds of Rossby waves. At 18°N , the fastest baroclinic Rossby wave propagates only 18° in longitude for 180 days, while at 6°N even the non-dispersive Rossby wave of the third baroclinic mode can propagate about 25° in longitude (Table 4-1-2).

Figs. 4-3-4 and 4-3-5 show the anomalies on day 360 and day 720, and Figs. 4-3-6 and 4-3-7 show the evolution of the temperature anomalies along 18°N and 6°N , respectively. The warm anomaly north of 12°N of level 1 expands to the west and drifts northward as a whole between day 180 and day 360. Then the anomaly is split into two parts as shown in Fig. 4-3-5(a). One of them moves east-northeastward, and the other moves westward. The propagation speed about 3 cm/sec of the eastern anomaly center is comparable to the normal current speed (Fig. 3-3(d)). Once the western anomaly arrives in the western boundary region, it moves northward along the boundary. The warm anomaly of level 3 drifts westward as a whole, then it extends northward along the western boundary.

Fig. 4-3-6 shows that the western edge of the warm anomaly of level 1 rapidly expands to the west, while the anomaly center itself slowly drifts to the west. The expansion speed is almost equal to that of the western edge of level 3, and also the propagation speed of the warm anomaly center of level 3 after day 180. This speed is approximately identical with the phase speed of the non-dispersive Rossby wave of the first baroclinic mode. The zonal component of the normal currents at 18°N , eastward at level 1 and westward at level 3, is far slower than the expansion speed.

The cold anomaly south of 12°N of level 1 is shown to have drifted northwestward as a whole between day 180 and day 720. Its center moves northward at first, then northwestward. The propagation speed is comparable to the normal current speed of 3–5 cm/sec.

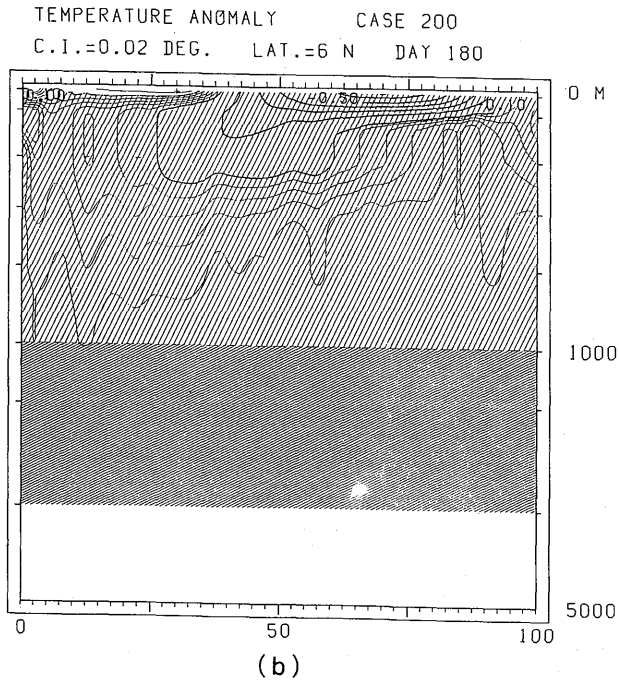
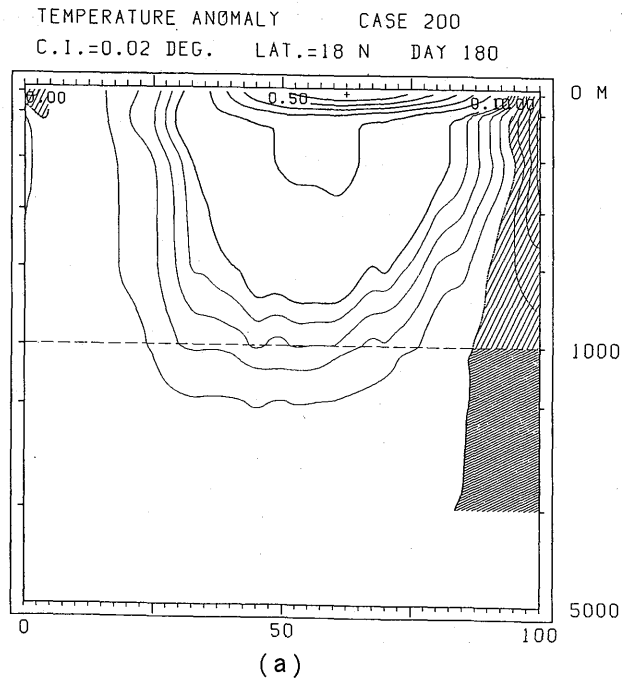
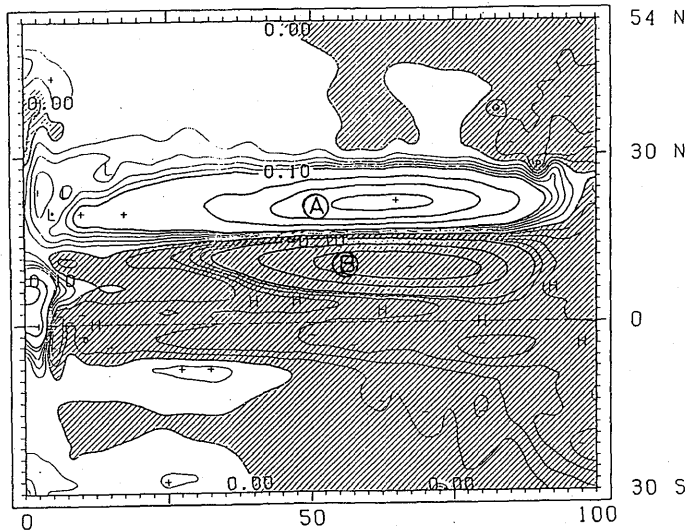


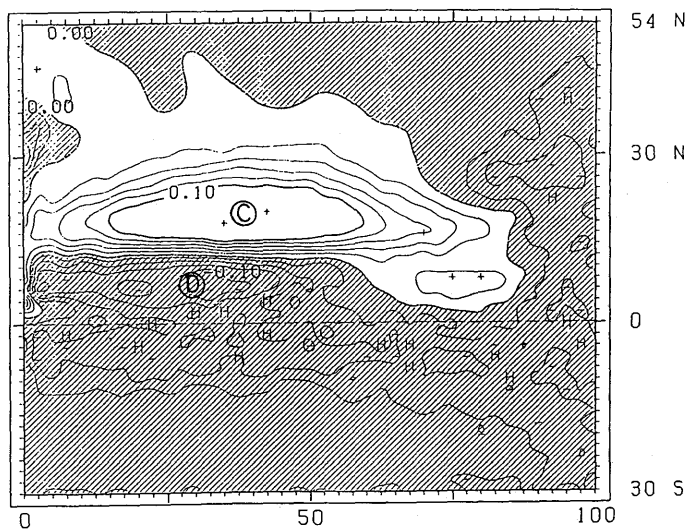
Fig. 4-3-3 Zonal cross-sections of the temperature anomalies on day 180 in case 200. (a) Along 18°N and (b) 6°N.

TEMPERATURE ANOMALY CASE 200
C.I.=0.02 DEG. LEVEL 1 (20 M) DAY 360



(a)

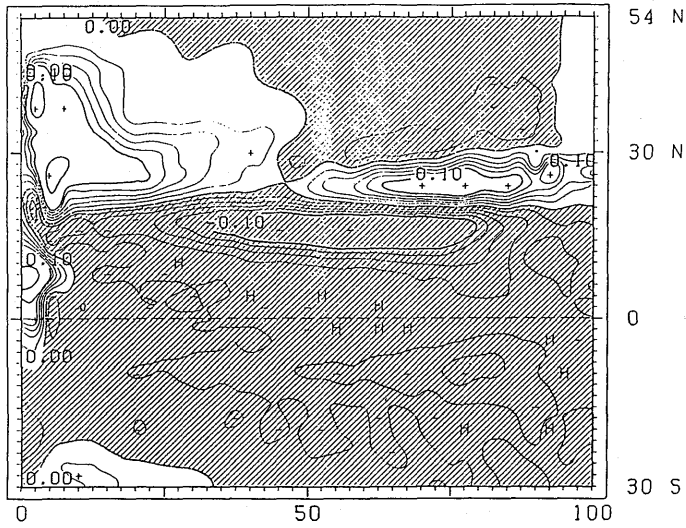
TEMPERATURE ANOMALY CASE 200
C.I.=0.02 DEG. LEVEL 3 (280 M) DAY 360



(b)

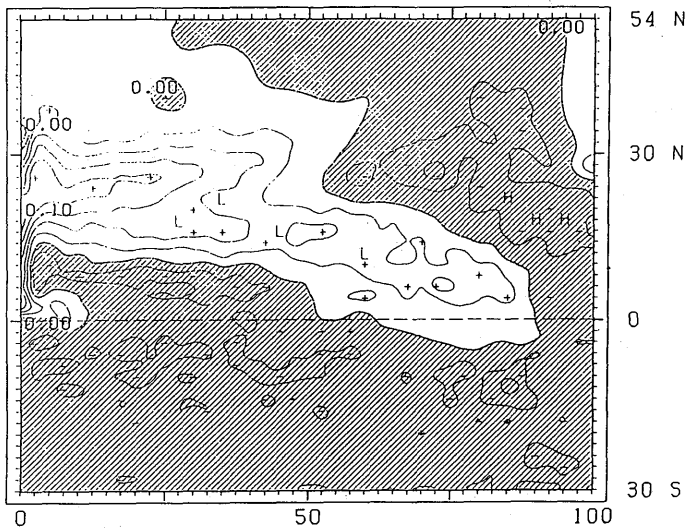
Fig. 4-3-4 As in Fig. 4-3-1 except for day 360.

TEMPERATURE ANOMALY CASE 200
C.I.=0.02 DEG. LEVEL 1 (20 M) DAY 720



(a)

TEMPERATURE ANOMALY CASE 200
C.I.=0.02 DEG. LEVEL 3 (280 M) DAY 720



(b)

Fig. 4-3-5 As in Fig. 4-3-1 except for day 720.

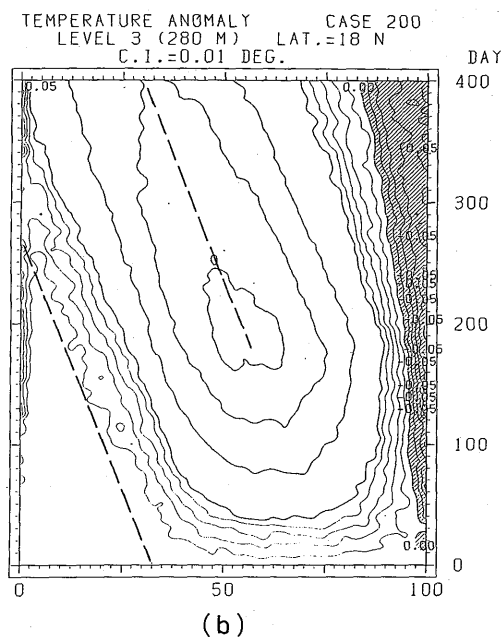
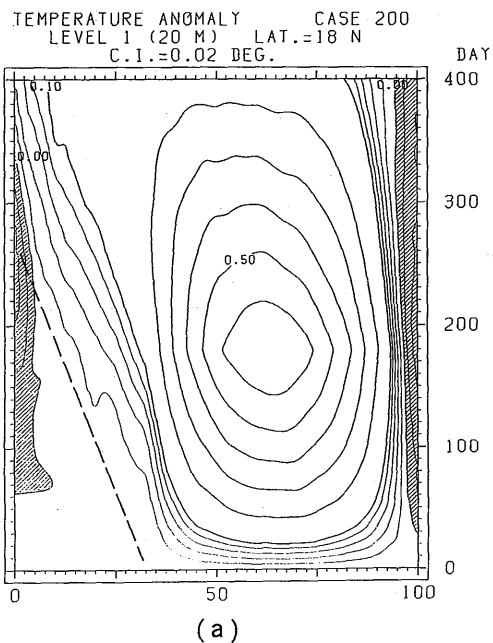


Fig. 4-3-6 Temperature anomaly variations along 18°N in case 200. (a) Level 1 and (b) level 3. The dashed lines correspond to the phase speed of the non-dispersive Rossby wave of the first baroclinic mode.

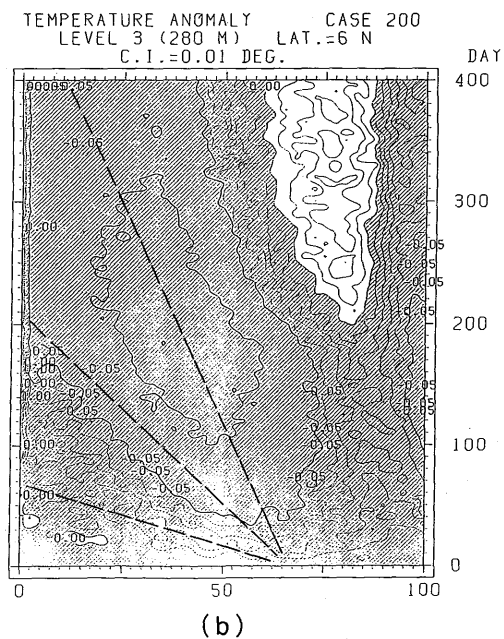
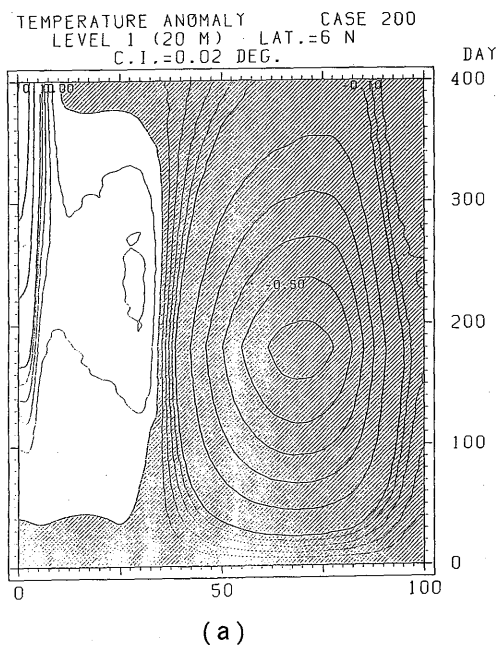


Fig. 4-3-7 As in Fig. 4-3-6 except for 6°N. The dashed lines correspond to the phase speeds of the non-dispersive Rossby waves for the first three baroclinic modes.

At level 3, on the other hand, the cold anomaly drifts westward, and anomalously warm temperatures newly develop in the region where the cold anomaly was initially generated.

Fig. 4-3-7 shows that the cold anomaly of level 1 is nearly stationary in the east-west direction, while that of level 3 drifts westward. The reason why the western edge of the cold anomaly at level 1 does not expand to the west is that the anomalous horizontal advection of the normal temperature field generates warm anomalies (see Fig. 4-3-1(b)). The anomaly center of level 3 propagates at the phase speed of the non-dispersive Rossby wave of the third baroclinic mode.

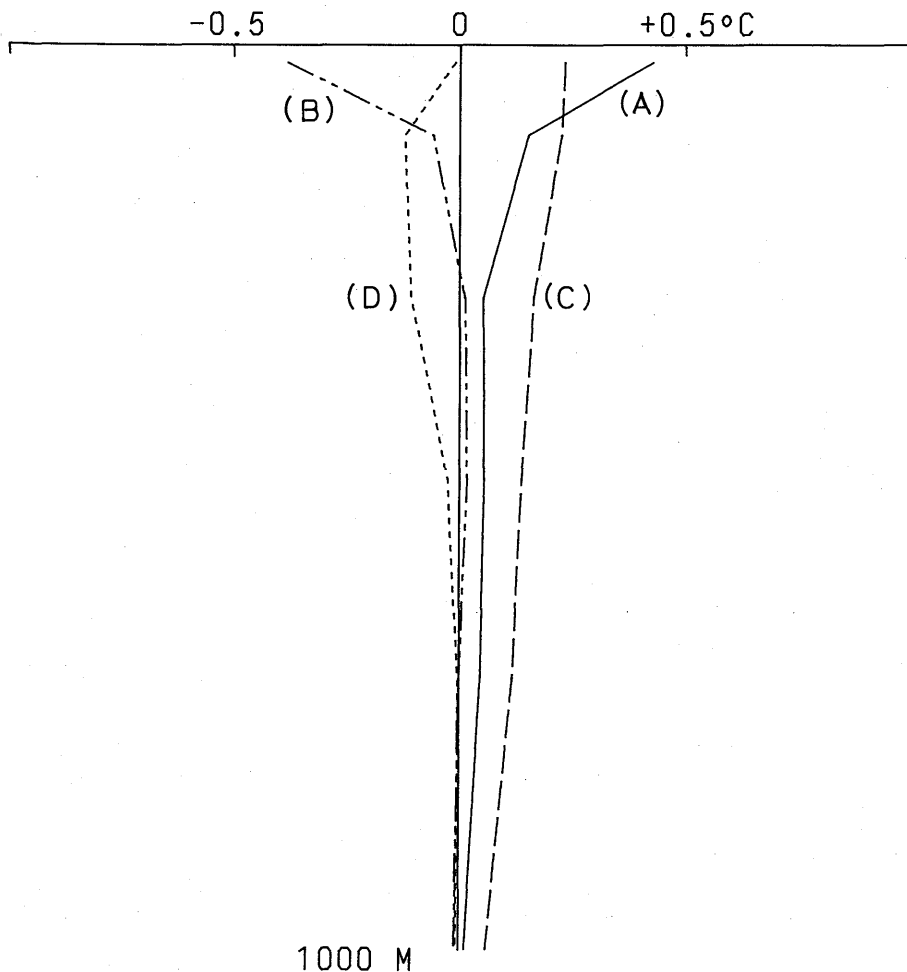


Fig. 4-3-8 Vertical structure of the temperature anomalies on day 360 in case 200. Full line: anomaly (A) at (22°N, 62.5°E), two dots and dashed line: anomaly (B) at (10°N, 65°E), dashed line: anomaly (C) at (20°N, 37.5°E) and dotted line: anomaly (D) at (8°N, 32.5°E).

Fig. 4-3-8 shows the vertical structure of anomalies (A), (B), (C), and (D) marked in Fig. 4-3-4. The eastern two anomalies, warm anomaly (A) and cold anomaly (B) of level 1, have a maximum value at the surface. On the other hand, the western two anomalies, warm anomaly (C) and cold anomaly (D) of level 3, have significant signals at the subsurface. The subsurface signals are comparable with or larger than those at the surface. Another point to be noted is that the warm anomalies (A) and (C) penetrate deeper than the cold anomalies (B) and (D). Anomaly (D) has a higher mode structure than the temperature changes associated with the first baroclinic mode (see Fig. 4-1-2(b)).

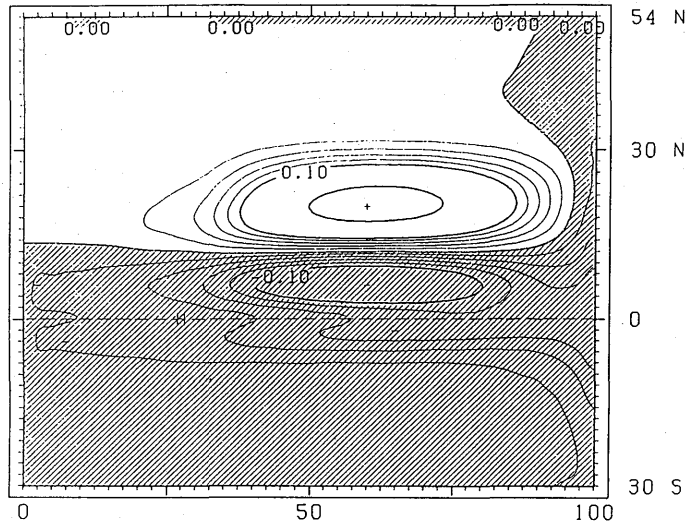
The same anomalous winds as those for case 200 are used for *case 201, the normal state of which is horizontally uniform and motionless*. The initial stratification is that of case 200 averaged over the region from the equator to 30°N and from 0° to 100°E.

Fig. 4-3-9 shows the results on day 360. Between Figs. 4-3-4 and 4-3-9, the following two differences are remarkable. First, the anomalies at level 1 are much smaller in magnitude in case 201 than in case 200. In case 201, anomalies are essentially produced by anomalous vertical motion (Ekman pumping) (term (E) in Eq. (4-1)). In case 200, on the other hand, they are produced by anomalous Ekman currents (The difference in the magnitudes at level 3 is chiefly due to different vertical structures of normal temperature field.) The second is that the westward expansion of the warm anomaly of level 1 is slower in case 201 than in case 200, and the westward displacement of the warm anomaly center of level 3 is also slower. Anomalous horizontal advection of normal temperature field, in this case mainly by anomalous geostrophic currents associated with subsurface anomalies, can explain a large part of this difference. Differences arising from the effect of advection by normal currents (terms (C) and (D)) become clear after day 360. Neither a northward displacement of surface anomalies nor a splitting of a surface anomaly center as in Fig. 4-3-5(a) are seen in case 201.

4.3.2 Variation 1 (case 210)

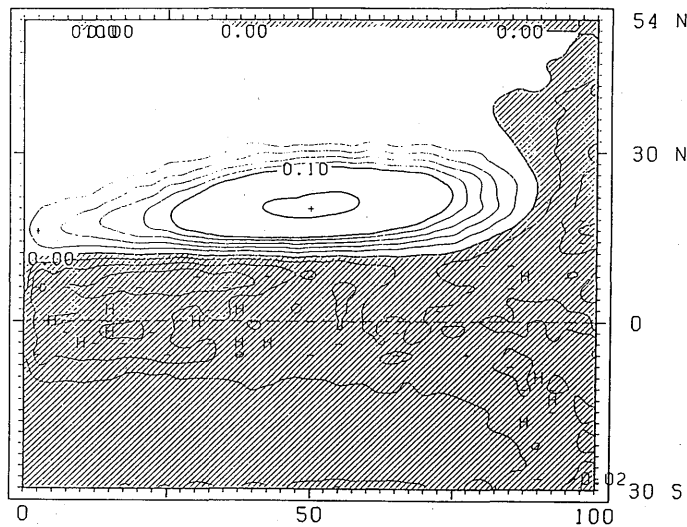
In this experiment, anomalous westward winds are imposed in a narrower region and for a shorter period than in case 200 (Table 4-1-1(a), Fig. 4-1-1(d)). A warm anomaly centered around 18–20°N is formed to the north of 14°N, and a cold anomaly is formed around 10°N. Their evolution after day 90 is essentially the same as that in case 200. In the equatorial region no significant anomalies appear except at the western boundary, though small amplitude signals are discerned to propagate eastward along the equator.

TEMPERATURE ANOMALY CASE 201
C.I.=0.02 DEG. LEVEL 1 (20 M) DAY 360



(a)

TEMPERATURE ANOMALY CASE 201
C.I.=0.02 DEG. LEVEL 3 (280 M) DAY 360



(b)

Fig. 4-3-9 As in Fig. 4-3-1 except for day 360 in case 201.

4.3.3. A warm anomaly (case 250)

This experiment is intended to examine the evolution of existing anomalies. A warm anomaly is introduced in the central tropics at the initial time (Table 4-1-1(b), Fig. 4-1-1(e)). No anomalous wind forcing is introduced. The initial anomaly is uniform from the surface to a depth of 380 m and none below 380 m. The initial field is not in geostrophic balance because no anomalous currents are imposed at the initial time. The current in the model rapidly adjusts to the specified density structure ($1/f \sim 0.3$ days at 14°N). Only the low frequency transient behavior of the model ocean after the initial adjustment is concerned in this experiment.

Fig. 4-3-10 shows the anomalies of level 1 and level 4 on day 120. A pair of cold and warm anomaly under the imposed warm anomaly as shown in Fig. 4-3-10(b), is formed in the lower five levels within 10 days. The cold and the warm anomalies continue to intensify for about half a year and a few months, respectively. The warm anomaly imposed in the upper three levels rapidly elongates westward, although the movement of its center is very slow.

Fig. 4-3-11 shows a zonal vertical section through the anomaly center. The warm anomaly center of level 5 which is located at 25°E on day 120 moves westward at the speed of the non-dispersive Rossby wave of the first baroclinic mode. Along with the movement of this deep anomaly, the warm anomaly in the upper levels extends westward. After it arrives in the western boundary region, it extends further northward and southward along the western boundary. The northward extension, which is obvious in the upper two levels, is due to advection by the boundary currents. On the other hand, the southward extension and subsequent eastward extension along the equator occurs as a result of the propagation of Kelvin waves. The anomalies on day 300 are shown in Fig. 4-3-12.

4.4 Summary and remarks

Numerical experiments to investigate the formation and evolution of large-scale thermal anomalies in the upper ocean were presented in this chapter. The experiments were performed with prescribed anomalies in the zonal wind stress. The anomalies, constant in time, were imposed in the equatorial and in the tropical and subtropical region for 90 or 180 days. Integrations were carried out for a few years.

The results show that temperature anomalies, both surface and subsurface, are initially generated by anomalous winds through wind-induced anomalous advection of normal temper-

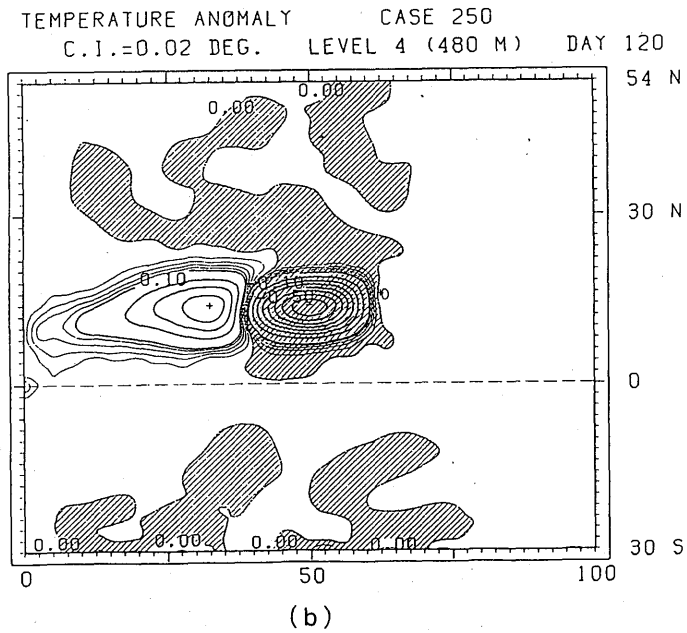
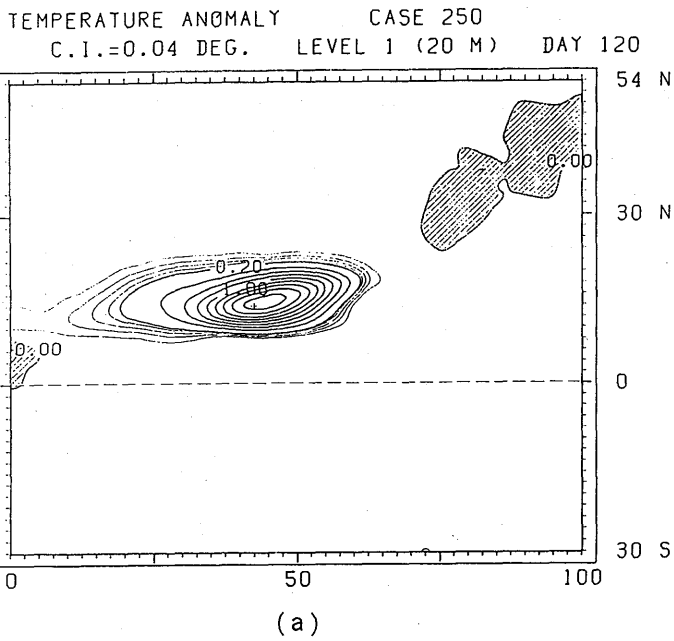


Fig. 4-3-10 Temperature anomalies on day 120 in case 250.
(a) Level 1 and (b) level 4.

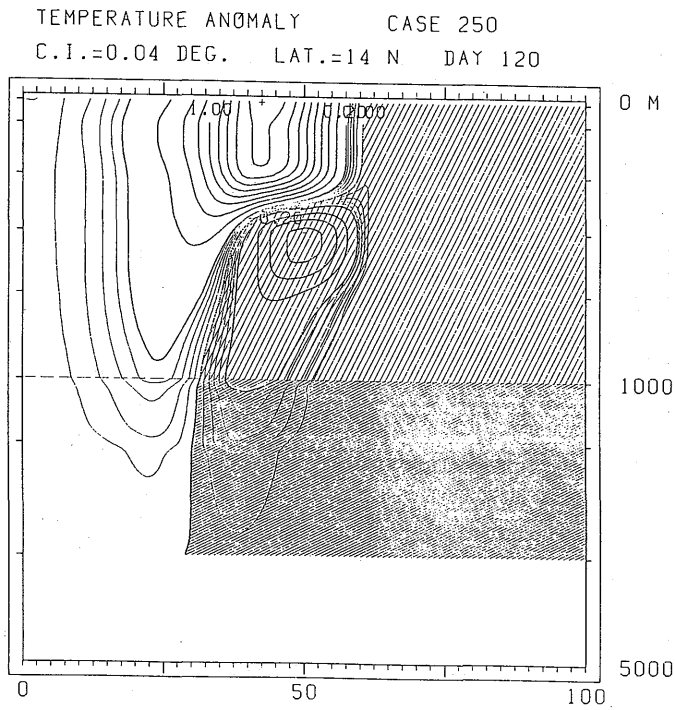


Fig. 4-3-11 A zonal cross-section of the temperature anomalies along 14°N on day 120 in case 250.

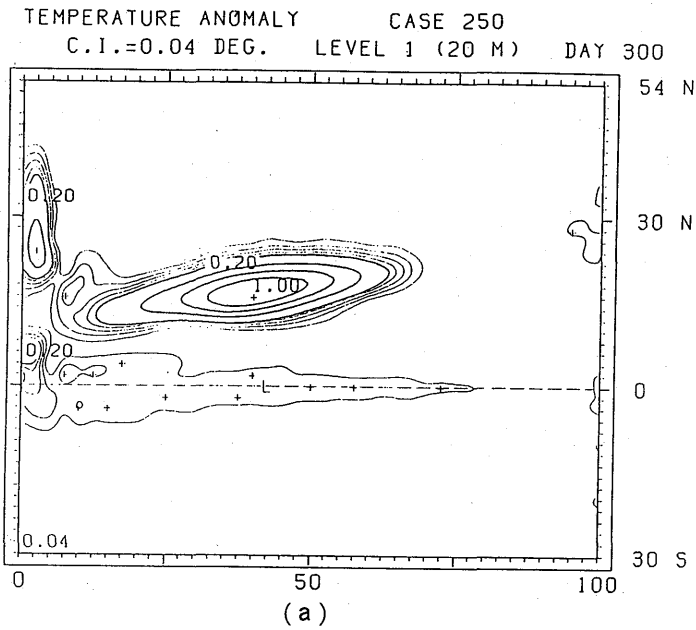


Fig. 4-3-12 As in Fig. 4-3-10 except for day 300.

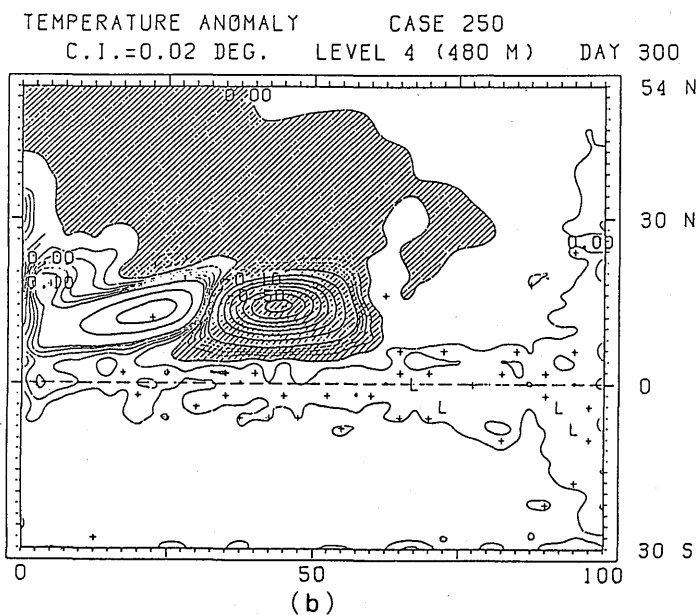


Fig. 4-3-12 Continued.

ature field. Horizontal advection (terms (A) and (B) in Eq. (4-1)) plays the most important role in the surface anomaly generation, and vertical advection (term (E)) in the subsurface anomaly generation. Once temperature anomalies are generated, all the other terms in Eq. (4-1) come into play. The horizontal advection of anomalies by normal currents (terms (C) and (D)) is one of the dominant processes in the upper ocean.

In the extra-equatorial ocean, an initially generated anomaly separates into a surface mode anomaly and a baroclinic mode anomaly. The surface mode anomaly is confined to the uppermost level, and is mainly advected by normal currents. The baroclinic mode anomaly has a significant subsurface signal, and may be accompanied with a surface signal generated due to the advection of normal temperature field by anomalous geostrophic currents associated with the subsurface anomaly. The baroclinic mode anomaly propagates westward at a speed comparable to that of a low baroclinic mode Rossby wave. However, the speed depends on the latitude of anomalously forced region and possibly on the duration and zonal extent of anomalous forcing. When the deep mode anomaly arrives in the western boundary region, a new surface mode anomaly is formed along with Kelvin mode anomalies. The Kelvin mode anomalies propagate equatorward and further eastward along the equator. The new surface mode anomaly tends to propagate or extend poleward through the effect of

advection by the western boundary currents.

In the equatorial ocean, surface mode anomalies are formed in the anomalously forced region, whereas baroclinic mode anomalies rapidly reach the eastern boundary region. Furthermore, new anomalies develop even after anomalous winds are turned off. This is one of the striking differences between responses in the equatorial ocean and the extra-equatorial ocean. The relative importance of each term in Eq. (4-1) depends not only on the latitude but also on large-scale features of the model ocean, such as current pattern and temperature gradient.

The results from this study must be verified and modified using improved models because the present model has a lot of limitations. The normal currents are far slow in comparison with observed currents. The thermocline is not always reproduced properly. The seasonal variation of the normal state is not included. Moreover, the dissipation of anomalies can not be examined with this model because of its highly diffusive nature. The attenuation of baroclinic waves is an important problem for remote forcing.

In spite of the above limitations, however, the results presented here seem to be qualitatively supported by some observational studies.

Favorite and McLain (1973) showed an example of movement of sea surface temperature anomalies in the direction of the North Pacific Current. Gill (1982) analyzed bathythermograph data from the equatorial Pacific during the period 1971–73, and described the changes in subsurface thermal structure associated with the 1972 El Niño. He showed that the changes in the central Pacific and along the eastern boundary were quite distinct. For example, subsurface temperature anomalies did not correlate well with surface temperature anomalies in the central Pacific, but they did along the eastern boundary. Gill (1983) indicated that horizontal advection of normal temperature field by anomalous zonal currents was the primary cause of the surface temperature anomalies in the central Pacific and that near the eastern boundary both anomalous horizontal advection of normal temperature field and upwelling of anomalously warm water significantly contributed to produce surface temperature anomalies. He noted further that once the surface temperature anomalies were created, advection of anomalies by normal currents became significant in spreading the anomalies over a wide range of latitudes.

White et al. (1985) investigated variability in both sea surface temperature and vertically averaged upper ocean (0–400 m) temperature over the Pacific from 20°S to 50°N. They observed that vertically averaged temperature anomalies off the equator propagated

westward at baroclinic Rossby wave speeds, and those at the equator propagated eastward at Kelvin wave speeds. They further observed that sea surface temperature anomalies propagated in the direction of normal surface currents.

Input in the present experiments were anomalies in the zonal wind stress, which are only a part of the anomalous atmospheric forcing responsible for the generation of temperature anomalies. The importance of anomalous surface heating and anomalous vertical mixing due to surface-generated turbulence was pointed out by Haney (1980), who attempted to simulate numerically observed behavior of large-scale thermal anomalies in the central North Pacific.

Elsberry and Garwood (1978) examined sea surface temperature changes at Ocean Weather Station Papa, and demonstrated that synoptic-scale atmospheric disturbances are important for the development of upper-ocean temperature anomalies. The anomalies produced by different forcing would have different vertical structure, so that their evolution is considered to be different. Further experiments using more realistic atmospheric forcing are needed. In the present study, changes in a model ocean induced by local atmospheric forcing were traced down for a few years, but ocean-atmosphere interactions were not included. In nature, anomalies in the sea surface temperature have great impact on the large-scale atmospheric circulation. Subsequent changes in the atmospheric circulation, in turn, tend to modify or newly generate sea surface temperature anomalies. This effect can be studied only by ocean-atmosphere coupled models.

References

- Bryan, K., 1969a: A numerical method for the study of the circulation of the world ocean. *J. Comput. Phys.*, **4**, 347-376.
- Bryan, K., 1969b: Climate and the ocean circulation: III. The ocean model. *Mon. Wea. Rev.*, **97**, 806-827.
- Bryan, K., and M.D. Cox, 1968: A nonlinear model of an ocean driven by wind and differential heating: Part 1. Description of the three-dimensional velocity and density fields. *J. Atmos. Sci.*, **25**, 945-967.
- Dorman, C. E. and R. H. Bourke, 1979: Precipitation over the Pacific Ocean, 30°S to 60°N. *Mon. Wea. Rev.*, **107**, 896-910.
- Elsberry, R. L., and R. W. Garwood, Jr., 1978: Sea surface temperature anomaly generation in relation to atmospheric storms. *Bull. Amer. Meteor. Soc.*, **59**, 786-789.
- Favorite, F., and D. R. McLain, 1973: Coherence in transpacific movements of positive and negative anomalies of sea surface temperature, 1953-60. *Nature*, **244**, 139-143.
- Gill, A. E., 1982: Changes in thermal structure of the equatorial Pacific during the 1972 El Niño as revealed by bathythermograph observations. *J. Phys. Oceanog.*, **12**, 1373-1387.
- Gill, A. E., 1983: An estimation of sea-level and surface-current anomalies during the 1972 El Niño and consequent thermal effects. *J. Phys. Oceanog.*, **13**, 586-606.
- Han, Y.-J., 1975: Numerical simulation of mesoscale ocean eddies. Ph. D. Thesis, Dept. Meteorol., University of California, 153pp.
- Haney, R. L., 1971: Surface thermal boundary condition for ocean circulation models. *J. Phys. Oceanog.*, **1**, 241-248.
- Haney, R. L., 1974: A numerical study of the response of an idealized ocean to large-scale surface heat and momentum flux. *J. Phys. Oceanog.*, **4**, 145-167.
- Haney, R. L., 1980: A numerical case study of the development of large-scale thermal anomalies in the central North Pacific Ocean. *J. Phys. Oceanog.*, **10**, 541-556.
- Kutsuwada, K. and K. Sakurai, 1982: Climatological maps of wind stress field over the North Pacific Ocean. *Oceanog. Mag.*, **32**, 25-46.
- Leetmaa, A., J. P. McCreary, Jr., and D. W. Moore, 1981: Equatorial currents: observations and theory. In *Evolution of Physical Oceanography*, B. A. Warren and C. Wunsch,

- eds., The MIT Press, 184-196.
- McCreary, J., 1976: Eastern tropical ocean response to changing wind systems: with application to El Niño. *J. Phys. Oceanog.*, **6**, 632-645.
- Moore, D. W., and S. G. H. Philander, 1977: Modeling of the tropical oceanic circulation. In *The Sea*, Vol. 6, Wiley-Interscience, New York, 319-361.
- Philander, S. G. H., 1981: The response of equatorial ocean to a relaxation of the trade winds. *J. Phys. Oceanog.*, **11**, 176-189.
- Rasmusson, E. M., and T. H. Carpenter, 1982: Variations in tropical sea surface temperature and surface wind fields associated with the Southern Oscillation/El Niño. *Mon. Wea. Rev.*, **110**, 354-384.
- Semtner, A. J., 1974: An oceanic general circulation model with bottom topography. *Numerical Simulation of Weather and Climate*, Tech. Rept. No. 9, Dept. Meteorol., University of California, 99pp.
- Semtner, A. J., and Y. Mintz, 1977: Numerical simulation of the Gulf Stream and mid-ocean eddies. *J. Phys. Oceanog.*, **7**, 208-230.
- Takano, K., 1974: A general circulation model for the World Ocean. UCLA Dept. of Meteorology Tech. Rep. No. 8.
- Takano, K., 1981: A note on the haline, thermohaline and thermohaline-wind-driven ocean circulation. *La mer*, **19**, 185-203.
- Takeuchi, K., 1984: Numerical study of the Subtropical Front and the Subtropical Counter-current. *J. Oceanog. Soc. Japan.*, **40**, 371-381.
- Weare, B. C., P. T. Strub and M. D. Samuel, 1981: Annual mean surface heat fluxes in the tropical Pacific Ocean. *J. Phys. Oceanog.*, **11**, 705-717.
- Williams, G. P., 1969: Numerical integration of the three-dimensional Navier-Stokes equations for incompressible flow. *J. Fluid Mech.*, **37**, 727-750.
- White, W. B., G. A. Meyers, J. R. Donguy and S. E. Pazan, 1985: Short-term climatic variability in the thermal structure of the Pacific Ocean during 1979-82. *J. Phys. Oceanog.*, **15**, 917-935.
- Wyrtki, K., 1965: The average annual heat balance of the North Pacific Ocean and its relation to ocean circulation. *J. Geoph. Res.*, **70**, 4547-4559.
- Wyrtki, K., and G. Meyers, 1976: The trade wind field over the Pacific Ocean. *J. Appl. Meteor.*, **15**, 698-704.

気象研究所技術報告一覧表

- 第1号 バックグラウンド大気汚染の測定法の開発 (地球規模大気汚染特別研究班, 1978)
Development of Monitoring Techniques for Global Background Air Pollution (MRI Special Research Group on Global Atmospheric Pollution, 1978)
- 第2号 主要活火山の地殻変動並びに地熱状態の調査研究 (地震火山研究部, 1979)
Investigation of Ground Movement and Geothermal State of Main Active Volcanoes in Japan (Seismology and Volcanology Research Division, 1979)
- 第3号 筑波研究学園都市に新設された気象観測用鉄塔施設 (花房龍男・藤谷徳之助・伴野登・魚津 博, 1979)
On the Meteorological Tower and Its Observational System at Tsukuba Science City (T. Hanafusa, T. Fujitani, N. Banno and H. Uozu, 1979)
- 第4号 海底地震常時観測システムの開発 (地震火山研究部, 1980)
Permanent Ocean-Bottom Seismograph Observation System (Seismology and Volcanology Research Division, 1980)
- 第5号 本州南方海域水温図—400 m (又は 500 m) 深と 1000 m 深— (1934—1943 年及び 1954—1980 年) (海洋研究部, 1981)
Horizontal Distribution of Temperature in 400m (or 500m) and 1000m Depth in Sea South of Honshu, Japan and Western-North Pacific Ocean from 1934 to 1943 and from 1954 to 1980 (Oceanographical Research Division, 1981)
- 第6号 成層圏オゾンの破壊につながる大気成分および紫外日射の観測 (高層物理研究部, 1982)
Observations of the Atmospheric Constituents Related to the Stratospheric Ozone Depletion and the Ultraviolet Radiation (Upper Atmosphere Physics Research Division, 1982)
- 第7号 83 型強震計の開発 (地震火山研究部, 1983)
Strong-Motion Seismograph Model 83 for the Japan Meteorological Agency Network (Seismology and Volcanology Research Division, 1983)
- 第8号 大気中における雪片の融解現象に関する研究 (物理気象研究部, 1984)
The Study of Melting of Snowflakes in the Atmosphere (Physical Meteorology Research Division, 1984)
- 第9号 御前崎南方沖における海底水圧観測 (地震火山研究部・海洋研究部, 1984)

- Bottom Pressure Observation South off Omaezaki, Central Honshu (Seismology and Volcnology Research Division and Oceanographical Research Division, 1984)
- 第10号 日本付近の低気圧の統計 (予報研究部, 1984)
Statistics on Cyclones Around Japan (Forecast Research Division, 1984)
- 第11号 局地風と大気汚染物質の輸送に関する研究 (応用気象研究部, 1984)
Observations and Numerical Experiments on Local Circulation and Medium-Range Transport of Air Pollutions (Applied Meteorology Research Division, 1984)
- 第12号 火山活動監視手法に関する研究 (地震火山研究部, 1984)
Investigation on the Techniques for Volcanic Activity Surveillance (Seismology and Volcanology Research Division, 1984)
- 第13号 気象研究所大気大循環モデル-I (MRI・GCM-I) (予報研究部, 1984)
A Description of the MRI Atmospheric General Circulation Model (The MRI・GCM-I) (Forecast Research Division, 1984)
- 第14号 台風の構造の変化と移動に関する研究—台風 7916 の一生— (台風研究部, 1985)
A Study on the Changes of the Three-Dimensional Structure and the Movement Speed of the Typhoon Through Its Life Time (Typhoon Research Division, 1985)
- 第15号 波浪推算モデル MRI と MRI-II の相互比較研究—計算結果図集— (海洋研究部, 1985)
An Intercomparison Study Between the Wave Models MRI and MRI-II—A Compilation of Results— (Oceanographical Research Division, 1985)
- 第16号 地震予知に関する実験的及び理論的研究 (地震火山研究部, 1985)
Study on Earthquake Prediction by Geophysical Method (Seismology and Volcanology Research Division, 1985)
- 第17号 北半球地上月平均気温偏差図 (予報研究部, 1986)
Maps of Monthly Mean Surface Temperature Anomalies over the Northern Hemisphere for 1891—1981 (Forecast Research Division, 1986)
- 第18号 中層大気の研究 (高層物理研究部・気象衛星研究部・予報研究部・地磁気観測所, 1986)
Studies of the Middle Atmosphere (Upper Atmosphere Physics Research Division, Meteorological Satellite Research Division, Forecast Research Division, MRI. The Magnetic Observatory, 1986)
- 第19号 ドップラーレーダによる気象・海象の研究 (気象衛星研究部・予報研究部・応用気象研究部・海洋研究部, 1986)
Studies on Meteorological and Sea Surface Phenomena by Doppler Radar (Meteor-

ological Satellite Research Division, Typhoon Research Division, Forecast Research Division, Applied Meteorology Research Division, Oceanographical Research Division, 1986)

第20号 気象研究所対流圏大気大循環モデル (MRI・GCM-I) による12年間の積分 (予報研究部, 1986)

Mean Statistics of the Tropospheric MRI・GCM-I based on 12-year Integration (Forecast Research Division, 1986)

第21号 宇宙線中間子強度1983—1986 (高層物理研究部, 1987)

Multi-Directional Cosmic Ray Meson Intensity 1983—1986 (Upper Atmosphere Physics Research Division, 1987)

第22号 静止気象衛星「ひまわり」画像の噴火噴煙データにもとづく噴火活動の解析に関する研究 (地震火山研究部, 1987)

Study on Analyses of Volcanic Eruptions based on Eruption Cloud Image Data Obtained by the Geostationary Meteorological Satellite (GMS) (Seismology and Volcanology Research Division, 1987)

第23号 オホーツク海海洋気候図 (篠原吉雄・四竈信行, 1988)

Marine Climatological Atlas of the Sea of Okhotsk Y. Shinohara and N. Shikama, 1988)

気象研究所

1946年(昭和21年)設立

所長：理博 岡村 存

予報研究部	部長：	久保田	効
気候研究部	部長：	桐山	一陽
台風研究部	部長：	蔵重	清
物理気象研究部	部長：	旭	満
応用気象研究部	部長：	眞島	恒裕
気象衛星・観測システム研究部	部長：	鯉沼	正一
地震火山研究部	部長：理博	勝又	護
海洋研究部	部長：	佐野	昭
地球化学研究部	部長：理博	杉村	行勇

気象研究所技術報告

編集委員長：勝 又 護

編集委員：藤部文昭 木田秀次 高谷美正
忠鉢 繁 佐藤純次 内野 修
古屋逸夫 遠藤昌宏 井上久幸
事務局：松下 眞 中山和之

気象研究所技術報告は、気象学、海洋学、地震学、その他関連の地球科学の分野において、気象研究所職員が得た研究成果に関し、技術報告、資料報告及び総合報告を掲載する。

気象研究所技術報告は、1978年(昭和53年)以降、必要の都度刊行される。

平成元年3月31日発行 ISSN 0386-4049

編集兼発行所 気象研究所

茨城県つくば市長峰1-1

印刷所 株式会社 明文社

東京都中央区日本橋蛸殻町1-24-8